# Dissertation

submitted to the
Combined Faculties for the Natural Sciences and for Mathematics
of the Ruperto-Carola University of Heidelberg, Germany
for the degree of
Doctor of Natural Sciences

presented by

Diplom-Physiker:     Thomas Tücking
born in:             Weinheim

Oral examination: 24.01.2007

# Development and Realization
# of the IGRT Inline Concept

Referees:   Prof. Dr. Uwe Oelfke

              Prof. Dr. Josef Bille

# Entwicklung und Realisierung des IGRT Inline Konzepts

## Zusammenfassung

In der vorliegenden Arbeit wird ein neues Konzept zur Anbindung eines bildgebenden Systems an einen medizinischen Linearbeschleuniger für die Strahlentherapie vorgestellt und dessen Realisierung beschrieben. Dafür wurden eine Röntgenröhre und ein Flächendetektor an gegenüberliegenden Seiten eines Linearbeschleuniger installiert, so dass der Detektor nicht nur zu Röntgenaufnahmen eines auf dem Behandlungstisch liegenden Patienten dient, sondern auch die Primärfluenz des Therapiestrahls gemessen werden kann. Mittels verschiedener im Verlauf dieser Arbeit entwickelter Hardwarekomponenten konnte das bildgebende System mit dem Therapiegerät synchronisiert werden. Dies ermöglichte neben fluoroskopischen Röntgensequenzen während der Behandlung und der Aufnahme von Kegelstrahl-CTs, u. a. die Einbeziehung atmungskorrelierter Signale externer Systeme zur atemgesteuerten Bildgebung und Therapie. Zudem werden diverse Anwendungen, Messungen und Untersuchungen, die mit Hilfe des neuen Systems durchgeführt wurden, diskutiert. Hierbei handelt es sich u. a. um Fragestellungen bezüglich des Einflusses verschiedener Aufnahmeparameter auf die Bildqualität und um die Verwertbarkeit gewonnener Bilder für Konzepte der Adaptiven Strahlentherapie. Des Weiteren werden Patientenstudien beschrieben und analysiert, die mit dem vorgestellten System durchgeführt wurden, um bildgebende Verfahren in den klinischen Therapieablauf zu integrieren und so eine präzisere Bestrahlung zu ermöglichen. Abschließend wird ein erster an das erläuterte Konzept angelehnter Prototyp eines kommerziellen Linearbeschleunigers vorgestellt.

## Development and realization of the IGRT Inline concept

## Abstract

A new concept for the integration of an imaging system into a medical linear accelerator for radiotherapy is presented, and its technical realization is described. An x-ray tube and a flat panel detector were installed along the treatment beam axis, such that the detector could not only be used for x-ray imaging of patients lying on the treatment couch, but also to measure the primary fluence of the therapy beam. The imaging system was synchronized with the linear accelerator by means of several hardware and software components that were developed as a part of this work in order to allow, for instance, the acquisition of fluoroscopic image sequences during beam delivery and the acquisition of volumetric cone beam CT information. Furthermore, external patient monitoring systems were integrated for respiration triggered imaging.

Several applications and investigations about image quality, about the application of the images for the concepts of Adaptive Radiotherapy, and about the improvement of image quality were carried out using the new system. Furthermore, first feasibility studies with patients were performed, that combine imaging and therapy at the linac, in order to provide a higher precision for the beam delivery. Finally, the first commercial prototype, following the described concept, is presented.

# Contents

# Abbreviations, acronyms and definitions

| | |
|---|---|
| **ADC** | analog-to-digital converter |
| **AP** | anterior-posterior |
| **ART** | Adaptive Radiotherapy |
| **a.u.** | arbitrary units |
| **BB** | beam blocker |
| **BEV** | beam's eye view |
| **BNC** | Bayonet Neill-Concelman (the inventors of the BNC connector) |
| **CAN** | Controller Area Network |
| **CBCT** | cone beam CT |
| **CC** | caudal-cranial |
| **CNR** | contrast to noise ratio |
| **CPC** | counts-per-measured-charge quotient |
| **CT** | Computer Tomography |
| **CW** | clockwise |
| **CCW** | counterclockwise |
| **DCM** | digital cine mode |
| **DRR** | digital reconstructed radiograph |
| **DVH** | dose volume histogram |
| **e$^-$** | electron |
| **e$^+$** | positron |
| **EIA** | Electronic Industries Alliance |
| | *more common for EIA-232: RS-232.* |
| **ESF** | edge spread function |
| **FBCT** | fan beam CT |
| **FFT** | fast fourier transform |
| **FDK-Algorithm** | Feldkamp, Davis & Kress - CBCT reconstruction algorithm |
| **FOV** | field of view |
| **FPI** | flat panel imager |
| **HF** | high frequency |
| **HIS** | Heimann Imaging Software |
| **HU** | Hounsfield unit |
| **HV** | high voltage |
| **HW** | hardware |
| **IEC** | International Electrotechnical Commission |
| **IGRT** | Image Guided Radiotherapy |
| **IMRT** | intensity modulated radiotherapy |
| **I/O** | input / output |
| **keV** | kilo electron volts ($1\,\text{keV} \approx 1.6 \cdot 10^{-16}$ J) |
| **KICK** | KV Imaging Control Kit |
| **kV** | kilovolt(age) |

| | |
|---|---|
| **kV source** | x-ray tube, generator and collimator as a system |
| **LED** | light emitting diode |
| **linac** | linear accelerator |
| **LR** | left-right |
| **LSF** | line spread function |
| **MB** | megabyte ($1\,\text{MB} = 1024^2\,\text{Byte}$) |
| **MeV** | mega electron volts ($1\,\text{MeV} \approx 1.6 \cdot 10^{-13}$ J) |
| **MLC** | mulitleaf collimator |
| **MRT** | Magnetic Resonance Tomography |
| **MTF** | modular transfer function |
| **MU** | monitor unit |
| **MV** | megavolt(age) |
| **OAR** | organ at risk |
| **OCS** | Oncology Care Systems (department of Siemens Medical Solutions) |
| **OTF** | optical transfer function |
| **PC** | personal computer |
| **PCI** | Peripheral Component Interconnect |
| **PET** | Positron Resonance Tomography |
| **PROM** | programmable read only memory |
| **QA** | quality assurance |
| **RO** | radiation on |
| **RS** | Radio sector *or* Recommended standard |
| **RT** | radiotherapy |
| **RGS** | respiratory gating system |
| **RTT** | radiation therapy technician |
| **SDD** | source to detector distance |
| **SID** | source to isocenter distance |
| **SNR** | signal to noise ratio |
| **SPR** | scatter to primary ratio |
| **SSD** | source to surface distance |
| **SW** | software |
| **SWR** | Start Wechselrichter (start inverter) |
| **TFT** | thin film transistor |
| **TPS** | treatment planning system |
| **TTL** | transistor-transistor-logic |
| **USB** | universal serial bus |
| **VOI** | volume of interest |
| **x-ray toolbox** | Internet accessible tool for the simulation of x-ray spectra |
| | `http://www.healthcare.siemens.com/med/rv/spektrum/default.asp` (11/2006) |

# Chapter 1

# Introduction

Latest developments in modern radiotherapy allow very precise dose deliveries in this non-invasive method for the treatment of tumor diseases. Intensity Modulated Radiotherapy (IMRT) techniques together with inverse treatment planning provide the possibility to deliver homogeneous photon dose distributions to nearly any kind of randomly shaped target volume and to simultaneously produce very steep dose gradients towards adjacent organs at risk (OARs) [1], [2]. This usually results in a better dose sparing of normal tissue and OARs combined with better tumor control probabilities.

To utilize these benefits requires an exact knowledge of the patient's anatomy and the treatment setup including the patient's position during the treatment. At first, this information is provided by a planning CT acquired at a certain time before the start of the treatment course. Fixation systems like masks and body casts can be applied for patient immobilization and marks on the cast or tatoos on the patient's skin are used to adjust the patient position on the treatment couch with the room lasers [3]. However, the dose delivery is usually divided into several daily treatment fractions, so that one treatment course may last 6 – 7 weeks. During this time, inter-fractional changes of the patient's anatomy like loss or gain of weight, tumor regression, fill level of the bladder, etc. may occur with respect to the anatomy observed on the initial planning CT. Additionally, intrafractional organ motion that occurs during the dose delivery process may influence the treatment precision. This primarily concerns breathing induced motion, especially for the irradiation of lung tumors but may also occur for prostate cases. Furthermore, setup errors during the daily patient positioning process might occur.

To handle these known problems, the target volumes to being irradiated are usually increased by safety margins to avoid any underdosage of the tumor caused by these uncertainties. However, this necessary procedure limits the gains of modern high precision radiotherapy techniques and may prevent even better normal tissue sparing. Theoretically, applicable high conformal dose distributions restricted to the tumor volume, as would be possible for static anatomies and fixed patient positions, are thwarted by an uncertainty of the situation at the time of dose delivery. But how does one fully exploit the potential of currently existing dose delivery techniques? Ideally one has an exactly positioned patient and the knowledge of the patient anatomy at any time of the treatment to allow a margin reduction as far as possible [4] – [9].

The concept of Adaptive Radiotherapy (ART) aims to provide strategies that solve this problem. ART is a feedback treatment process that optimizes a patient's treatment according to the patient specific images obtained either directly prior or during the course of treatment [10]. Image guidance plays an important role within ART [11]. In Image Guided Radiotherapy (IGRT) real-time 3D information of the actual treatment setup and the actual anatomy of the patient before every treatment fraction, and optionally even during dose delivery, can be provided by imaging systems in the treatment room [12] – [14]. Though there are many different imaging modalities like optical systems, ultrasound, PET, MRT, etc. this work focuses on x-ray imaging, especially on linear accelerator (linac) integrated kilovoltage (kV) imaging.

The prominent approach of kV-imaging for IGRT utilizes an x-ray tube mounted at the linac [15] – [18]. The treatment machine then provides x-rays of two different energy ranges: i) a megavoltage (MV)-spectrum for treatment (optionally also for imaging) with photon energies up to several MeV generated by the linac, and ii) a kV-spectrum for imaging with photon energies up to about 150 keV generated by the x-ray tube. To use the x-rays for patient imaging additionally requires that an x-ray detector has to be mounted at the treatment machine opposite to the x-ray source so that the patient lies between the x-ray source and the x-ray detector. The detector is an amorphous silicon (a-Si:H) flat panel imager (FPI) [19], [20]. With such linac-integrated imaging systems, radiographs of the patient can be acquired in treatment position prior and during every treatment fraction from arbitrary angles of the linac rotation axis. Besides pure radiographies for 2D imaging the acquisition of cone beam CTs (CBCTs) to obtain 3D information of the patient's anatomy that may, for instance, be used for accurate patient positioning, is provided by these setups as a further important feature [17], [21] – [26].

Several vendors have developed linacs with integrated kV-imaging systems. Figure 1.1 shows two examples of commercially available setups. In both cases either the x-ray tube is installed at 90°
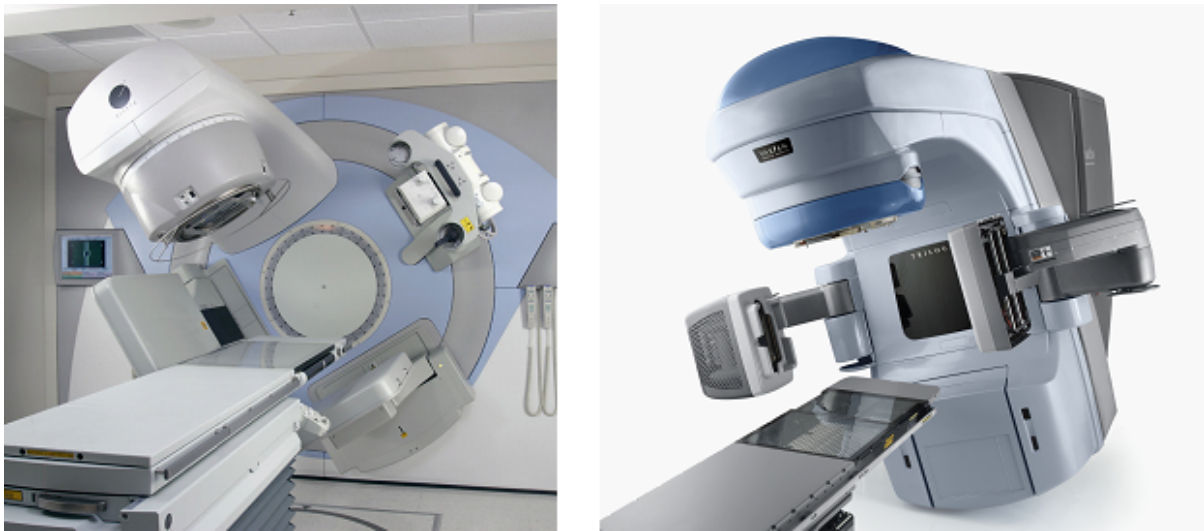


Figure 1.1: Linac integrated IGRT setups

*These two examples follow the 90 degree solution of linac-integrated kV-imaging systems. The Synergy system from Elekta on the left has an x-ray tube installed at 90° and the FPI at 270° – the Trilogy system from Varian vice versa. In both cases the kV-beam is perpendicular to the MV-beam. The pictures sources are the internet pages of the vendors (*`http://www.elekta.com`* and* `http://www.varian.com`*).*

and the FPI at 270° with respect to the MV-source or vice versa[1]. For those *90 degree solutions* the imaging axis is always perpendicular to the treatment beam axis. A further approach is the *Inline Concept* [18], [28] – [31], where the x-ray tube is mounted at 180° with respect to the treatment beam. Therefore, the FPI is placed below the mulitleaf collimator (MLC) and can detect both the kV- and the MV-beam that share the same axis. This concept is described in more detail in section 3.2. The gain of this work is the development and realization of a linac integrated IGRT system prototype following the *Inline Concept*. The different features of this technical concept, the development of the first prototypes, and their first successful clinical applications are discussed.

---

[1]linac coordinates are given according to the norm IEC 61217 [27] throughout this work unless otherwise noted. The coordinates systems used in this work are summarized in section 2.1.

In Chapter 2 some basics are given concerning x-ray imaging and definitions of coordinate systems used within this work. Then the *Inline concept* is described and a motivation for using kV-spectra for imaging at the treatment machine is given in Chapter 3. The first step of the development using a bench top system of an integrated kV-imaging setup and the basic components are described in detail in Chapter 4. The continuation of the development process is described in Chapter 5, mainly covering by the integration of the kV-system at the treatment machine, the substitution of certain imaging components, and the development of further peripheral components to allow special imaging applications. Both chapters 4 and 5 already partly include methods and results of measurements and investigations specifically related to the respective state of development. The main part of investigations and applications using the developed imaging system are provided in Chapter 6: Measurements concerning the influence of the image quality of CBCTs on certain imaging or reconstruction parameters are reported. Furthermore, first clinical applications of the *Inline concept* prototype system are presented, and methods and investigations are described concerning dose calculations and scatter corrections of image data obtained from the realized IGRT setup. Finally, in Chapter 7 a short summary of the presented work is given and the first commercially implemented prototype of the described concept and developments is introduced.

# Chapter 2

# Basics

This chapter summarizes the technical and physical basics that are accessed in this work. Only the principles and formulas that are needed for better understanding of this work are presented; no detailed derivations are given. Furthermore, coordinates and terms and definitions that are dealt with are introduced if not yet addressed in the introduction. A general knowledge and understanding of the common terms used in the field of Medical Physics and especially of radiotherapy is assumed. Abbreviations are listed in *Abbreviations, acronyms and definitions* at the beginning of this work.

## 2.1 Coordinate systems

### 2.1.1 Linac coordinate systems

The linac coordinate systems are defined according to IEC 61217. Figure 2.1 shows a layout of the treatment room to give an overview of the movable components and their alignment. The rotational axes of the three components (gantry , MLC and table) are outlined in the picture. The intersection point of these axes is defined as the *isocenter*. Gantry- and MLC rotation can be *clockwise* (CW)
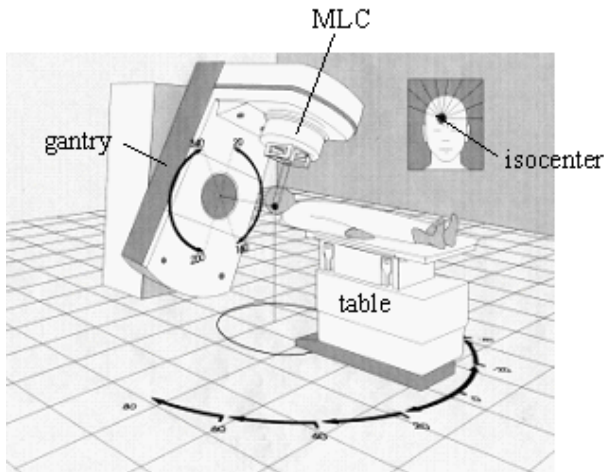


*The turnable components are the gantry (here shown without IGRT equipment), the MLC, and the table. In this illustration MLC and table are placed at 0° and the gantry at about 20°, each in its own rotational system. The isocenter is defined as the intersection point of the three rotation axes. Picture source: [32].*

Figure 2.1: Layout of the treatment room

and *counterclockwise* (CCW). The definition of both rotation systems is illustrated in figure 2.2. For mechanical reasons the gantry can only be rotated up to 190° CW and down to 170° CCW. Therefore, a full 360° rotation needs to be started between 170° and 190°. The rotation system of a linac-mounted x-ray tube is the same as for the gantry. Following the *inline approach* the tube angle is defined by $\gamma_t = (\gamma_g + 180)\,\text{MOD}\,360$, with $\gamma_t$: tube angle, $\gamma_g$: gantry angle, and MOD: modulo function.
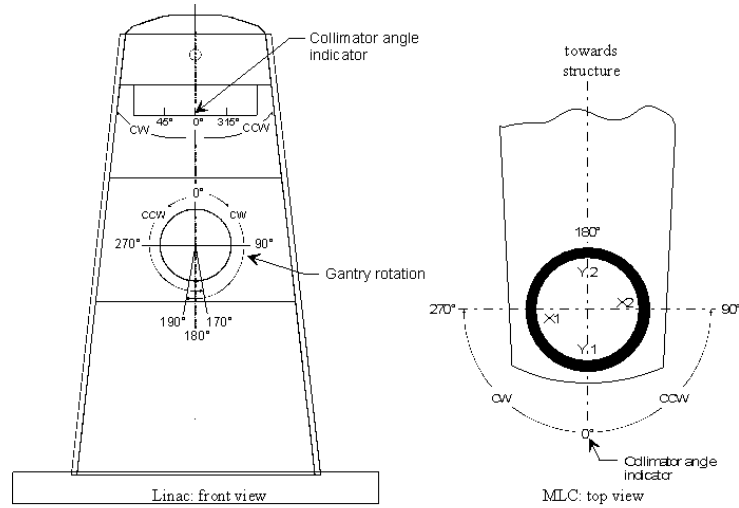
Figure 2.2: Rotation angles of gantry and MLC

*Viewed from the front the gantry angle increases CW. From beam's eye view (BEV) the MLC angle increases CCW. X1, X2, Y1, Y2 indicate the leaf banks and the jaws of the collimator. Pictures source: [33].*

The table can additionally be moved longitudinally, laterally, vertically. The different cartesian table axes, as well as the room coordinate system, are illustrated in figure 2.3. The origin of this system coincides with the isocenter. With the table at 0° the x-axis corresponds to the lateral, the y-axis to the longitudinal, and the z-axis to the vertical table axis.
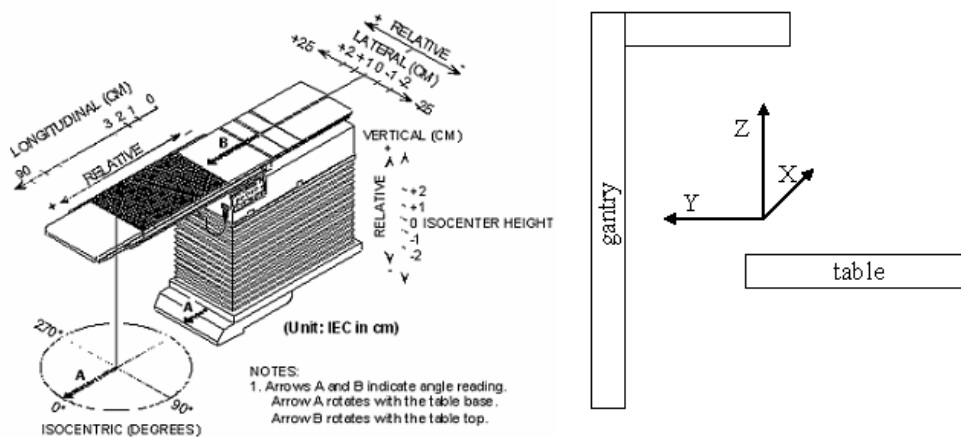


Figure 2.3: Table axes and room system

*The three cartesian table axes conform to the room system (X, Y, Z) for the table at 0°. The origin of the room system is the isocenter. Standing in front of the linac the positive x-direction goes left-right, the positive y-direction back-forward, and the positive z-axis bottom-up. Source of the left picture: [33].*

### 2.1.2   Patient coordinate system

The patient coordinate system is illustrated in figure 2.4. The x-axis is parallel to the patient's left-right (LR) direction, the y-axis to the anterior-posterior (AP) direction, and the z-axis to the caudal-
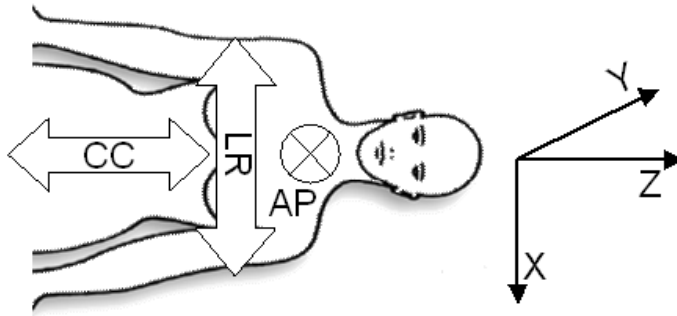
*In common treatment posi-
tion, the x-axis of the patient
coordinate system is parallel
to the x-axis of the room co-
ordinate system (figure 2.3),
the y-axis antiparallel to the z-
axis and the z-axis parallel to
the y-axis. The origin is de-
fined individually.*

Figure 2.4: Patient coordinate system

cranial (CC) direction. The origin of this coordinate system varies from case to case. Throughout this work, 'treatment position' means that the patient lies with his back on the treatment table at $0°$ and his head towards the linac. In this case, room coordinates can be transformed into patient coordinates as follows:

$$\begin{pmatrix} x_p \\ y_p \\ z_p \end{pmatrix} = \begin{pmatrix} 1 & 0 & 0 & -x_0 \\ 0 & 0 & -1 & z_0 \\ 0 & 1 & 0 & -y_0 \end{pmatrix} \begin{pmatrix} x_r \\ y_r \\ z_r \\ 1 \end{pmatrix} \tag{2.1}$$

with $(x_p, y_p, z_p)$: coordinates in the patient system, $(x_r, y_r, z_r)$: coordinates in the room system, and $(x_0, y_0, z_0)$: coordinates of the patient system's origin in room coordinates.

### 2.1.3 Detector coordinate system

Throughout this work the used FPIs have an active area of $1024 \times 1024$ pixels. Each pixel has dimensions of $400 \times 400\,\mu\mathrm{m}^2$. The detector design is mostly symmetrical but has plug connections
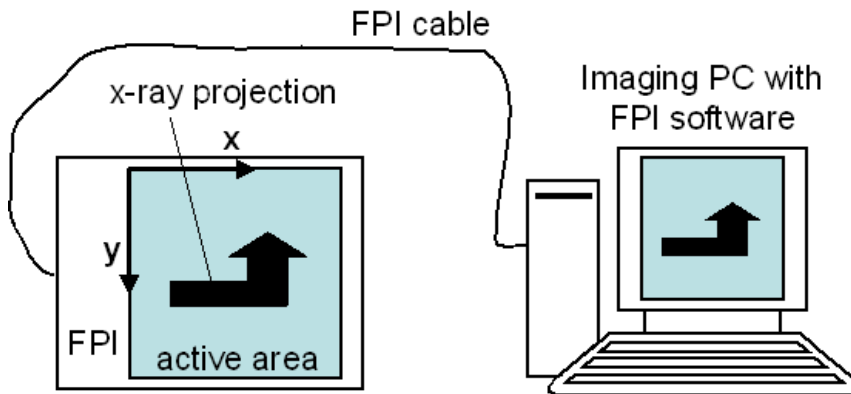


*Detector front view, de-
tector cables left: In this
case the detector coordi-
nate system has its ori-
gin in the upper left cor-
ner of the active area.
Raw images are always
displayed at the com-
puter screen with the
origin at the upper left
corner.*

Figure 2.5: Detector coordinate system

at one side for power supply, readout trigger, and information transfer with the imaging PC. Figure 2.5 shows the orientation of the FPI coordinate system on the FPI itself and on the imaging PC screen. FPI coordinates are given in pixels. The x-coordinate represents the FPI column and the y-coordinate the row. Throughout this work raw images of the FPI are printed as displayed on the PC screen unless otherwise noted. How an object is displayed depends on the orientation of the FPI to the patient coordinate system, and is determined by means of the position of the plug connections or the FPI cable.

### 2.1.4   CBCT projection coordinate system

For CBCT reconstruction the detector coordinates themselves are not of interest, but rather the rotation axis of the imaging system (x-ray source and detector) and the orientation of the FPI to this axis. In a linac-integrated IGRT system the imaging rotation axis coincides with the gantry rotation axis. During the acquisition of a CBCT sequence the imaging system rotates around this axis and permanently acquires x-ray projections of the object to be imaged. Figure 2.6 schematically illustrates a CBCT imaging system and the projection coordinate system. On the
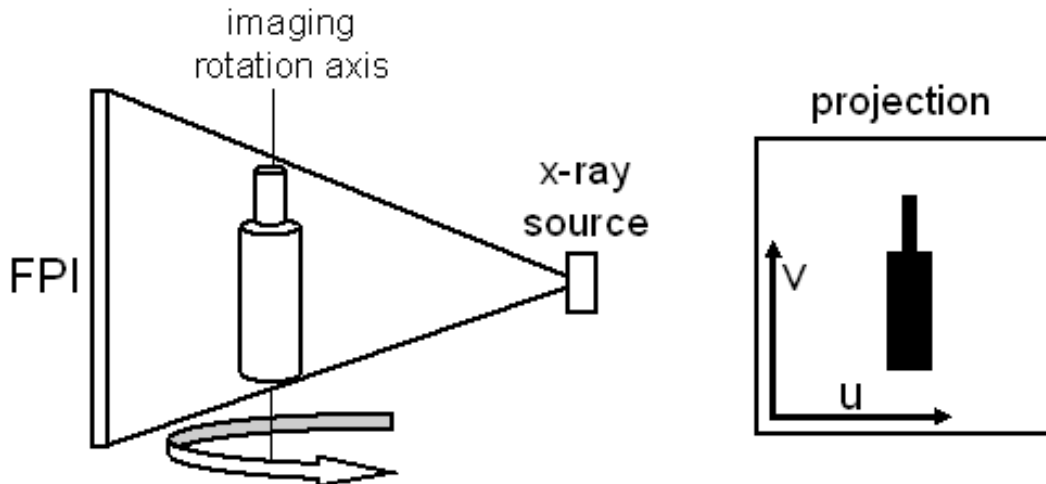


Figure 2.6: CBCT setup and projection coordinate system

*The imaging system consisting of the x-ray source and the FPI rotates around the longitudinal axis of the imaging object (left). The projections of the symmetrical imaging object (right) look the same for any imaging angle. The v-axis is always parallel to the imaging rotation axis. The u-axis is perpendicular to the v-axis and has no fixed direction in the room system.*

2D projections the axis parallel to the rotation axis is the v-axis. The u-axis is perpendicular to the v-axis. The origin of the projection coordinate system is the lower left corner of the projection. Projection coordinates are also given in pixels. The projection matrix may be sampled down to $1024 \cdot 2^{-n} \times 1024 \cdot 2^{-m}$ pixels. The pixel size is then $(400 \cdot 2^n \times 400 \cdot 2^m)\mu m^2$. Throughout this work the v-axis is parallel to the y-axis of the room coordinate system.

## 2.2   Interaction of x-rays and matter

For x-ray imaging the amount of radiation remaining from an incident fluence after passing through an object is measured. Since the energies of x-ray photons are much too high to be absorbed in electron transitions between states for most atoms, they can interact with an electron only by knocking it completely out of the atom. That is, all x-rays are classified as ionizing radiation. Within the object mainly three different kinds of interactions between x-rays and matter may attenuate the incident beam:

### 2.2.1   Photoionization

Photoionization is based on the photoelectric effect (figure 2.7). In the presence of a third particle (the nucleus) a photon may be absorbed by transmitting nearly its complete energy to the electron. There are strong maxima at the cross section for the photoionization, if the energy of the photons is just high enough to release an electron from a certain electron shell. Apart from the absorption edges, the total absorbtion cross section $\sigma_{ph}$ for this process approximately is proportional the
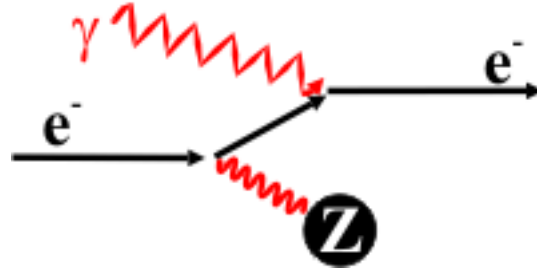
*An electron, electrically bound to nucleus 'Z', interacts with a photon and gains energy. The photon is completely annihilated in this process.*

Figure 2.7: Photoelectrical effect

atomic number $Z$ of the material to the power of 5 [34]. For non-relativistic energies ($\alpha = \frac{E_\gamma}{m_0 c^2} < 1$, with $m_0$: electron's rest mass), it is approximately
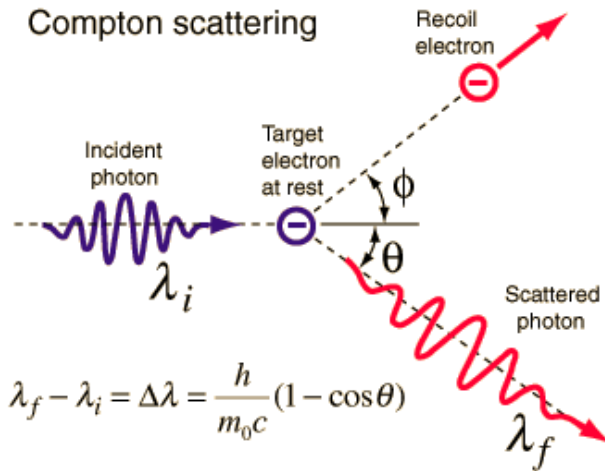
$$\sigma_{ph} \propto Z^5 E_\gamma^{-\frac{7}{2}} \tag{2.2}$$

For higher energies ($\alpha > 1$), it is approximately

$$\sigma_{ph} \propto \frac{Z^5}{E_\gamma} \ . \tag{2.3}$$

### 2.2.2 Compton scattering

The process of Compton scattering is illustrated in figure 2.8. During this process the energy of the



*The incident photon gets absorbed by the electron, and a scattered photon is produced. $\lambda_f$ and $\lambda_i$ are the wave length of the scattered and the incident photon and $m_0$ the electron's rest mass. Momentum- and energy transfer of the incident photon follow the laws of classical mechanics. Picture source: [35].*

Figure 2.8: Compton scattering

absorbed photon is divided into the transmitted energy to the collision electron and the production of a scattered photon. Again a third collision partner (the nucleus) is necessary due to conservation laws. The distribution of energy and momentum and the angle between the recoil electron and the scattered photon follow the laws of classical collision processes. The differential cross section of the scattered photon $\frac{d\sigma_c}{d\Omega}$ for this interaction is given by *Klein-Nishina*:

$$\frac{d\sigma_c}{d\Omega} = r_0^2 \left( \frac{1}{1 + \alpha(1 - \cos\theta)} \right)^2 \left( \frac{1 + \cos^2\theta}{2} \right) \left( 1 + \frac{\alpha^2(1 - \cos\theta)^2}{(1 + \cos^2\theta)[1 + \alpha(1 - \cos\theta)]} \right) \tag{2.4}$$

with $r_0$ the classical electron radius, and . $\theta$ is the angle between the incident and the scattered photon (see figure 2.8). For small $\alpha$ this results in the classical *Thomson cross section*:

$$\frac{d\sigma_c}{d\Omega} \overset{\alpha \to 0}{=} \frac{r_0^2}{2}(1 + \cos^2\theta) \tag{2.5}$$

Figure 2.9 shows the angular distribution for different energies of the incident photon. The nearly isotropic distribution for low energies changes to forward scattering for energies in the MeV range. The integral over every $\Omega$ results in the total cross section $\sigma_c$ that is also illustrated in figure 2.9
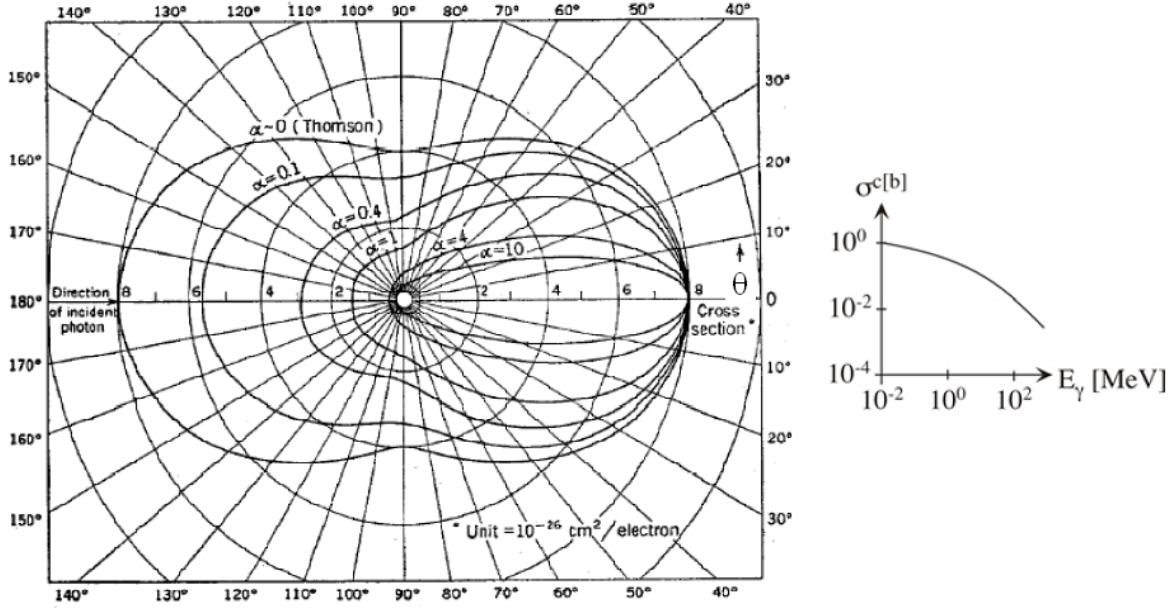


Figure 2.9: Compton scattering cross sections

*Left: Angular distribution of the scattered photon. For low energies $E_\gamma = 511\,keV \cdot \alpha$ of the incident photon the angular distribution is nearly isotropic. For higher energies ($\alpha > 1$) forward scattering dominates. Right: Total cross section given in units of barn ($1b = 10^{-28}m^2$). Source of the left picture: [36].*

$$\sigma_c = 2\pi r_0^2 \left[ \frac{1+\alpha}{\alpha^2} \left( \frac{2(1+\alpha)}{1+2\alpha} - \frac{1}{\alpha} \log(1+2\alpha) \right) + \frac{1}{2\alpha} \log(1+2\alpha) - \frac{1+3\alpha}{(1+2\alpha)^2} \right] \quad (2.6)$$

### 2.2.3  Pair production

Pair production occurs for energies $E_\gamma > 2m_0c^2 = 1.022\,\text{MeV}$ of the incident photon. In presence of a nucleus, the incident photon gets absorbed by creating an $e^+e^-$ pair. The remaining energy $E_\gamma - 2m_0c^2$ is divided as kinetic energy between the leptons. The nucleus is needed for momentum conservation. The pair production process is schematically illustrated in figure 2.10.
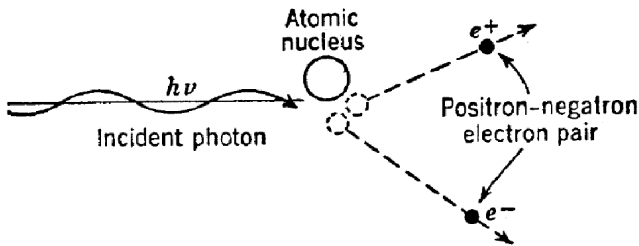


*The incident photon with an energy $E_\gamma > 1.022\,MeV$ creates an electron-positron pair.*

Figure 2.10: Pair production

## 2.2.4 Absorption coefficients

The attenuation of photons with energy $E_\gamma$ having an geometrical path length $d$ through an homogeneous object is described by:

$$I_{E_\gamma}(d) = I_{0,E_\gamma} \cdot \exp(-\mu(Z, E_\gamma) \cdot d) \tag{2.7}$$

with $I_{0,E_\gamma}$ the intensity of the incident x-ray beam, $I_{E_\gamma}$ the intensity of the attenuated beam, and $Z$, the atomic number of the material and $\mu(Z, E_\gamma) = \mu_{ph}(Z, E_\gamma) + \mu_c(Z, E_\gamma) + \mu_{pp}(Z, E_\gamma)$ as the linear attenuation coefficient. Between the absorption coefficients $\mu_i(Z, E_\gamma)$ and the cross sections $\sigma_i$ (i = ph, c, pp) exists the following correlation:

$$\mu_i(Z, E_\gamma) = \sigma_i(Z, E_\gamma) \cdot \varrho \cdot \frac{N_A Z}{A} \tag{2.8}$$

$N_A = 6.02 \cdot 10^{23}$ is the Avogadro constant, $A$ the nucleon number, and $\varrho$ the mass density of the material. Passing through a heterogeneous medium the beam is attenuated as follows:

$$I_{E_\gamma}(d) = I_{0,E_\gamma} \cdot \exp\left(-\int_0^d \mu(x, E_\gamma)\, dx\right) \tag{2.9}$$

$\mu(x, E_\gamma)$ is the absorption coefficient at position $x$ along the ray path. For a heterogeneous beam every energy bin is attenuated following equation 2.9. Due to the energy dependence of $\mu$ a heterogeneous beam changes its spectrum when passing through matter. Figure 2.11 exemplarily shows the energy dependence of $\mu$ for one certain $Z$ and its distribution in $\mu_{ph}, \mu_c$ and $\mu_{pp}$. Furthermore, it illustrates which of the three described interactions dominates the attenuation for different energies of the incident beam and different atomic numbers. As already shown in equation 2.3 photoionization plays its biggest role for high atomic numbers and low energies. Compton scattering mainly dominates for energies between some $100\,\mathrm{keV}$ and some MeV. In this work only photon energies up to maximum $6\,\mathrm{MeV}$ are considered. Pair production still has only little influence on photon absorption in tissue at these energies and therefore will be ignored for the rest of this work unless otherwise noted.
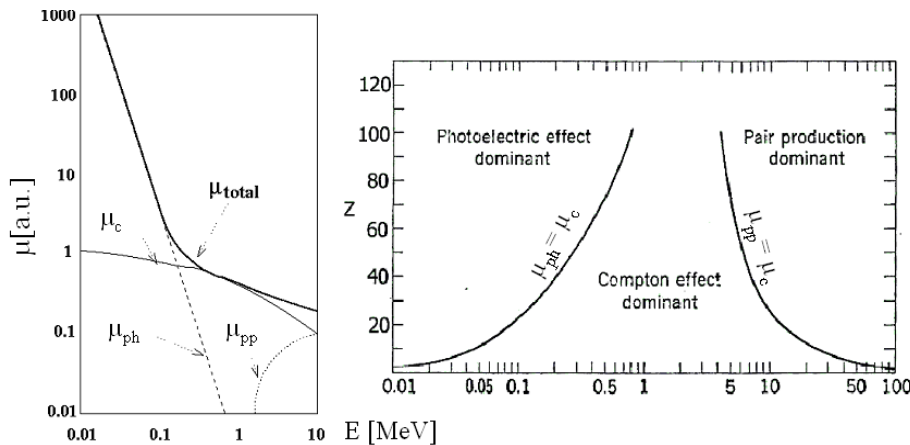


Figure 2.11: Absorption coefficients

*The left plot exemplarily shows the energy dependence of the absorption coefficient and its sum labelled as $\mu_{total}$. In the right picture the intersection points between the $\mu_{ph}$ and $\mu_{ph}$, $\mu_c$ and $\mu_{pp}$ are plotted for different atomic numbers Z. In this way it is shown at which energies x-ray attenuation is dominated by which interaction. Source of the right picture: [36].*

## 2.3   Aspects of image quality in projection radiography

In this section a monoenergetic beam and a detector of perfect efficiency and spatial resolution that is only sensitive to one photon energy is considered unless otherwise noted, i.e. only primary (attenuated) signal but no scattered photons or bremsstrahlung from secondary interactions is considered. Image quality of a radiograph is correlated to the required size and difference in x-ray absorption of two objects to be still distinguishable on the x-ray projection. Under the given assumptions image quality is mainly determined by the contrast and the signal-to-noise ratio (SNR).

**Contrast.** The contrast $C = \frac{|N_1 - N_2|}{N_1 + N_2}$ is defined as the normalized difference between two transmission signals $N_1$ and $N_2$, that are directly correlated to the absorption coefficient $\mu_1$ and $\mu_2$ and therefore energy dependent. Figure 2.12 compares energy dependence of the mass absorption coefficients $\frac{\mu}{\varrho}$ of bone, muscle and fat. The dominance of photoionization (see figure 2.11) and
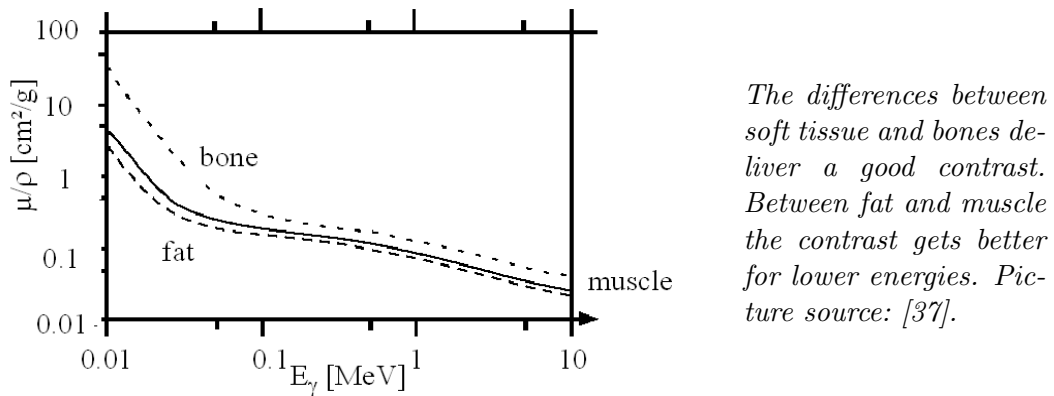


The differences between soft tissue and bones deliver a good contrast. Between fat and muscle the contrast gets better for lower energies. Picture source: [37].

Figure 2.12: Mass absorbtion coefficients for tissue

the resulting bigger differences in $\frac{\mu}{\varrho}$ yield better contrasts for lower energies. Practically, energies $E_\gamma < 25\,\mathrm{keV}$ do not deliver sufficient transmission signals and thus are not suitable for x-ray imaging.

In the presence of (a homogeneous distribution of) scatter signal on the detector the contrast reduces to $C_S$:

$$C_S = \frac{1}{1+\delta} C; \qquad \delta := \frac{2S_S}{S_1 + S_2} \tag{2.10}$$

$S_S$ is the detector signal produced by scattered radiation, $S_1$ and $S_2$ the transmission signals on the detector. $S_1$ and $S_2$ are proportional to the numbers $N_1$ and $N_2$ of the transmitted photons (per area). Due to the energy dependent detector efficiency in general $\frac{S_S}{N_S} \neq \frac{S_i}{N_i}$ with: $i = 1, 2$ and $N_S$: number of scattered photons (per area).

Examples for $\delta$: Thorax projection: $\delta \approx 2$; Abdominal projection: $\delta \approx 7$. In these cases the signal on the detector is mainly produced by scattered, rather than by transmitted, photons. This problem can be reduced by the use of an antiscatter grid. An antiscatter grid is attached at the detector front and contains high absorbing closely spaced lines that are focused towards the x-ray source. It is therefore intended to transmit primary radiation and absorb scattered radiation.

**Signal-to-noise ratio.** The spatial resolution is associated with statistical fluctuations of the number of photons per area. Assuming a Poisson distribution for it the SNR, defined as the quotient of the signal to its fluctuation, is proportional to $\sqrt{N}$. Therefore, increasing the photon fluence $\Phi$ leads to an increased SNR. A certain SNR can be achieved for a spatial resolution $\delta s$ for a detectable contrast of different numbers of photons $|N_1 - N_2|$ by a fluence:

$$\Phi \approx \frac{1}{|N_1 - N_2|} \left( \frac{\mathrm{SNR}}{\Delta s} \right)^2 \tag{2.11}$$

The absorbed dose $D$ can be estimated as:

$$D \approx \frac{\mu(E_\gamma)}{\varrho} \, E_\gamma \, \Phi \tag{2.12}$$

Figure 2.13 exemplarily outlines the expected dose exposure to detect a muscle-fat contrast and a bone-fat contrast for a given SNR as a function of $E_\gamma$. This example is representative for a tissue
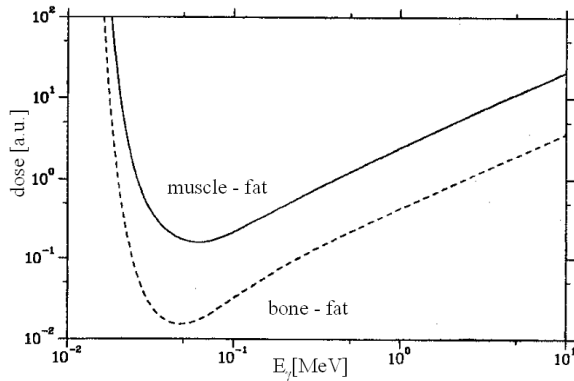


*The imaging dose needed to detect a muscle-fat or bone-fat contrast for a certain SNR exemplarily for a tissue thickness of approximately 10 cm is plotted. The curves have their minima in the energy range of approximately 40-50 keV. Picture source: [37].*

Figure 2.13: Energy dependence of expected dose exposure

thickness of approximately 10 cm. The lowest dose is expected for an energy range of 40-50 keV. For thicker objects the opportune range shifts to higher energies (e. g. 50-80 keV for a tissue thickness of approximately 30 cm).

## 2.4 X-Ray generation and x-ray spectra

For x-ray generation electrons are accelerated to a previously determined energy $E_{e^-}$ and stopped in a target (i. e. the anode in an x-ray tube) by emitting bremsstrahlung. This may happen in one or, more likely, in several steps. In this way an x-ray spectrum with a maximum photon energy of $E_{\gamma,max} = E_{e^-}$ is produced. This spectrum is overlaid by characteristic x-rays resulting from recombination after inner-shell electron interaction and ionization of the target atoms. The low energy photons of the produced spectrum are absorbed within the target so that x-ray spectra as shown in figure 2.14 are emitted[1]. The mean energies $\overline{E}$ of the plotted spectra are approximately 1.8 MeV for the 6 MV spectrum and 51 keV for the 120 kV spectrum. The lower energy part of the x-ray tube spectrum that is not suitable for imaging can be removed by additional filtering (beam hardening). For medical x-ray tubes a filtering of at least 2.5 mm aluminium is mandatory. This shifts the mean energy of the shown spectrum to approximately 56 keV.

The three most important parameters for the acquisition of an x-ray projection with a given x-ray tube are (i) the tube voltage $U$, (ii) the anode current $I$, and (iii) the pulse length $t$. The tube voltage is the potential difference that accelerates the electrons before they hit the anode for x-ray generation. $U$ is not only proportional to $E_{\gamma,max}$ but also to the efficiency $\eta$ of the energy conversion from electron energy to beam energy:

$$\eta \propto Z \cdot U \tag{2.13}$$

In summary, changing $U$ influences $E_{\gamma,max}$, $\overline{E}$ and the spectral fluence $\Phi(E_\gamma)$. The product $I \cdot t$ is the electrical charge that hits the anode during the x-ray pulse. This product has no influence on

---

[1]The kV-spectrum was simulated with the *x-ray toolbox* that is provided at a the internet by *Siemens Vacuum Technology Division*. It uses algorithms described in [38] – [40]. The MV-spectrum was obtained from Monte-Carlo simulations [41].

the shape of the spectrum but only on the absolute fluence: $I \cdot t \propto \Phi(E_\gamma)$. Therefore, $I \cdot t$ is also proportional to the imaging dose[2]
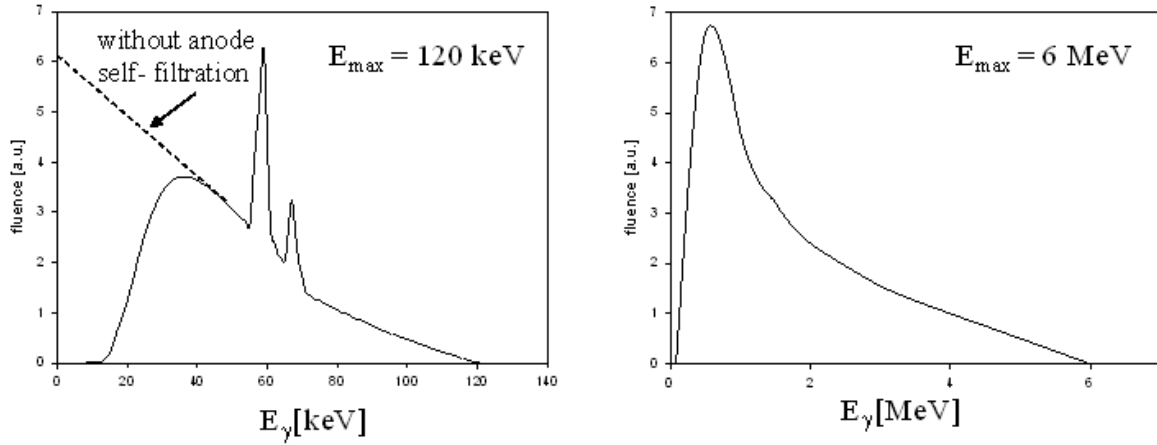


Figure 2.14: X-ray spectra for different $E_{e^-}$

*Left: 120 kV x-ray spectrum of an x-ray tube with tungsten anode without additional filtration. The bremsstrahlung spectrum is overlaid by two visible characteristic lines. The dashed line outlines the gradient of the initial bremsstrahlung spectrum without any filtering. Right: Example of a 6 MV x-ray spectrum. This plot represents the exit spectrum of a linac behind the flattening filter. No characteristic lines are present at high energies.*

## 2.5   Computer Tomography

A radiograph is the x-ray shadow of the imaged object providing only the total attenuation as a set of line integrals

$$p = -\log\left(\frac{I}{I_0}\right) \overset{(2.9)}{=} \int \mu(x)\, dx \tag{2.14}$$

along the ray path. Here, and in the remainder of this section the same assumptions as for section 2.3 are made (monoenergetic beam, ideal detector, no scattered radiation, unless otherwise noted). Figure 2.15 outlines the projection of one 2D slice from a certain projection angle $\Theta$ with parallel beam geometry (no beam divergence). Generally the total attenuation of an x-ray at position $u$, on the projection at angle $\Theta$, is given by the line integral:

$$p(u,\Theta) = \int \mu(x,y)\, ds \tag{2.15}$$

or with the coordinate system in figure 2.15:

$$p(u,\Theta) = \int\limits_{\infty}^{-\infty} \int\limits_{\infty}^{-\infty} \mu(x,y)\delta(x \cdot \cos\Theta + y \cdot \sin\Theta - u)\, dx\, dy \tag{2.16}$$

This function is called *Radon transform*. CT provides the slice data $\mu(x,y)$ by calculating the inverse Radon transform. For that purpose projections from every projection angle $\Theta$ are required. Because $p(u,\Theta) = p(u,\Theta + \pi)$ only an angular range of $\Theta = [\Theta_{start} \ldots \Theta_{start} + \pi]$ needs to be scanned. Theoretically, it is possible to analytically invert the Radon transform. To do so the following steps have to be performed:

---

[2]In this section, $I$ was used for the anode current. In the remainder, it is again also used for the beam intensity. If the physical value, that is represented by $I$ is self-explanatory, it might not be stated explicitly.
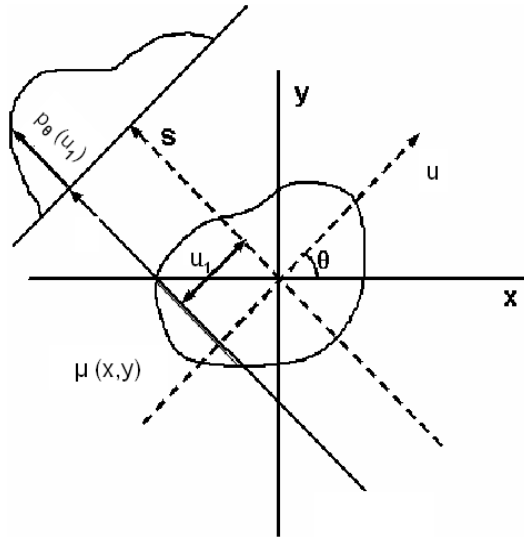
*Each projection is made up of the set of line integrals through the object. To obtain the slice data $\mu(x,y)$ projections over a range of 180 degree are required.*

Figure 2.15: Parallel beam geometry

1. *Fourier transform* of $p_\Theta(u) \rightarrow P_\Theta(\nu)$;

2. *Multiplication* of $P_\Theta(\nu)$ with $|\nu| \rightarrow P_\Theta^\star(\nu)$;

3. *Inverse Fourier transform* of $P_\Theta^\star(\nu) \rightarrow p_\Theta^\star(u')$;

4. *Back projection* of $p_\Theta^\star(u')$ and *integration* over $\Theta \rightarrow \mu(x,y)$.

This procedure is called *filtered back projection*. Back projection means 'smearing back' along the projection lines. The back projection under a certain angle $\Theta$ can be expressed as $\mu(\mathbf{r}) = p_\Theta(\mathbf{r} \cdot \hat{\mathbf{n}}_\Theta)$ where $\mathbf{r} = (x,y)$ and $\hat{\mathbf{n}}_\Theta$ the normal vector of the projection direction.

However, the inverse Radon transform proves to be unstable with respect to noisy data. In practice, a stabilized and discretized version of the inverse Radon transform is used. Indeed, practically, only a discrete sampling of $\Theta$ and $u$ is possible. The sampling rate of $u$ is limited by the detector resolution, and the maximum sampling rate of $\Theta$ depends on gantry rotation speed, detector frame rate and tube power. The influence on image quality is discussed in chapter 6.

For the patient in treatment position the $(x,y)$-plane in figure 2.15 corresponds to the $(x,y)$-plane of the patient coordinate system and the tube angle is given by $\gamma_t = \Theta$. Generally, x-ray sources produce divergent beams. Therefore, a *fan beam geometry* is applied for CT acquisition that needs to be taken into account for CT reconstruction. For fan beam CT acquisition the angular scanning range must be increased to at least $\Theta = [\Theta_{start} \ldots \Theta_{start} + 180° + \varepsilon]$ where $\varepsilon$ is the fan angle, which is the angle of the divergent beam opening that is needed to project the whole extent of the scanned object's u-dimension at every $\Theta$. To image a complete 3D volume every slice must be scanned. This can be done by constantly moving the object (or the imaging system) in the z-direction while repeatedly rotating the imaging system (i.e. the x-ray source and the detector) around the object. This technique is called spiral CT. For linac integrated CT acquisition a multiple rotation is neither technically possible nor suitable due to the time requirement (maximum rotation speed of a linac is 300° per minute). To image multiple slices without performing multiple rotations, CBCT is applied by opening the x-ray field in the v-direction for the *cone angle* and using an area detector. The cone angle is the angle of the divergent beam needed to project the extent of the volume to be scanned in v-direction. This *cone beam geometry* is taken into account for CT reconstruction by an algorithm developed by *Feldkamp*, *Davis*, and *Kress* (FDK-Algorithm) [42].

**Extension of the field of view.** The transversal field of view (FOV) at the isocenter for a CBCT acquisition is determined by the source to isocenter distance (SID), the source-to-detector distance (SDD), the $u$-dimension of the detector's active area $b$, the fan angle and the distance $|d| < \frac{b}{2}$ of

the detector center in $u$-direction (i. e. the *detector shift*). Assuming a fixed SID, a fixed SDD, a fixed $b$ and a fan angle that is large enough to always irradiate the complete $u$-dimension of the detector, the field of view for a centered detector ($d = 0$) can be extended by a lateral shift of the detector ($0 < |d| < \frac{b}{2}$). The geometry is illustrated in figure 2.16.
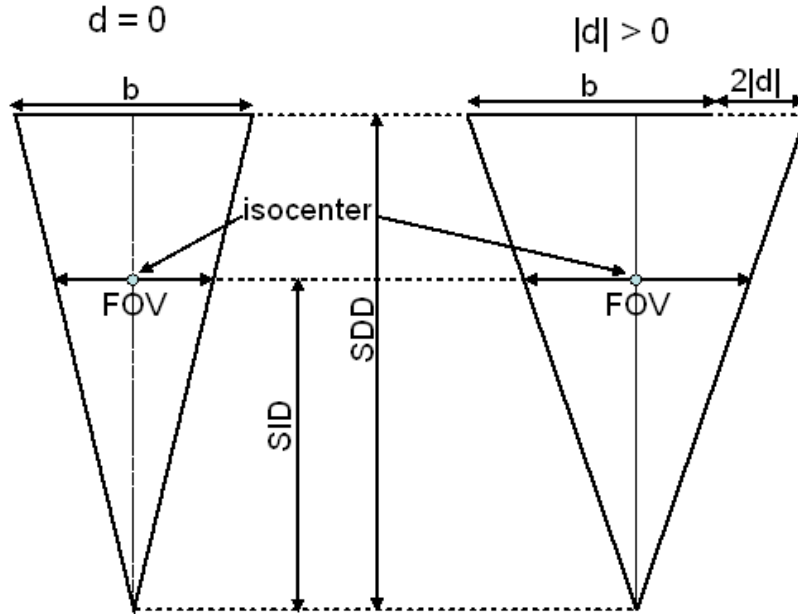


Figure 2.16: FOV extension

*Projection geometry for centered (left) and shifted detector (right). The FOV can be enlarged by a lateral shift of the detector. The projection truncation is compensated for by acquiring a 'full scan' CBCT.*

The FOV is given by FOV $= (b + 2|d|) \cdot \frac{\text{SID}}{\text{SDD}}$. For $|d| > 0$ the projection redundancy for angular scan ranges of more than 180° is no longer given. Therefore, the full angular range of 360° needs to be scanned ($\Theta = [0 \dots 360°]$). The projections are truncated at one edge, but all parts of the FOV will be covered in at least half of the projections for $|d| < \frac{b}{2}$. The shifted detector geometry must be taken into account for CBCT reconstruction. Methods to correctly reconstruct images from projections acquired with the asymmetric detector set-up are described in [43], [44]. Throughout this work the detector is placed at its centered position ($d = 0$) unless otherwise noted. A CBCT scan of the full angular range of 360° is named *full scan*, and a scan over (significantly) less than 360° is named *short scan*.

**Hounsfield units.** As already mentioned CT reconstructions yield the absorption coefficients $\mu_{E_\gamma}(x, y, z)$ of the scanned volume for the energy $E_\gamma$ of the imaging beam. Due to the energy dependence of the absorption coefficients a comparability of CTs acquired with different energies (in practice, different energy spectra) may be complicated. Therefore, instead of absorption coefficients *Hounsfield Units* (HUs) are commonly used for CT display. HUs are defined as

$$H := \frac{\mu - \mu_w}{\mu_w} \cdot 1000 \tag{2.17}$$

where $\mu_w$ is the absorption coefficient of water for the respective energy spectrum. Therefore, $H$ gives the per mil difference of absorption coefficients to water. By definition, $H_w = 0$ for water and $H_a \approx -1000$ for air. Soft tissue HUs usually range between -100 and 100 for soft tissues and up to $2000 - 3000$ for bones.

# Chapter 3

# Linac integrated kV-imaging

Though radiotherapy is an effective modality for tumor treatment, ionizing radiation may also cause serious side effects on healthy tissue. Ideally, the complete tumor volume receives the prescribed dose and the rest of the body as little dose as possible during the treatment course that all tumor cells are killed and no side effects occur. In practice, when planning a treatment, the therapist often needs to carefully balance deliverable dose distributions and the probabilities of these mostly contradictory requirements, especially if there are organs-at-risk (OARs) close to the tumor volume. Treatment planning is usually performed on a CT, which provides a snapshot of the patient's anatomy a few days before the beginning of the treatment. The following things may cause hypothetical static conditions to differ from the reality at the time of treatment:

- Positioning errors of the patient (the patient has to be positioned by technical personnel for each fraction),

- inter-fractional anatomical changes (organ motion, gain or loss of weight, fill levels of organs like bladder or stomach, tumor regression, ... ),

- intra-fractional motions (e. g. breathing, peristalsis, ... )

X-ray imaging modalities inside the treatment room provide the possibility to acquire real time information of the patient's anatomy at the time of treatment. With the acquisition of a CT at the intended treatment position one can determine the real position of the patient with respect to the planned treatment position and correct for it by a corresponding movement of the table. Ideally, positioning errors can be eliminated by this technique. Although, inter-fractional anatomical changes cannot be avoided, they can be observed, their impact may be evaluated and the therapist may react accordingly. Intra-fractional organ motion, especially breathing motion, can be followed by fluoroscopic imaging during dose delivery. Therefore, a good location for the in-room imaging system is the treatment machine itself. Linac integrated kV-imaging has the potential to combine all of these features. Since the linac already generates x-rays for treatment it may seem redundant to use an additional kV-x-ray imaging system instead of simply mounting a detector at the opposite side of the gantry. In the following section the differences between kV- and MV- photon energies for x-ray-imaging are discussed.

## 3.1   Imaging properties of kV- and MV-beams

The interaction between radiation and matter and its influences on absorption coefficients are described in chapter 2. In figure 2.12 it is shown that tissue contrast decreases with increasing photon energy. Therefore, kV-spectra are expected to deliver a better contrast that MV-spectra. Although theoretically an arbitrary SNR can be reached for imaging by increasing the imaging dose, for radiation protection purposes the patient should only be exposed to the necessary amount

of dose. The imaging dose to obtain a certain SNR is plotted in 2.13. Again the optimal imaging energies are in the kV-spectra. As outlined in equation 2.10 the contrast is decreased by scattered radiation. Basically it is not the amount of scattered radiation itself that influences the image quality but the scatter to primary ratio $\frac{S_S}{S_P}$ (SPR). The primary signal $S_P$ is the signal produced by the transmitted photons of the incident beam. That means for a linear detector response $S_P = S_0 \cdot \exp(-p)$ (equation 2.14) and $S_{tot} = S_S + S_P$, where $S_{tot}$ is the total signal and $S_0$ the signal of the non-attenuated beam. In presence of scattered radiation the Radon transform $p$ becomes

$$p_s = -\log\left(\exp(-p) + \frac{S_S}{S_0}\right) = \log S_0 - \log(S_p + S_S) \tag{3.1}$$

For $S_S < S_P$ this expression can be approximated by its Taylor series to

$$p_s \approx p - \frac{S_S}{S_P} \tag{3.2}$$

Thus, it is the SPR that goes into the Radon transform. The scattered photons are only produced by Compton scattering. Photons generated by secondary interactions of photoionization (e.g. production of bremsstrahlung) play nearly no role in x-ray imaging and can be neglected. A very rough approximation of the energy dependence of the SPR can be made using equations 2.7 and 2.8:

$$\text{SPR}\,(E_\gamma) \propto \frac{\mu_c(E_\gamma) \cdot d}{\exp[-\mu(E_\gamma) \cdot d]} \tag{3.3}$$

Here $d$ is the given path length through the imaged object. The energy dependence of the angular scatter distribution and any kind of secondary interactions of the scattered photons are is neglected, as is the energy dependence of the detector response (every photon is assumed to generate the same detector signal). Equation 3.3 together with equation 3.2 and equation 2.14 indicate a $d$-dependence of the scatter signal caused error at the reconstructed attenuation coefficients. A higher underestimation of $\mu$ for lower path lengths results in cupping artifacts at the reconstructed $\mu$-distributions.

Because both, $\mu$ and $\mu_c$ are monotonically decreasing within the interesting energy range (up to maximum 6 MeV) the SPR is also expected to decrease with increasing $E_\gamma$ considering equation 3.3. Figure 2.11 illustrates the dominating interaction processes against atomic number and photon energy. In the range of photoionization domination the SPR is expected to strongly decrease due to the strong energy dependence of $\mu_{ph}(E_\gamma)$. The energy dependence of $\mu_c$ is rather low and therefore only a slight decrease of the SPR is expected for a further increase in photon energy. Effective atomic numbers of tissue range between approximately 6 and 15. For such low atomic numbers Compton scattering is already involved for kV-energies and photoionization nevertheless plays an important role for photon absorption. In the range of MV-energies Compton scattering is the only noticeable interaction. Taking into account the angular distribution of the scattered photons, the primary direction of the MV-scattered radiation is forward towards the detector (see figure 2.9). That means for MV-imaging a higher ratio of the scattered photons will hit the detector and produce a disturbing signal than for kV-imaging. The angular distribution, together with the equation in figure 2.8, also show that $\Delta\lambda$ is more likely higher for photons of lower energies (i.e. higher wavelengths) than for photons of higher energies. That means scattered photons from primary kV-spectra have more likely lower energies than those from primary MV-spectra. Hence, they will more likely be absorbed in the scattering object itself and therefore produce no scatter signal on the detector.

In summary kV-spectra are expected to be more appropriate for x-ray imaging than MV-spectra. The Inline concept for linac integrated kV-imaging is described in the following section.

## 3.2 The Inline Concept

A sketch of the Inline concept for IGRT is presented in figure 3.1. The different components are



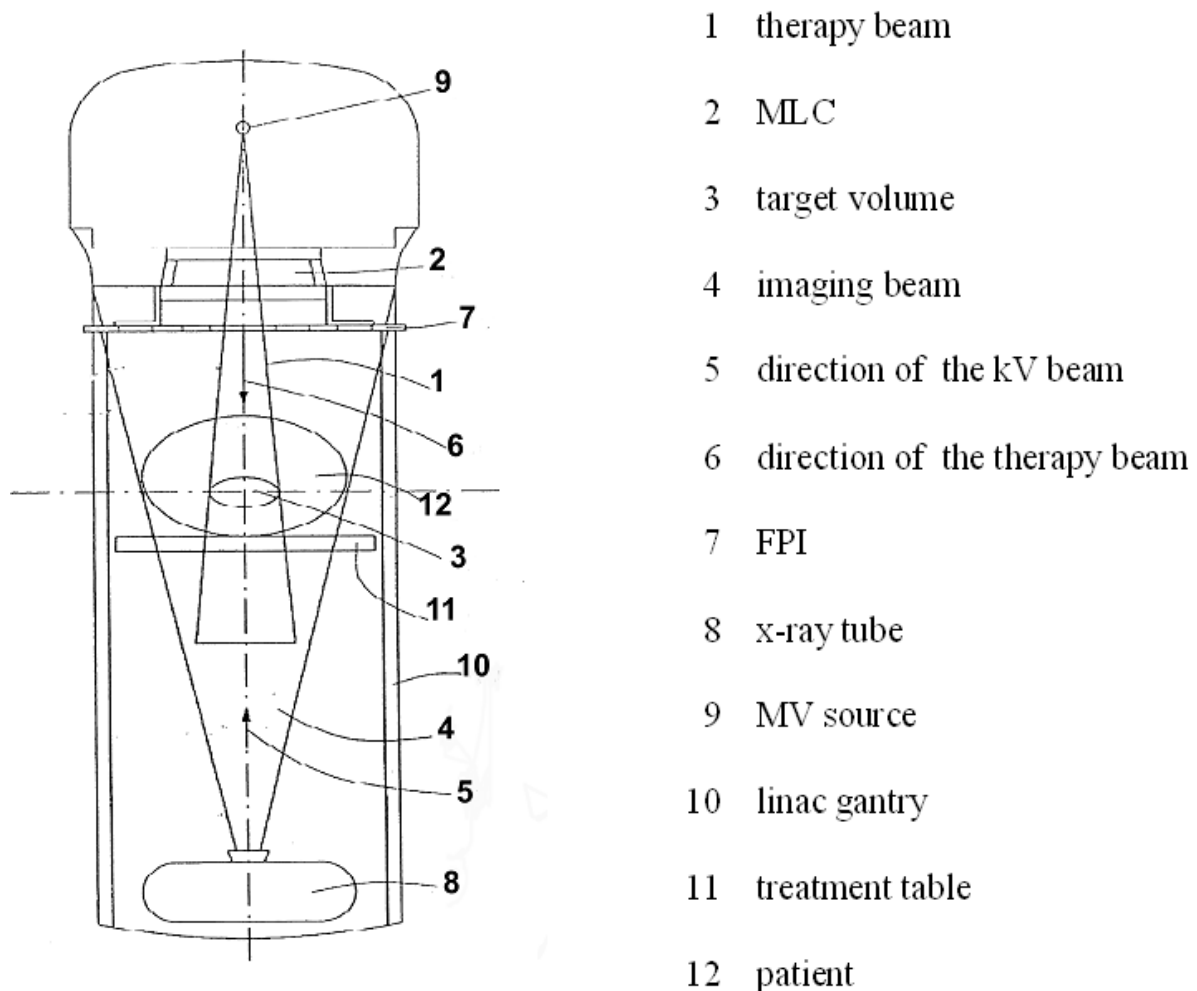| | |
|---|---|
| 1 | therapy beam |
| 2 | MLC |
| 3 | target volume |
| 4 | imaging beam |
| 5 | direction of the kV beam |
| 6 | direction of the therapy beam |
| 7 | FPI |
| 8 | x-ray tube |
| 9 | MV source |
| 10 | linac gantry |
| 11 | treatment table |
| 12 | patient |

Figure 3.1: Inline concept

*The essence of the Inline concept is the kV-imaging system consisting of an x-ray tube installed at 180° with respect to the treatment beam, and the dedicated FPI installed at the treatment beam exit right below the MLC. With this configuration both the kV- and the MV-beam can be monitored by a single detector. Furthermore besides the acquisition of CBCTs intra-fractional organ motion perpendicular to the treatment beam can be observed by kV-imaging during beam delivery. This sketch of the Inline concept shows the alignment of the different components, which are described in more detail in the text. Picture source: [28].*

described below: The MV-beam (1) is generated by the MV source (9) and directed to the target volume (3). The beam is modulated by the MLC (2) in accordance with the treatment plan to deliver a specified dose distribution to the patient (12) lying on the treatment table (11). The x-ray tube (8) is mounted at the gantry (10) at the opposite side of the MV source. Therefore, the direction (5) of the central ray of the imaging beam (4) is 180° with respect to the direction of the central ray of the therapy beam (6). The FPI (7) is installed directly below the MLC perpendicular to the beam directions and with its front plane towards the x-ray tube. The kV-beam can be rectangularly collimated to adjust for the size of the volume to be imaged. The

FPI detects the transmitted x-rays after its passage through the patient for imaging purposes. By rotating the gantry, patient projections can be acquired from any direction in the $(x, z)$-plane of the room coordinate system (figure 2.3). This option allows the acquisition of CBCTs of the patient in treatment position. For dose delivery the MV-beam always traverses the FPI. Thus the shape and the intensity of the treatment beam is continuously monitored. Optionally, an additional FPI can be installed for MV- imaging purposes at the opposite side of the MV source right above the x-ray tube and with its front plane towards the MV-beam (not shown in figure 3.1). With this FPI, MV-projections of the patient from every gantry angle, and therefore also MV-CBCTs, could be acquired. Furthermore, during dose delivery the transmitted radiation of the treatment beam after its passage through the patient could be monitored. Removing any scattering object between the MLC and the FPI (i. e. the upper FPI, the patient and the treatment table), the shape of the MV-beam can be monitored with a higher spatial resolution than with the upper FPI. This is due to the beam divergence and the larger distance to the beam source.

Besides the usual dose delivery, possible features of a treatment machine following the Inline concept for linac integrated kV-imaging are:

**Detection and corrections of set-up errors:** A treatment plan is generated on the basis of a planning CT that has been acquired before the start of the treatment course. The transformation from the patient coordinate system to the room coordinate system (i. e. $[x_0, y_0, z_0]$ from equation 2.1), and thus the position of the (immobilized) patient in the treatment room, is determined at treatment planning. On every treatment day the patient should be placed exactly at the same position. By acquiring a CBCT of the immobilized patient in the position adjusted by the RTT for treatment, residual set-up errors can be detected. Because the CBCT is acquired with a linac-integrated and calibrated imaging system the coordinates of the isocenter are fixed. Therefore, the deviation of the actual patient position to the specified position can de determined by a spatial match of the CBCT and the planning CT data. Assuming a pure translation the position can be corrected by a table shift.

**Detection and corrections of patient's anatomy:** If there are changes of the patient's anatomy between the single treatment fractions they can also be detected by CBCT acquisition and comparison to the planning CT or the last acquired CBCT. If necessary, a short-term adaptation of the treatment plan to the given anatomy, including the actual patient position, prior to each fraction is imaginable.

**Calculation of actual delivered dose.** Changes in the patient's anatomy may lead to deviations in the delivered dose distribution compared to the expected one predicted by the treatment plan. The acquisition of a patient CBCT in treatment position prior to a treatment fraction may allow the calculation of the actual dose distribution on the basis of the applied treatment plan. Possible table shifts for patient positioning can be taken into account.

**Real-time tracking of tumor and organ motion\*:** For tracking or control of tumor and organ motion, 2D projections or fluoroscopic sequences of the patient can be acquired at any time during a treatment fraction. This information may be used to react online to any kind of intra-fractional motion. Especially for lung cancer cases, it is possible to monitor the breathing motion of the patient and to adapt the dose delivery online on the basis of these images. This could, for instance, be done either by gating the treatment beam on a certain tumor position window, i. e. the treatment beam is interrupted as soon as the tumor moves out of a determined region on the kV-projection, or by following the tumor motion with the MV beam shape by means of the MLC. In this case the MLC shape could be adapted online to a recent or, in case of motion tracking, a predicted tumor position.

**Treatment control by overlay of treatment beam and patient projection\*:** By simultaneously acquiring an x-ray projection of the patient and monitoring the treatment, the beam shape can be mapped on the patient projection. Due to the divergent beam geometries the

reproduction scale of both beam projections on the detector needs to be taken into account for this purpose. That means the MV-beam size must be stretched on the projection to a virtual size reflecting its real size in the patient. The resulting image can be used for treatment control purposes, to check, for instance, whether the beam hits the intended part of the anatomy.

**Independent monitoring of beam delivery\*:** The control system of a linac examines the delivered fluence and the shape of the single treatment segments via the monitor chambers and the MLC encoders or potentiometers. The Inline concept provides a redundancy of the dose delivery control. The beam shape and its intensity can be analyzed online by monitoring the treatment beam with the FPI. Deviations of the actual applied beam from its treatment plan description may be handled by an immediate beam interruption.

**Entrance dosimetry\*:** Treatment beam monitoring can also be used for dose reconstruction [45] – [47]. Independently from the treatment plan, the actual delivered dose distribution can be calculated on the basis of the actual applied beam shapes and 2D-intensities. A dose calculation can be performed on the planning CT or, if applicable, on the CBCT acquired prior to the particular treatment fraction. The delivered dose distribution can be used for treatment control purposes and for inter-fractional treatment plan adaptations dealing with deviations from the planned dose distribution.

**MLC-QA\*:** MLC calibration can be performed with the FPI [48], [49]. This can be done by moving the single leaves to prescribed positions during beam monitoring. The actual leaf positions and leaf speeds may be analyzed real-time and compared to the expected ones. Online adjustments may be performed on the basis of the observed deviations. This process may then be repeated until the accuracy of the MLC calibration is within a specified tolerance.

The features marked with * either require the special Inline set-up (kV-imaging axis coincides with MV-beam axis)[1] or their outcome differs from alternative setups (e. g. 90 degree solutions). For CBCT acquisition, the mounting position of the kV-imaging system with respect to the treatment beam does not matter. With the Inline configuration real-time tracking of tumor and organ motions perpendicular to the treatment beam is possible. Motion along the image beam direction is not observable (if beam divergence caused changes of the projection size are neglected). Alternative configurations using a kV-imaging axis perpendicular to the MV-beam axis allow to observe motion along the MV beam direction but are not able to track motion along both axes perpendicular to the treatment beam. Generally, photon dose distributions are less sensitive to organ movements along the beam axis than perpendicular to it. This issue is discussed in detail in [50]. Any applications dealing with MV-beam monitoring are naturally infeasible with 90 degree solutions. For that purpose a second FPI for MV-beam detection, and possibly a synchronization with the FPI belonging to the kV-imaging system, would be needed.

In this work, a prototype of a linac integrated kV-imaging system following the Inline concept was developed. The following chapters report on the different development stages of the project, starting with the construction of an experimental kV-imaging platform, to the point of integrating the kV-imaging components at a research linac, and finally lead to a stable IGRT device for patient applications. Finally, the first commercial version of this setup is introduced.

---

[1]It is assumed the only the one FPI, used for kV-imaging is installed at the linac.

# Chapter 4

# The x-ray wagon

The first step in the evolution of the Inline prototype was the construction of a bench top system as an experimental setup to simulate linac integrated kV-imaging. A photo and the design of this *x-ray wagon* are shown in figure 4.1. With this construction, single x-ray projections of a phantom
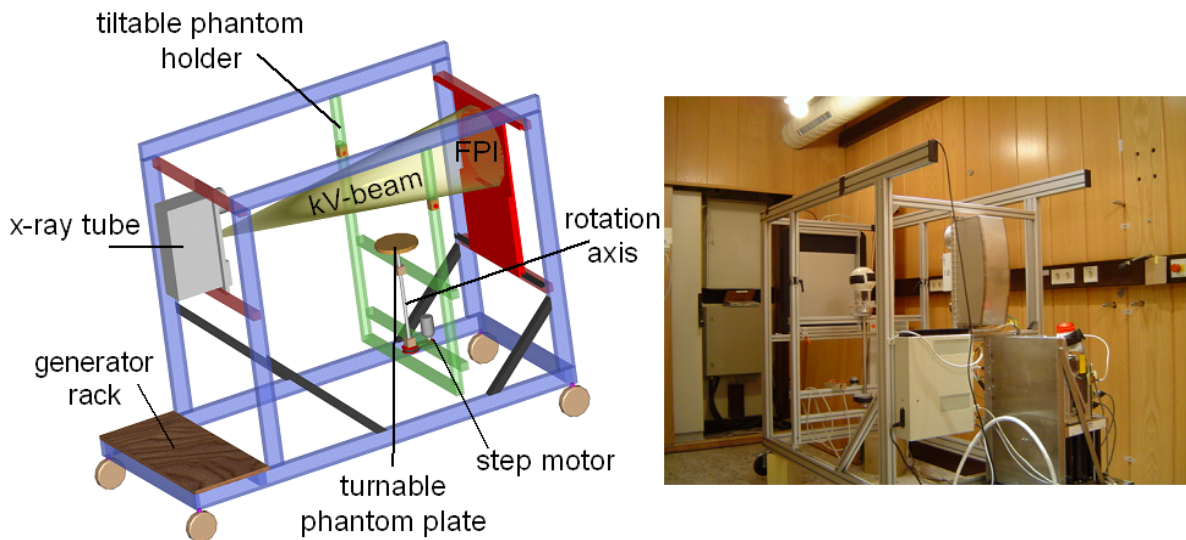


Figure 4.1: X-ray wagon

*The x-ray wagon bench top system mainly consists of an aluminium frame carrying an x-ray tube and a FPI and a rotatable plate driven via a shaft by a step motor. The detector can be shifted laterally and the rotation axis can be tilted towards the x-ray tube. On the photo a phantom is placed on top of the plate, the x-ray generator is mounted at the rack and a positioning module for the step motor is installed next to the generator.*

fixed on top of the phantom plate and CBCTs can be acquired due to the rotatability of the plate. The isocenter is the intersection point of the rotation axis and the central ray of the kV-beam. The dimension are: $SID = 100\,cm$ and $SDD = 150\,cm$. The detector can be shifted up to $10\,cm$ laterally for FOV extension. Furthermore, the rotation axis can be tilted towards the x-ray tube. This feature is intended for tomosynthesis [51] experiments and not further attended within this work; the rotation axis is always kept perpendicular to the x-ray beam direction.

Compared to a linac integrated kV-imaging system the y-axis of the room coordinate system corresponds to the rotation axis of the x-ray wagon, with positive coordinates above the isocenter. A CW-rotation of the gantry corresponds to a CCW-rotation of the plate (looking towards increasing y-coordinates) and vice versa. The FPI is fixed with its front towards the x-ray tube and the plug

connections towards the ceiling (positive y-direction), corresponding to cable plugs towards the
structure for a linac integrated kV-imaging system.


## 4.1    Components

The main components that are used for x-ray imaging with the bench top systems are the x-ray tube
(including the x-ray generator), the FPI and the step motor. Furthermore, an x-ray imaging control
system was developed to handle the interaction of the single components for image acquisition. The
principles and the properties of these components are described in this section.


### 4.1.1    X-ray tube and x-ray generator

The x-ray tube *P 125/10/20 CR* embedded in the *POWERPHOS* housing, and the x-ray generator,
are taken from the commercially available *Siemens POWERMOBIL* C-arm system. The technical
data of these components are summarized as follows:

**Generator**

| | |
|---|---|
| Type | HF-generator |
| Power (IEC 60601 [52]) | 15 kW |
| Max. pulse power | 20 kW |
| kV-range | 40 kV to 125 kV |
| Anode current (DCM) | up to 250 mA |
| Pulse frequency | up to 12.5 Hz |

**X-ray tube + housing**

| | |
|---|---|
| Type | Double-focus rotating anode, |
| Focal spot nominal value (IEC 60336 [53]) | small focus: 0.3; large focus: 0.5 |
| Nominal power | small focus: 10 kW; large focus: 20 kW |
| Inherent filtration (IEC 60601) | 2.5 mm Al; 0.1 mm Cu |
| Anode target anlge | 10° |
| Anode material | Rhenium-tungsten, molybdenum, graphite |
| Anode heat storage capacity | $2 \cdot 10^5$ J |
| Housing heat storage capacity | $1.9 \cdot 10^6$ J |
| Max. anode heat dissipation | 36,000 J/min |
| Max. average anode input power | 150 W |

The effective focal spot size is the focal spot area projected perpendicularly onto the image detector[1]. The anode angle is the tilt angle of the area where the electrons emitted form the cathode hit
the target to the beam direction. Both terms are illustrated on the left image of figure 4.2. The
x-ray beam's intensity is neither uniform nor symmetrical throughout its entirety. The anode-sided
point $A$ receives less intensity than cathode-sided point $C$. The decreased intensity at $A$ results
from emission which is nearly parallel to the angled target where there is increasing absorption of
the x-ray photons by the target itself. This is called the *heel effect* [54]. Generally, the steeper the
anode, the more severe or noticeable the heel effect becomes. The anode-sided beam collimation
should be adjusted to block at least the rays having a larger angle to the central beam direction
than the anode angle; the cathode-sided collimation, as well as the collimation perpendicular to the
cathode-anode direction may be opened wider. A large anode angle provides large radiation field
coverage but for a given effective focal spot size the actual focal spot track on the anode is narrower
compared to a smaller anode angle, resulting in a lower heat capacity. The influence of the focal

---

[1]The *IEC 60336* nominal focal spot value does not indicate the exact effective focus size, but gives the limits of
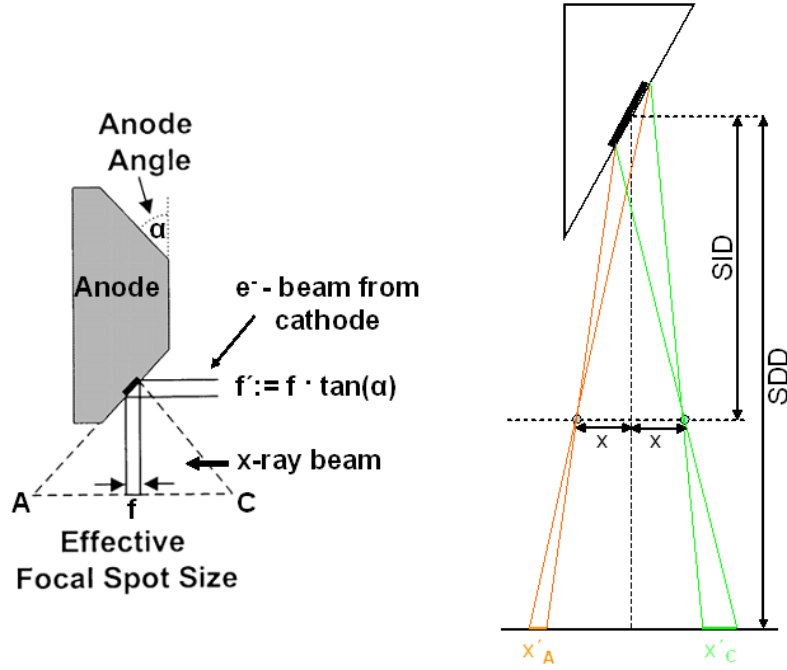both dimensions.

Figure 4.2: Anode design and effects on projection sharpness

*Left: 2D-anode geometry. The focal spot projected perpendicular onto the detector is a rectangular area (assuming an appropriate anode radius). Here, f is the dimension in the cathode-anode direction. The anode angle $\alpha$ defines the focus size on the anode and the magnitude of the heel effect, causing a lower intensity at point A than at point C. Right: Blurring of a punctiform object. The projection of the cathode-sided point is always more blurred than the anode-sided point at the same distance to the central ray.*

spot size and the anode angle on the spatial resolution or the sharpness of a projection is illustrated on the right side of 4.2. The picture shows how the projection of a point gets blurred due to a non-punctiform source. Obviously there is an asymmetry between anode-sided and cathode-sided points. It is:

$$x'_A = \frac{4f \tan \alpha \cdot (\text{SDD} - \text{SID}) \cdot (x - \text{SID} \cdot \tan \alpha)}{(f + 2 \cdot \text{SID} \cdot \tan \alpha) \cdot (f - 2 \cdot \text{SID} \cdot \tan \alpha)} \tag{4.1}$$

and

$$x'_C = \frac{4f \tan \alpha \cdot (\text{SID} - \text{SDD}) \cdot (x + \text{SID} \cdot \tan \alpha)}{(f + 2 \cdot \text{SID} \cdot \tan \alpha) \cdot (f - 2 \cdot \text{SID} \cdot \tan \alpha)} \tag{4.2}$$

leading to an asymmetry in blurring of:

$$\frac{x'_C}{x'_A} = \frac{\text{SID} \cdot \tan \alpha + x}{\text{SID} \cdot \tan \alpha - x} \quad > \quad 1 \tag{4.3}$$

The definition of the used variables are given in figure 4.2. The blurring perpendicular to the cathode-anode direction is homogeneous and does not show this asymmetry as one can easily imagine. It is $x_\perp = f_\perp \cdot (\frac{\text{SDD}}{\text{SID}} - 1)$ where $x_\perp$ is the blurring and $f_\perp$ the effective focus size perpendicular to cathode-anode direction. The x-ray tube was installed at the x-ray wagon with the anode at top (low x-values on the FPI) and the cathode at bottom (high x-values on the FPI). The SDD of 150 cm leads to maximum cone- resp. fan angle of 15.4°beam opening in to cover the complete $41 \times 41 \text{cm}^2$ area of the FPI[2]. A small focus was always used for image acquisition, unless otherwise noted [55]. For beam collimation an octagon-aperture was available that was initially adjusted to

---

[2]The anode-sided opening of the beam is therefore $\leq 7.7°$ and smaller than the anode angle.

cover the active area as much as possible without irradiating parts of the FPI beyond the active area.

**Generator control.** The electric power supply for the x-ray generator is provided by a common 230 V/50 Hz power socket. The generator is controlled via a serial EIA-232 port and a CAN bus port [56]. As the serial interface is mainly used for debugging and service purposes, the x-ray parameters (high voltage, anode current and focal spot) and the commands for anode rotation start and stop are sent via CAN protocol. During anode rotation x-ray pulses are triggered by the *SWR signal*. The length of this external hardware signal defines the pulse duration. X-ray generation starts as soon as the SWR signal rises and is stopped immediately when it falls. High voltage and anode current can be varied at any time even during anode rotation. The actual x-ray parameters may vary from those transmitted to the generator. Especially the anode current may not be constant over the complete pulse length, and the pulse lengths themselves may be shorter than the provided SWR signal. The generator measures the x-ray parameters and supplies the control software after each pulse with the actual applied pulse length, the average anode current and the high voltage via CAN protocol. These data are stored for each pulse together with a corresponding time flag, into a text file. A control of the tube load is not provided by the generator. The operator takes the responsibility for the adherence of the load charts.

### 4.1.2   Flat Panel Imager

The used FPI was the Radiation Image Detector *RID 1640 AL1* from *PerkinElmer optoelectronics*. This is an amorphous silicon FPI consisting of a phosphor (gadolinium oxysulfide ($Gd_2O_2S$)) and a matrix of photo diodes. The technical data are summarized in the following table.

<u>Sensor:</u>

| | |
|---|---|
| Pixel | $1024 \times 1024$ |
| Pitch | $400 \, \mu$m |
| Active area | $409.6 \times 409.6 \, \text{mm}^2$ |

<u>Electronics:</u>

| | |
|---|---|
| ADCs | 16 (16 bit) |
| Min. integration time | 286 ms |
| Saturation charge | $5 \, pC$ (at $5 \, V$) |

<u>Detector:</u>

| | |
|---|---|
| Non-linearity | $< \pm 1\%$ |
| Image lag | $< 8\%$ |
| Max. frame rate | $3.5 \, s^{-1}$ |
| Scintillator | $Gd_2O_2S : Tb$ (Lanex fast®) |

The FPI is based on amorphous silicon technology. The light sensitive photodiode array of $1024 \times 1024$ pixels is coupled to the scintillation material which responds to x-rays. Each pixel consists of a light sensing photodiode and a switching Thin Film Transistor (TFT) in the same electronic circuit. The incident x-rays are converted by the scintillator material to visible light which generates electron-hole pairs in the biased photodiode. The charge carriers are stored in the capacitance of the photodiode. By pulsing the gates of a TFT line within the matrix, the charges of all columns are transferred in parallel to the signal outputs. The signals of the columns are amplified in readout multiplexers for further processing. The rows are addressed by row drivers. For scintillator protection purposes a 0.6 mm aluminium plate is screwed at the detector's front plate. To protect the electronics from incident radiation, they are apart from the sensor in a frame around the active area of the detector. Therefore, the x-ray beams' size should always be restricted to the active area. The detector readout is controlled by a PC via a PCI frame grabber that supplies the PC with the imaging data. A corresponding imaging software (HIS) is supplied by the

vendor. The image data of one projection consist of an $1024 \times 1024 \times 16$ bit array, i.e. 16 bits per pixel yielding integer gray values between 0 and $2^{16} - 1 = 65535$ for each pixel. The gray value is proportional to the charge measured in the corresponding photodiode. Gray values cannot exceed the saturation threshold of 65535. Therefore, saturated pixels delivering a gray value of 65535 provide no quantitative information of the actual amount of radiation they received. Throughout this work all pixels are assumed not to be saturated unless otherwise noted.

**Image acquisition.** The detector readout can be triggered by external hardware signals (*external trigger mode*) or automatically in fixed time intervals of multiples of the minimum integration time (*free running mode*). The time difference between two external trigger signals must be at least the minimum integration time. Otherwise, the signal is ignored by the detector. Starting at the moment of the (internal or external) readout trigger, the charges of the photodiodes are transferred, row by row, to the signal outputs starting in the middle (y = 511 and y = 512) and ending at the edges (y = 0 and y = 1023). The readout time for the whole area coincides with the minimum integration time. The signal of x-ray pulses hitting the active area during a readout phase is split up in two frames in the following way. The signal of rows that have already been read out recently fully appears on the subsequent frame. The signal of rows that are read out during the x-ray pulse appears partly on the current and partly on the subsequent frame. The signal of rows that have not been read out until the end of the x-ray pulse fully appears on the current frame. Therefore, when performing x-ray imaging in a pulsed mode, the detector readout should be synchronized with the beam pulses, i.e. the detector readout should be triggered after the end of each pulse, and the subsequent pulse should not start before the end of the detector readout. If the FPI runs in external trigger mode and does not receive any trigger signal for approximately 20 seconds, it switches to free running mode to avoid dark current saturation and switches back to external trigger mode as soon as it receives the next trigger signal. For imaging acquisition, the imaging software needs to allocate main memory (one projection needs approximately 2 MB). The user can decide between the *continuous acquisition mode* that stores the projection data in a ring buffer of predefined size and runs until it is stopped by the user, or an *acquisition sequence* that is stopped after a predefined number of projections that are kept in the main memory.

**Offset correction.** Every raw image is overlaid by an integration time-dependent offset signal. This background signal should be measured by *dark image acquisition* (i.e. image acquisition with the corresponding integration time but without radiation) and subtracted from the raw image. Gray values of the dark images are usually in the range of approximately $3000 - 5000$. The maximum dynamic range (65535) of each pixel is reduced accordingly. Practically, for an acquisition of a projection sequence with (approximately) a constant frame rate (i.e. a constant integration time for each projection) a sequence of a few dozen dark images is acquired with the according frame rate prior to the actual sequence. The averaged gray values of each pixel are used for online offset correction provided by the imaging software. Saturated pixels are not offset corrected due to the lack of quantitative gray value information. Because neither a long term stability nor a linearity in the integration time dependence of the dark image gray values can be determined, an accurate prediction is not possible and, therefore, dark image acquisition should be performed at least every day and for each applied integration time unless they do not differ significantly. Throughout this work, all projections dealt with are already offset corrected unless otherwise noted.

**Gain- and open field correction.** As the gray values of the dark image varies from pixel to pixel, the FPI response on radiation is pixel dependent. This means that in general, a homogeneous x-ray beam causes different gray values on different pixels. The (offset corrected) detector signal $S(x, y)$ is proportional to the individual gain $g(x, y)$ of each pixel. For an non-attenuated x-ray beam the FPI response is:

$$S_o(x, y) \propto I(x, y) \cdot g(x, y) \tag{4.4}$$

where $I(x, y)$ is the intensity of the x-ray beam. Therefore, such an *open field projection* contains the FPI response and the inhomogeneities of the x-ray beam (caused for instance by the heel effect) as shown in figure 4.3. To obtain the line integrals dealt with in section 2.5, both effects are
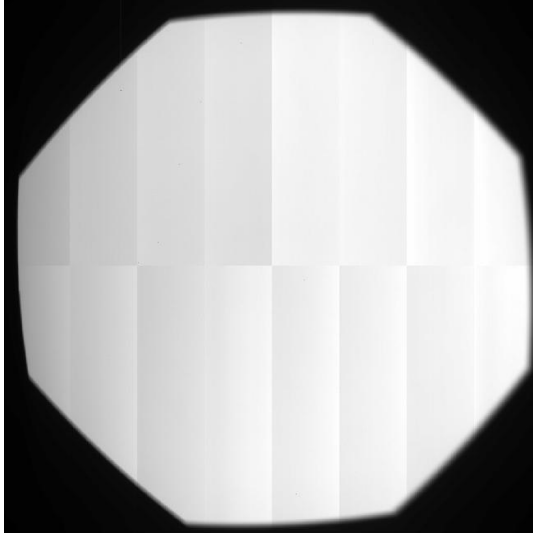


*The ADC structure of the FPI is visible on the open field projection as a pixel dependent FPI response. The increasing brightness towards the right side, which is the cathode-sided part of the image, is caused by x-ray beam inhomogeneities. The open field is margined by the octagon aperture. The increased blurring of the cathode-sided margin compared to the anode-sided margin is evident.*

Figure 4.3: Open field projection

corrected for by dividing the gray values $S_p(x, y)$ of an acquired x-ray projection by the open field projection gray values $S_o(x, y)$:

$$q(x, y) = \frac{S_p(x, y)}{S_o(x, y)} \tag{4.5}$$

Here, together with the assumptions of section 2.3, it is assumed that $S_p(x, y)$ is obtained with the same output ($U$ and $I \cdot t$) of the x-ray tube as $S_o(x, y)$. Practically, an average open field over a few dozen projections with the appropriate x-ray spectrum is acquired and used for off-line gain- and open field correction. Again, it is recommended to do so everyday to overcome long term instabilities. Differences in $I \cdot t$ can be considered by:

$$q(x, y) = \frac{S_p(x, y)}{S_o(x, y)} \cdot \frac{I_o \, t_o}{I_p \, t_p} \tag{4.6}$$

$I_x$, $t_x$: self-explanatory. Differences of $U_p$ and $U_o$ cannot be corrected for. Though an online correction is also provided by the imaging software, it is only suitable for a qualitative flatness correction of the projection.

**Dead pixels correction.** Unavoidably, a small fraction of the $1024^2$ detector pixel does not work properly. Under radiation, these *'dead' pixels* usually deliver significantly higher or lower gray values than the surrounding pixels and can therefore be easily identified. Dead pixel correction can be performed by replacing the gray value by the mean gray value of their eight neighboring pixels. Online dead pixel correction is provided by the imaging software on basis of dead pixel maps.

### 4.1.3  Drive mechanism

For the rotation control of the phantom plate a common 1.8° hybrid step motor was used. The step angle accuracy was increased using a 50:1 gear. Additionally, a belt drive with a gear reduction of 2.5 was used to drive the shaft in order to increase the gear's maximum torque of 4 Nm to 10 Nm. Therefore, a full 360° rotation of the phantom plate was divided into $\frac{360°}{1.8°} \cdot 50 \cdot 2.5 = 10,000$ steps yielding step angles of 0.0144°. The minimum rotation time is approximately 10 seconds. The motor is driven via a software controlled step motor positioning module. The positioning module

is installed at the x-ray wagon and connected to the control PC via a serial EIA-232 interface. Position measurement is provided by a 5000 lines incremental rotary encoder at the shaft with an accuracy of $\frac{360°}{5000} = 0.072°$. Encoder readout is provided by a PCI encoder counter board. The encoder counter is reset every revolution by the encoder's index crossing.

### 4.1.4 X-ray console

An *x-ray console* was built for the SWR signal supply and, therefore, for the triggering of the x-ray pulses. The software controlled console is connected to a PC timer- and digital I/O card. It features the following operational modes:

**Continuous radiation.** In this mode the signal rises and falls at the push of a button at the control software.

**Single shot** In this mode the signal rises once at the push of a button and falls after a predefined time interval.

**Pulsed radiation.** In this mode, at the push of a button, the SWR signals of a predefined length are generated with a predefined frequency. During a pulsed radiation sequence the pulse duration and the pulse frequency can be varied at the control software.

**Hardware triggered.** In this mode the generation of the SWR signals is triggered by external hardware signals via an digital input line of the x-ray console.

The operator can switch between the single operational modes at the control software, which sets the modes at the console by correspondingly setting the digital outputs of the PC card the console is connected with. The pulse duration and the pulse pause duration for the pulsed radiation mode can be set in unit intervals of one millisecond. These values are stored in the timer card and are accessed from there by the console.

For safety purposes the x-ray console contains a key switch for power supply, a release button and an emergency stop button. X-ray pulses can only be released if the key is turned, the door interlock is closed, the emergency stop button is released and the release LED is on. The release LED can be switched on and off by pressing the release button and switches off automatically when the door interlock is opened, the emergency button is pressed or the radiation sequence is finished (either by user interaction, by irradiation abort in the case of error or in single shot mode after the end of the pulse).
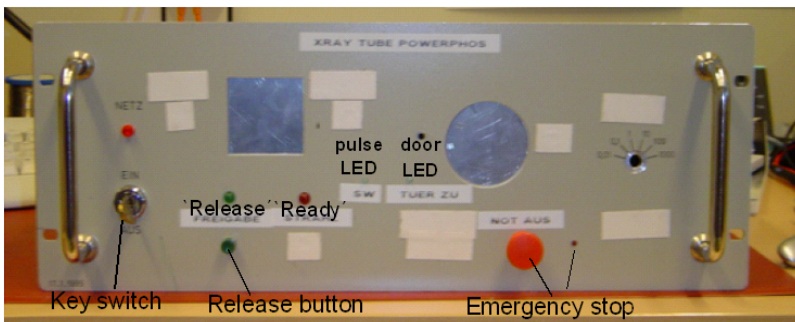


*The x-ray console provides the SWR signal for x-ray pulse triggering. LEDs indicate the beam release, the ready state of the x-ray tube, the x-ray pulses, and the states of the emergency button and the door interlock.*

Figure 4.4: X-ray console

Furthermore, the x-ray console features two digital outputs: The *rad-on* output provides a high TTL output signal that coincides with the SWR signal; the *ready* output provides a high output signal when the x-ray tube is ready for radiation (i. e. the anode rotates). The release button that switches between beam release and beam blocking can be used to interrupt and continue a

sequence, or to allow continuous irradiation without interrupting the x-ray tube's ready state. A photo of the x-ray console is shown in figure 4.4.

### 4.1.5   Detector readout trigger board

For triggering the detector readout, a detector readout trigger board (*trigger board*) was built. This box has two digital inputs, namely the *rad-on* input and the *ready* input that are connected to corresponding outputs of the x-ray console. The trigger signal is generated (with a short delay of about 1 ms) at the falling edge of the rad-on signal, i. e. at the end of every x-ray pulse. Furthermore, two to five trigger signals (switchable) at intervals of approximately 300 ms are generated at the rising edge of the ready-signal. This is for clearing the FPI offset- and lag signal prior to acquisition of an imaging sequence.

## 4.2   Image acquisition

Several methods of x-ray image acquisition are possible with the x-ray wagon:

**Single x-ray projection.**  For a single x-ray projection of a phantom placed on the phantom plate, at first the phantom can be rotated to the intended projection angle via the control software. This can be done by entering the absolute angular position or an angle (positive or negative) interval to be rotated, or by starting the rotation and stopping it as soon as the phantom is positioned correctly. The detector is run in external trigger mode and the x-ray console in single shot mode. After setting the x-ray parameters and pressing the release button the x-ray pulse is generated at the push of the button at the control software. By the end of the x-ray pulse the detector is read out and the projection is displayed at the imaging screen and can be stored to hard disk.

**Fluoroscopic imaging.**  By fluoroscopic image acquisition, the movement of non-static objects can be observed or static objects can be imaged using a higher imaging dose. The limited dynamic range of the FPI also limits the achievable SNR of a single projection. A higher incident fluence can be used by adding up the signal of several frames. For this purpose either the continuous radiation mode is chosen at the x-ray console together with the internal trigger mode of the FPI[3], or the x-ray console runs in pulsed radiation mode and the FPI readout is triggered externally by the trigger board after each x-ray pulse. For moving objects the pulsed radiation mode is preferred because the same imaging dose can be delivered with shorter pulse lengths by increasing the anode current. This may avoid motion artifacts compared to the continuous radiation mode with an effective pulse length of the set FPI integration time. The projections are displayed at the imaging screen immediately and can be stored as an imaging sequence or as one averaged frame.

**Cone beam CT**.  For CBCT acquisition, the operator chooses the acquisition parameters (high voltage, anode current, pulse length, angle increment and rotation speed) at the control software, rotates the phantom to the start angle and releases the radiation. The x-ray console runs in hardware triggered mode and the FPI in external triggered mode. An acquisition sequence of enough numbers of projections is chosen at the imaging software. The angular speed $v_\Theta$ of the plate rotation is limited by the chosen angle increment $\Delta\Theta$ between two consecutive projections, the pulse length $t_p$ and the FPI's minimum integration time $t_f$ to $v_\Theta < \frac{\Delta\Theta}{t_p+t_f}$ and must be set appropriately to avoid a loss of projections. The phantom motion is synchronized to the imaging system by the control software. For this, the angular position of the phantom plate is monitored real-time by means of the encoder signals. After the start of the rotation an x-ray trigger signal is generated every $\Delta\Theta$ via a digital output of the PC card connected to the digital input line of the x-ray console. The sequence is finished, at the latest, after a full rotation but can already be stopped after an angle increment of $180° + \varepsilon + \Delta\Theta$ for a short scan. Therefore, the shortest acquisition

---

[3]Asynchronism artifacts due to FPI readout during radiation will not appear because every frame receives the same amount of radiation.

time for a CBCT at the x-ray wagon is $T_{min} = (t_p + t_f) \cdot \frac{180° + \varepsilon + \Delta\Theta}{\Delta\Theta}$. During image acquisition the current projection is always displayed at the imaging screen and the complete sequence is stored to hard disk after the end of the CBCT acquisition. The actual beam parameters of each pulse, which can be used to correct incident fluence variations, are also stored. Dark image acquisition for offset correction is performed prior to the actual CBCT acquisition by averaging various dark images with the corresponding integration time. For this purpose, either a pulsed sequence with pulse distances of $\Delta t = t_p + t_P = \frac{\Delta\Theta}{v_\Theta}$ with the pulse pause time $t_P$, or a 'simulated CBCT sequence' with the according parameters is applied. In both cases the detector runs in external triggered mode and the radiation is disabled by unplugging the SWR signal connection to the x-ray generator. Open field projections are acquired in the same way, but with the SWR signal connected to the generator and without any phantom on the phantom plate. The actual beam parameters of these projections are also stored to a corresponding text file.

A schematic overview of the main components and their interactions for CBCT acquisition is given in figure 4.5.
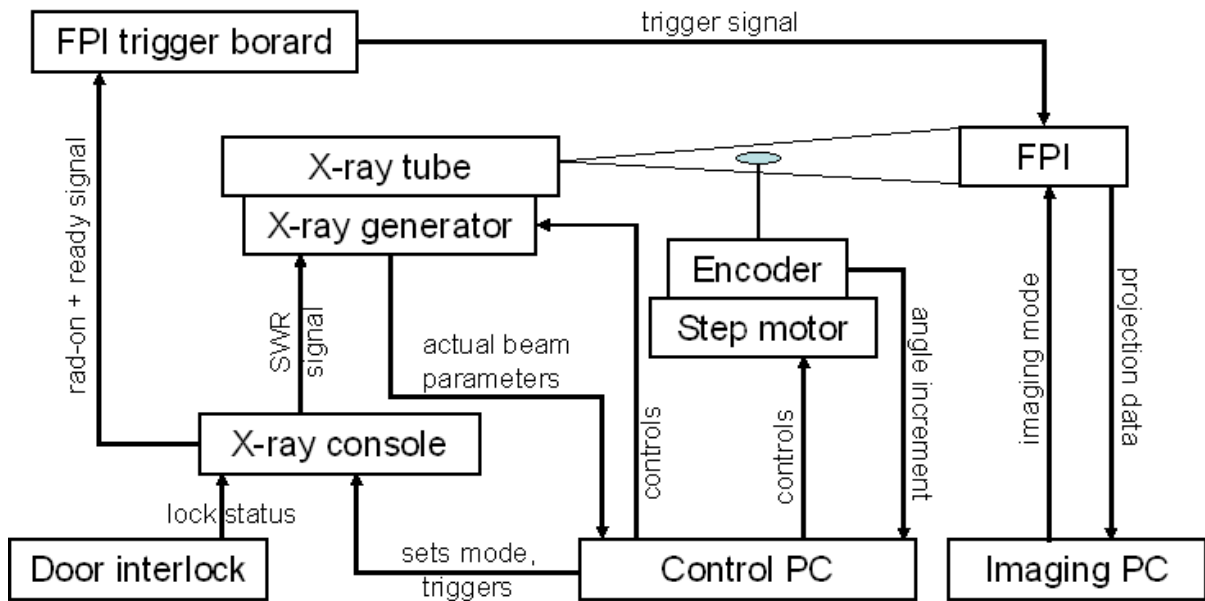


Figure 4.5: Scheme of components interaction at the x-ray wagon

*The interaction and the data flow between the different components of the x-ray wagon system are illustrated as described for CBCT acquisition. The arrows indicate the direction of the corresponding information flow. The phantom plate is represented by the blue ellipse, the x-ray beam by the triangle between the x-ray tube and the FPI. X-ray generator and x-ray tube are integrated to one component. Their internal interaction is not shown.*

## 4.3 Geometrical calibration

To back-project the FPI images for CBCT reconstruction (see section 2.5) the actual path of the x-rays must be known. With an ideal imaging geometry the ray path through the patient coordinate system for every FPI pixel is determined by its projection coordinates, the SID, the SDD and the corresponding projection angle. An ideal geometry assumes that **i)** the SID and SDD are constant and well known, **ii)** the x-ray source is punctiform, **iii)** the rotation axis and the central ray intersect perpendicularly in the origin of the patient coordinate system, **iv)** the central ray is perpendicular to the active area of the FPI and hits its center, **v)** the v-axis (see section 2.1.4) is parallel to the rotation axis, and **vi)** the exact projection angles are well known. Though all these requirements are nearly fulfilled for the x-ray wagon system where the only moving part is the phantom plate, a

real linac integrated kV-CBCT system is much more unstable and must not be assumed as ideal in the described sense. Provided that a reproducibility of the geometry is given for several successive CBCT acquisitions, a calibration for the real imaging geometry can be done by experimentally determining projection matrices for each projection angle [57], [58]. The projection matrix $\mathbf{A}_\Theta$ for the projection angle $\Theta$ is a $3 \times 4$ matrix that specifies, for every point $(x, y, z)$ in the patient coordinate system, to which point $(u, v)$ it is projected. It is

$$
\begin{pmatrix} \lambda u \\ \lambda v \\ \lambda \end{pmatrix} = \mathbf{A}_\Theta \begin{pmatrix} x \\ y \\ z \\ 1 \end{pmatrix}
\tag{4.7}
$$

where $\lambda$ is a normalization factor. With $\mathbf{A}_\Theta$ a back projection of $p_\Theta$ (see section 2.5) into the patient coordinate system is possible. This is described in detail in [57]. The explicit knowledge of $\Theta$ is not necessary. It is only important that $\mathbf{A}_\Theta$ is applied to a projection acquired at the same angle for which $\mathbf{A}_\Theta$ was determined. Therefore, the projection angles must also be reproducible. $\mathbf{A}_\Theta$ is determined with the help of a special calibration phantom shown in figure 4.6 [59]. This phantom is
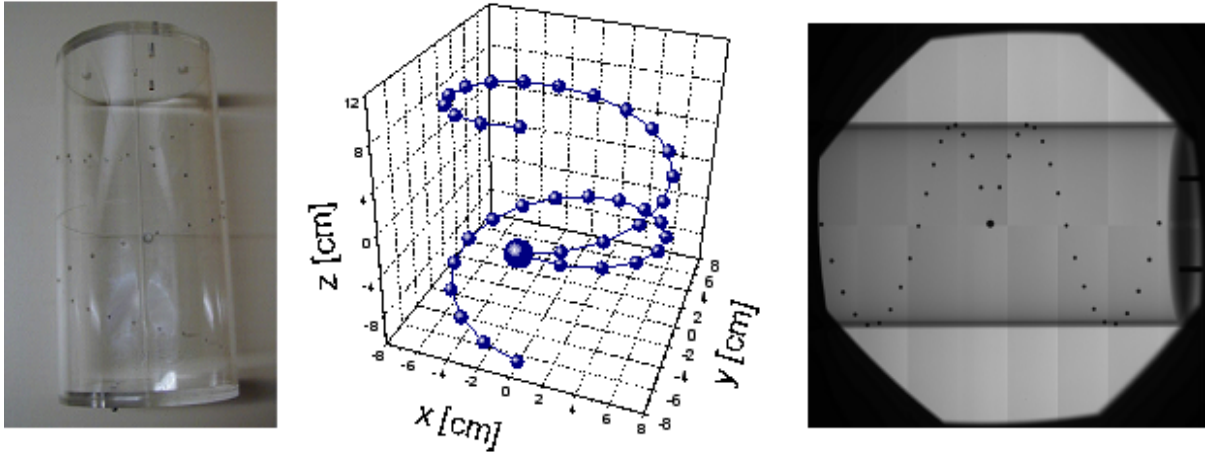


Figure 4.6: Calibration phantom

*A hollow perspex cylinder with metal bullets (left) is used for geometrical calibration. The center of the phantom defines the origin of the patient coordinate system. The graph illustrates the coordinates of the bullets. The right picture shows a projection of the calibration phantom.*

a hollow perspex cylinder containing 37 metal bullets embedded at defined positions along a helical trajectory in the cylinder wall. For identification purposes the middle bullet is characterized by a larger radius. For geometrical calibration the phantom is fixed on the phantom plate. The center of the phantom defines the origin of the patient coordinate system, its longitudinal axis being the z-axis and the big bullet at the coordinate $(x_B, y_B, z_B) = (0, -6.75\,\mathrm{cm}, 0)$. By acquiring a *calibration CBCT* of the phantom with the same start angle, $\Delta\Theta$ and $v_\Theta$ as for the real *imaging CBCT*, $\mathbf{A}_\Theta$ can be determined for each $\Theta$ by means of the bullet center coordinates on the respective projection and their known coordinates in the patient system. This method is also described in [57]. The bullet coordinates can be easily extracted on the high contrast projections using a threshold filter. Although the orientation of the phantom on the CBCT reconstruction depends on its position with respect to the position of the calibration phantom and may not be exactly adjustable on the x-ray wagon, the geometric calibration avoids deformation artifacts and implicitly delivers the correct phantom size.

An example of incorrect calibration is shown in figure 4.7. In this example a spherical contrast
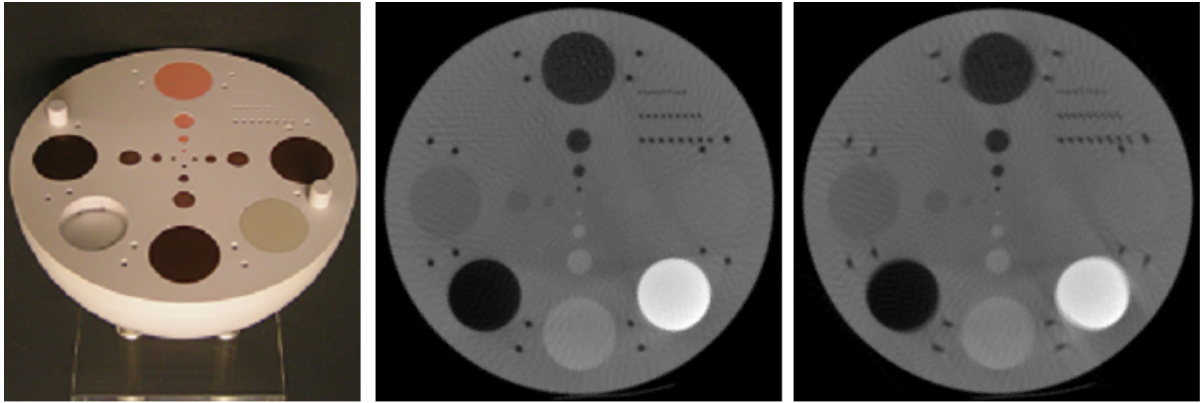
Figure 4.7: Artifacts caused by wrong calibration

*Left: lower half of the contrast phantom. The inlays of the middle slice are visible. The complete phantom if filled up with further RW3-plates to form a ball. Reconstructions of the central slice a shown with a correct geometrical calibration (middle) and assuming an ideal geometry but a 1 % error in the angular spacing.*

phantom was used. This phantom has a diameter of $16\,\mathrm{cm}$ and contains several RW3 slices of $10\,\mathrm{mm}$ thickness. The central slice has variably sized holes, and various circular disks of different materials are embedded. One hundred and eighty projections with angular spacings of $\Delta\Theta = 2°$ were acquired. This CBCT sequence was reconstructed once using the correct experimentally determined projection matrices (middle picture), and once with an artificial projection matrix assuming an ideal projection geometry but angular steps of $\Delta\Theta' = 1.98°$. At the x-ray wagon the SID and SDD are constant and well known. Therefore, the phantom size is correctly reconstructed, but the 1 % error in $\Delta\Theta$ leads to artifacts that are clearly visible, especially at the different inlays and the small rows of holes.

## 4.4 CBCT Reconstruction

For CBCT reconstruction, an in-house written software applying an FDK algorithm is used [57]. The algorithm is supplied with the projection matrices $\mathbf{A}_\Theta$ for every projection angle and with the gain and tube output corrected projection data $p_\Theta(u,v) = -\log[q(x,y)] \overset{(4.6)}{=} -\log\left(\frac{S_p(x,y)}{S_o(x,y)} \cdot \frac{I_o\, t_o}{I_p\, t_p}\right)$ With the assumptions of section 2.3 (monoenergetic beam, ideal detector, no scattered radiation) it is $p_\Theta(u,v) \overset{(2.15)}{=} \int \mu(x,y,z)\, ds$, the integral of the attenuation coefficients along the ray path $s$. Besides the gain correction, further pre-processing steps can be performed before the logarithm calculus of the x-ray image data. Sampling down the projection data to $1024\cdot 2^{-n} \times 1024\cdot 2^{-m}$ pixels yields a decreased memory requirement and calculation time. The compression of the projection data is performed by neighborhood averaging because summing up the signal of $2^{n+m}$ pixels decreases the projection noise by a factor of approximately $\sqrt{2^{n+m}}$. However, the maximum possible spatial resolution of the reconstruction is also decreased. A nearest neighbor sampling for example would only decrease spatial resolution without reducing the image noise. Practically, $n$ and $m$ are chosen between 0 and 2.

For reconstruction output, the number of voxels in x-, y- and z-direction $(n_x, n_y, n_z)$ of the patient coordinate system and the corresponding pitches $(p_x, p_y, p_z)$ must be chosen. This yields a CT cube of $n_x \times n_y \times n_z$ voxels with a voxel size of $p_x \times p_y \times p_z$ and a reconstruction volume of $V = n_x p_x \times n_y p_y \times n_z p_z$. Throughout this work it is $p_x = p_y$ and $n_x = n_y$ unless otherwise noted. It is unnecessary to define a reconstruction volume that exceeds the maximum FOV (here, approximately $27\,\mathrm{cm}$) in one dimension. The reconstruction algorithm calculates the attenuation co-

efficients at each voxel center and allocates this value to the complete voxel volume. ($p_x$, $p_y$ and $p_z$) define the maximum spatial resolution of the reconstruction. Each voxel corresponds to only one single pixel of each projection determined by the projection matrices $\mathbf{A}_\Theta$. Therefore, the down sampling of the image data should follow the voxel pitch of the reconstruction. The effective pixel pitch (here, $p_u = 2^n \times 0.4\,\text{mm}$ and $p_v = 2^m \times 0.4\,\text{mm}$) of the projection data may be chosen as $p_u \approx \frac{\text{SDD}}{\text{SID}} \cdot p_x$ (and correspondingly: $p_v \approx \frac{\text{SDD}}{\text{SID}} \cdot p_z$). Overly small pixel pitches may lead to unused projection data that might have been used for noise reduction by a further down sampling. Too much down sampling may lead to a blurring in the reconstruction data.

## 4.5  First tests

With the above described components and methods, a prototype system for first 2D and 3D imaging experiments was competed. This section reports on first measurements applied with this configuration before the next step in the development course, the integration of the imaging components at the treatment machine, was performed.

### 4.5.1  Linearity

For a quantitative analysis of the x-ray projections, including the CT reconstruction of attenuation coefficients, the linearity of the imaging system is an important factor. This means, whether a proportionality is observed between the output of the x-ray tube and the corresponding FPI response. This correlation was measured separately for an $U_1 = 80\,\text{kV}$ and an $U_2 = 120\,\text{kV}$ output spectrum of the x-ray tube. Measurements were performed using the pulsed radiation mode of the x-ray console and the external trigger mode of the detector. No phantom was placed on the phantom plate. For each spectrum, 10 sequences with different settings for anode current $I$ and pulse length $t$ were acquired. The parameters were adjusted to nominally deliver outputs of $I \cdot t = 300\,\mu\text{As}$ to $I \cdot t = 3000\,\mu\text{As}$ in steps of $300\,\mu\text{As}$ for $U_1$ and $I \cdot t = 100\,\mu\text{As}$ to $I \cdot t = 1000\,\mu\text{As}$ in steps of $100\,\mu\text{As}$ for $U_2$. For each sequence, 35 pulses were acquired using the same parameters. For evaluation purposes, the nominal parameters for $I$ and $t$ were not used but rather those supplied by the generator as the actual pulse parameter feedback, which are automatically stored to a text file after each pulse. Additionally, an ionization chamber[4] was placed between the x-ray tube and the detector, and the charge that was produced in the chamber during each sequence was measured. These measurements were performed for a linearity analysis of the FPI, independent from the generator feedback. The x-ray shadow of the chamber on the FPI is small compared to the beam size and does not affect the measurement, since linearity is also demanded for the FPI pixels in the chamber shadow. Figure 4.8 shows as an example one projection of the series. The linearity of the
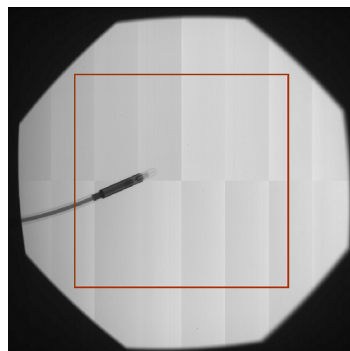


*The ionization chamber is visible on the open field projection. The gray values of the 624 × 624 pixels inside the red sized square are used for linearity evaluation.*

Figure 4.8: Projection for linearity analysis

---

[4]Throughout this work, for all measurements an ionization chamber from PTW Freiburg (type *M31002*) is applied.

gray values $g_{x,y}$ for each pixel inside the ROI bordered by the red square in figure 4.8, and their mean gray value $g_{\mathrm{roi}}$, were analyzed. In figure 4.9 the linearity of the FPI, the relative deviation from a linear fit to the data, and a distribution of standard deviations from the linearity for each pixel inside the ROI is plotted.
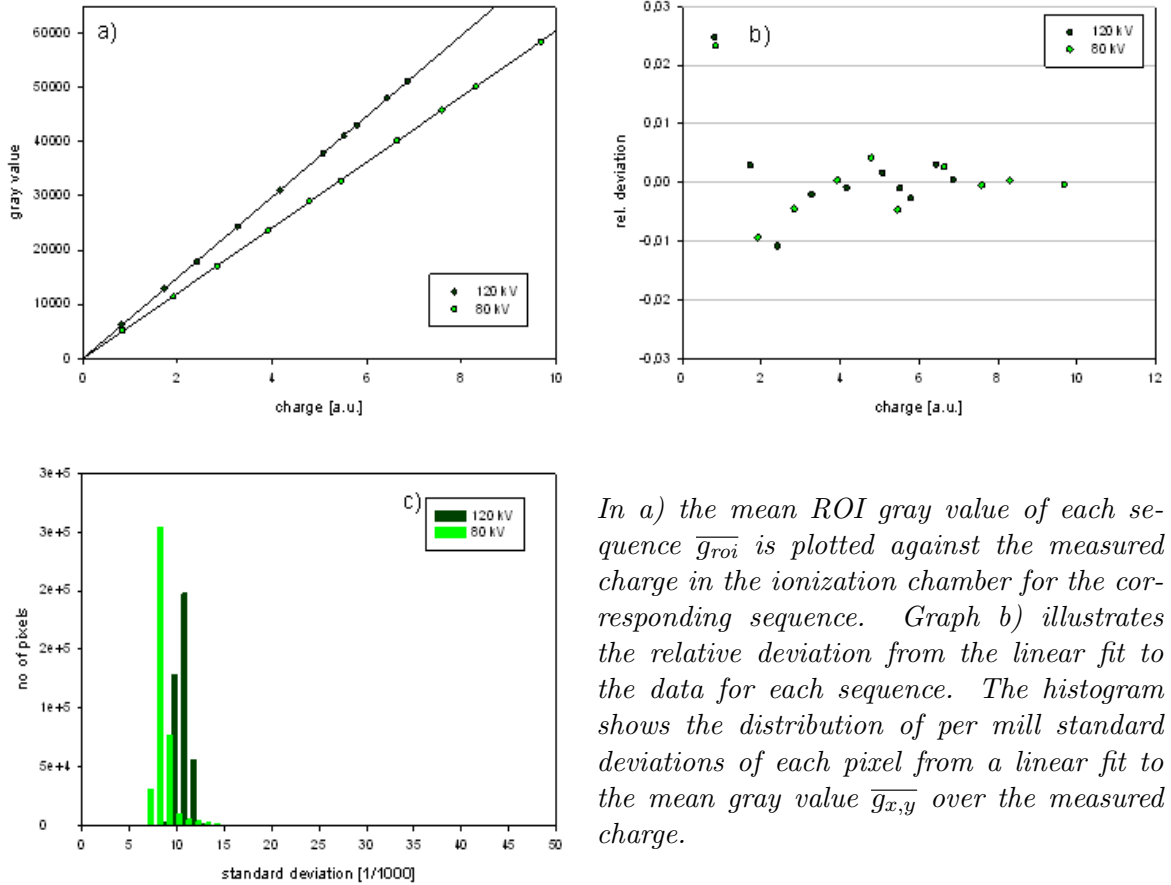


*In a) the mean ROI gray value of each sequence $\overline{g_{roi}}$ is plotted against the measured charge in the ionization chamber for the corresponding sequence. Graph b) illustrates the relative deviation from the linear fit to the data for each sequence. The histogram shows the distribution of per mill standard deviations of each pixel from a linear fit to the mean gray value $\overline{g_{x,y}}$ over the measured charge.*

Figure 4.9: Linearity of the FPI

The plots show a good linearity of the FPI. Deviations of the ROI gray values from the linear fit are mostly below 1%. The only outlier for both energies[5] is the first data point representing the lowest chamber- and FPI signal. This might be caused by a comparatively high noise ratio of both measurements and high relative gray value uncertainties caused by inaccuracies of the offset correction. The standard deviation histogram also outlines a good pixel-wise linearity with slightly better values for the 80 kV spectrum. To analyze the linearity of the imaging system, including possible uncertainties from the generator feedback, the gray values are also analyzed as a function of the mean tube output $\overline{I \cdot t}$ of each sequence. This is shown in figure 4.10.

As expected, the results show a slightly decreased linearity that might be caused by inaccuracies of the generator's tube output feedback. To analyze this feedback, the chamber charge was measured at both energies for several sequences of 20 pulses each with a fixed pulse width setting of 100 ms, and anode current settings between 20 mA and 100 mA for $U_1$, and between 20 mA and 70 mA for $U_2$. In figure 4.11 a normalized quotient of measured charge and indicated tube output is plotted against the cumulated tube output of the corresponding sequence.

---

[5]Here and in the following the term 'energy' might be used synonymously for 'tube voltage' or 'x-ray spectrum'.
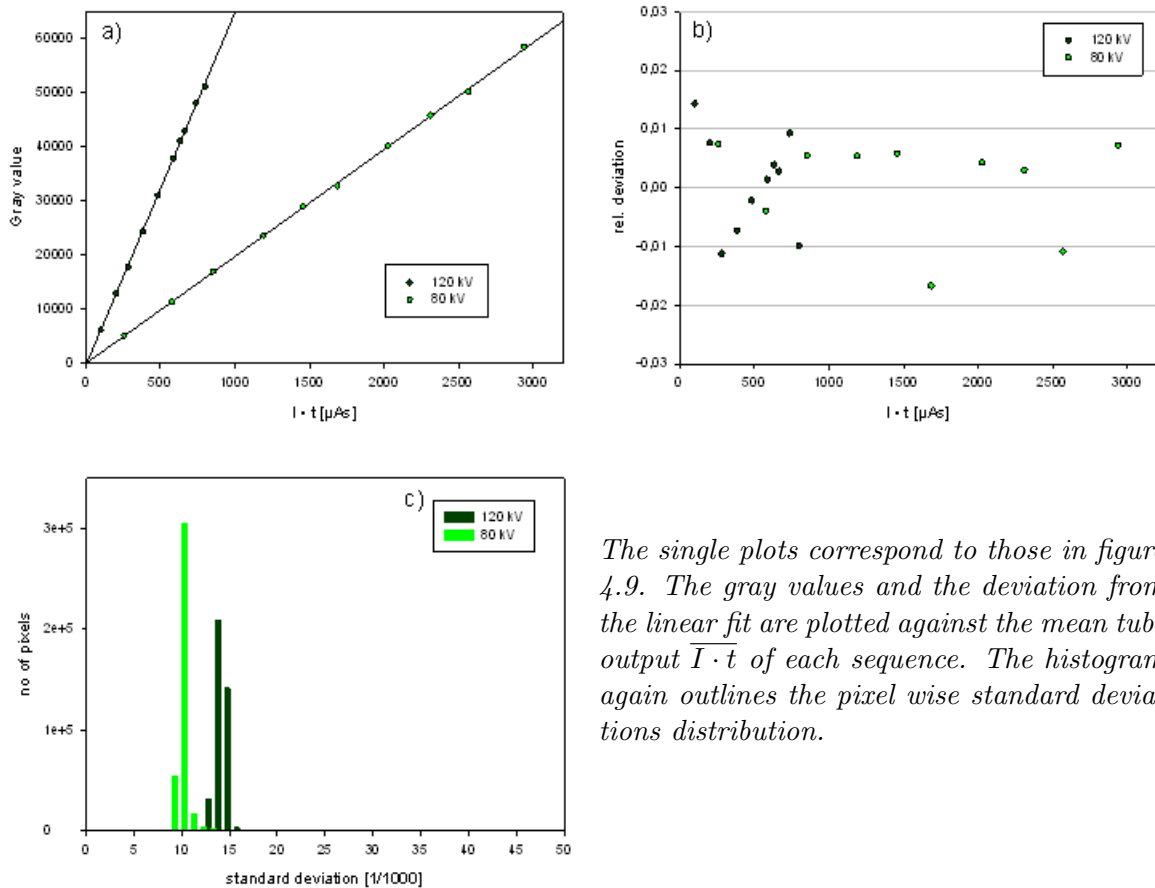
*The single plots correspond to those in figure 4.9. The gray values and the deviation from the linear fit are plotted against the mean tube output $\overline{I \cdot t}$ of each sequence. The histogram again outlines the pixel wise standard deviations distribution.*

Figure 4.10: Linearity of the imaging system
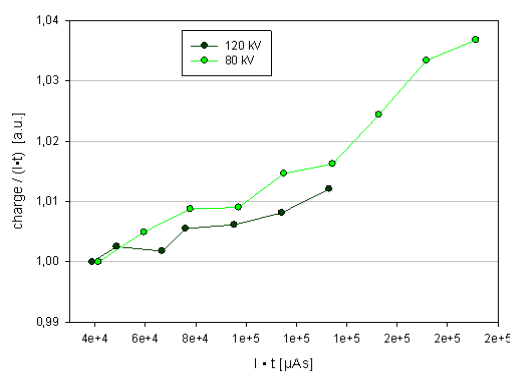


*The normalized quotient of charge caused by a certain indicated tube output is plotted against the output. For the 120 kV plot only a smaller data range could be analyzed due to tube load limitations.*

Figure 4.11: Generator feedback linearity

The graph shows that either higher current settings lead to underestimation or lower current settings lead to overestimation of the actual tube output. This trend seems to be slightly stronger for lower energies. Throughout this work mainly 120 kV spectra are used. The generator feedback is not further corrected for the low dependency of the settings since the linearity of the imaging system shown in figure 4.10 is assumed to be appropriate for further measurements.

### 4.5.2  Modular transfer function

The *modular transfer function (MTF)* of an imaging system is the magnitude of the optical transfer function (OTF), which describes the spatial (angular) variation as a function of spatial (angular) frequency. Since in imaging systems, the phase component is typically not captured by the sensor, the MTF is the important measure. The MTF describes the response of an imaging system to an image decomposed into its Fourier-components. The concept and the principal of MTF measurements is illustrated in figure 4.12. MTF measurements can be performed by acquiring an x-ray
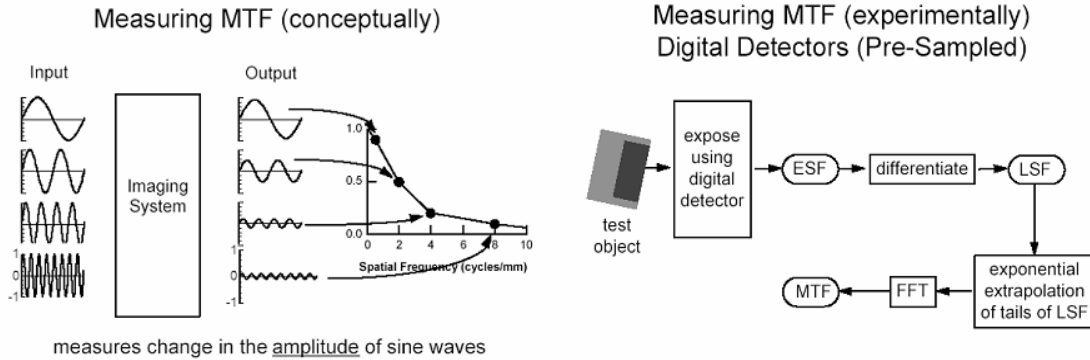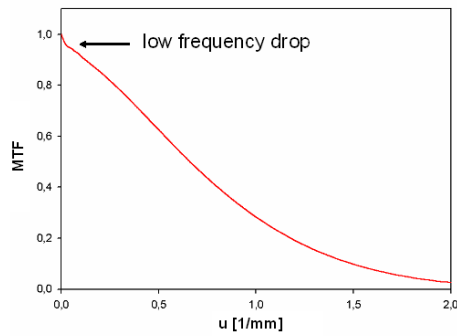


Figure 4.12: MTF measurement

*The MTF of an imaging system describes the input/output amplitude ratio of sine waves as a function of spatial frequency. The MTF can be determined by means of an over sampled ESF measurement (see text). Pictures source: [61].*

projection of a rectangular opaque test object with straight edges that is fixed at the front plane of the detector, slightly tilted with respect to the columns (or rows). After dark- and open field correction, the *edge spread function (ESF)* is determined by taking a profile perpendicular to the edge of the test object. The small tilt of the edge allows an *over-sampling* of the ESF. This means, that the profile can be sampled much finer than the pixel pitch of the FPI would allow it, for an edge that is parallel to the columns. Practically, to reduce noise, instead of one single projection, an averaged image of many projection is used, and the ESF is also averaged over many profiles along the edge. The MTF is determined by means of ESF(x), where x denotes the (positive or negative) distance from the edge, by performing the following steps [61], [62]:

1. *Differentiation* $\frac{d}{dx}$ ESF(x) = LSF(x) (line spread function)

2. *Exponential extrapolation* of the tails of LSF(x)

3. *Fourier transform* $\int_{\infty}^{-\infty}$ LSF(x) exp$(-2\pi iux)\,dx =$ MTF(u), u: spatial frequency.

The MTF of a 2D projection acquisition with the x-ray wagon imaging system was determined as described using a $10 \times 10 \times 0.5\,\text{cm}^3$ tungsten slab as a test object. Fifty well-illuminated projections were averaged and the signal from 100 detector rows was used to get the final over-sampled ESF. The resultant MTF after the described calculation steps (differentiating, extrapolating, FFT) is shown in figure 4.13. It shows a steep drop at low frequencies and then extends down to a frequency of $2\,\text{mm}^{-1}$. The *low frequency drop* may be caused by scattered radiation, which would add a broadly Gaussian distributed offset to the signal thus increasing the low frequency component in the MTF [60].

The MTF shows how contrasts of different sized object details are reflected by intensity contrasts in the image. Relevant details for medical applications are in a range between 0 and $2\,mm^{-1}$. A

*The MTF measured for 2D projections of the x-ray wagon system. The MTF extends to frequencies of about $2\,mm^{-1}$. The low frequency drop may be caused by an offset in the signal.*

Figure 4.13: MTF

special value of the MTF is the limiting resolution, i. e. the spatial frequency at $4\,\%$ of the maximum amplitude [63]. Figure 4.13 shows a limiting resolution of approximately $2\,mm^{-1}$ for the analyzed FPI, which indicates an appropriateness for the intended applications.

### 4.5.3   Dose measurement

To obtain an estimate of the imaging dose, dose measurements were performed using a cylindrical water-filled perspex phantom. The phantom has a diameter of 18 cm and a height of approximately 20 cm. Two thin cylindrical holes, one along the central axis and one close to the outside margin of the phantom, allow an insertion of a ionization chamber. The phantom was placed on the phantom plate with it longitudinal axis in the y-direction (along the rotation axis of the plate). The setup is illustrated in figure 4.14. Imaging dose was measured separately with the chamber inserted into the
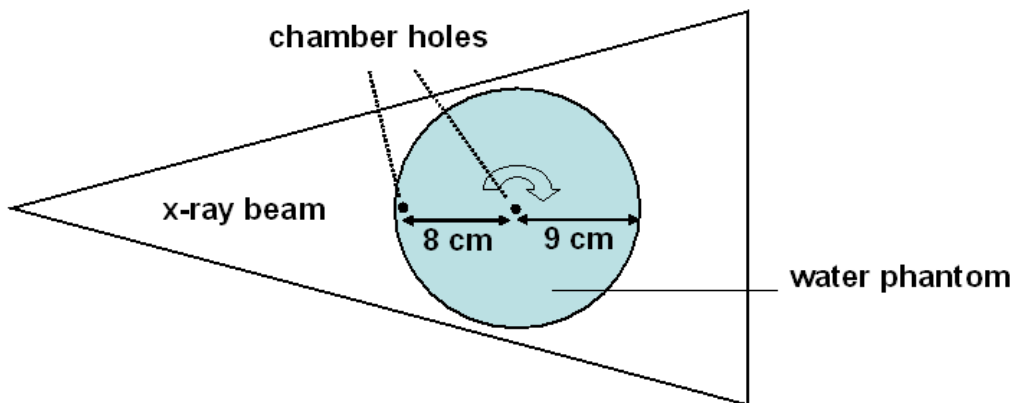


Figure 4.14: Dose measurement setup

*To view of the setup. The water phantom is placed on the rotating phantom plate. A ionization chamber is inserted in the central and the peripheral hole, respectively. X-ray pulses are applied at every degree of the phantom rotation.*

central and the peripheral hole. The same chamber was used as for the linearity analysis (see section 4.5.1). It was inserted into the holes as far as was necessary to be hit by the central ray of the beam. Dose values were measured again for both energies: $U_1 = 80\,\mathrm{kV}$ and $U_2 = 120\,\mathrm{kV}$. Measurements were performed by acquiring a CBCT sequence of the phantom over the whole angular range of $360°$, applying one pulse per degree ($\Delta\Theta = 1°$). Typical x-ray parameters for CBCT acquisition were used, providing a good but not saturated illumination of the FPI (see figure 4.10a). The parameters are: $U_1:\ I_1 = 50\,\mathrm{mA}$, $t_1 = 15\,\mathrm{ms}$ and $U_2:\ I_1 = 100\,\mathrm{mA}$, $t = 20\,\mathrm{ms}$. For evaluation the

feedback parameters stored in the corresponding text file were used. Dose calibration values were calculated on the basis of the applied cumulative tube output for a 360° CBCT acquisition. The values for the central axis are also valid for arbitrary 2D projections. Table 4.1 summarizes the results.

Table 4.1: Imaging doses for CBCT acquisition

|  | dose calibration factors | |
|---|---|---|
|  | peripheral [mGy/As] | central [mGy/As] |
| $80\,\mathrm{kV}$ | **22** | **16** |
| $120\,\mathrm{kV}$ | **70** | **52** |

*Dose per cumulative tube output of a* 360° *CBCT acquisition of the described water phantom.*

In the following, these values are used as an imaging dose estimation reference for this x-ray tube and similarly sized phantoms.

### 4.5.4 Cone beam CTs

As a proof of principle for 3D imaging using the described components and methods, CBCTs of several phantoms were first acquired at the x-ray wagon. A full scan of the contrast phantom, that was already shortly introduced in section 4.3, was acquired with the following nominal parameters: $U = 120\,\mathrm{kV}, I = 50\,\mathrm{mA}, t = 15\,\mathrm{ms}, \Delta\Theta = 2°$. The isocentric dose[6] $D_c$ was estimated to be $D_c \approx 6\,\mathrm{mGy}$ according to table 4.1.[7] The CBCT sequence was reconstructed once using all 180 projections, and once as a short scan over an angular range of only 200° yielding an effective imaging dose of $D_c \approx 3.5\,\mathrm{mGy}$. As a second example an Alderson head phantom was scanned, again over the full angular range. The parameters were: $U = 120\,\mathrm{kV}, I = 55\,\mathrm{mA}, t = 20\,\mathrm{ms}, \Delta\Theta = 1°$. The applied dose was estimated to be $D_c \approx 18\,\mathrm{mGy}$. This phantom was also reconstructed first using all projections, and then with only the first 200 projections. The short scan reconstruction results in an effective imaging dose of $D_c \approx 10\,\mathrm{mGy}$. All projections were sampled down to $512 \times 512$ matrices. CT cubes of $(25.6\,\mathrm{cm})^3$ were reconstructed at a resolution of $512 \times 512 \times 128$ voxels. Transversal slices[8] of these reconstructions are shown in figure 4.15. These first promising results can be regarded as a proof of principle. Several components were integrated to provide a working and stable kV x-ray imaging system. Different methods were described to apply 2D and 3D imaging with this setup. Acceptable CBCT reconstructions obtained for several phantoms and different imaging methods (short scan, full scan, different $\Delta\Theta$). Therefore, the next step of the development course could be started: the integration of the imaging components at the treatment machine.

---

[6]'isocentric dose' is used synonymously for the dose at the central axis of the phantom and the dose at the phantom center, respectively.

[7]The actual isocentric dose might be slightly higher due to the lower diameter compared to the reference phantom.

[8]transversal slices are perpendicular to the z-axis of the patient coordinate system.
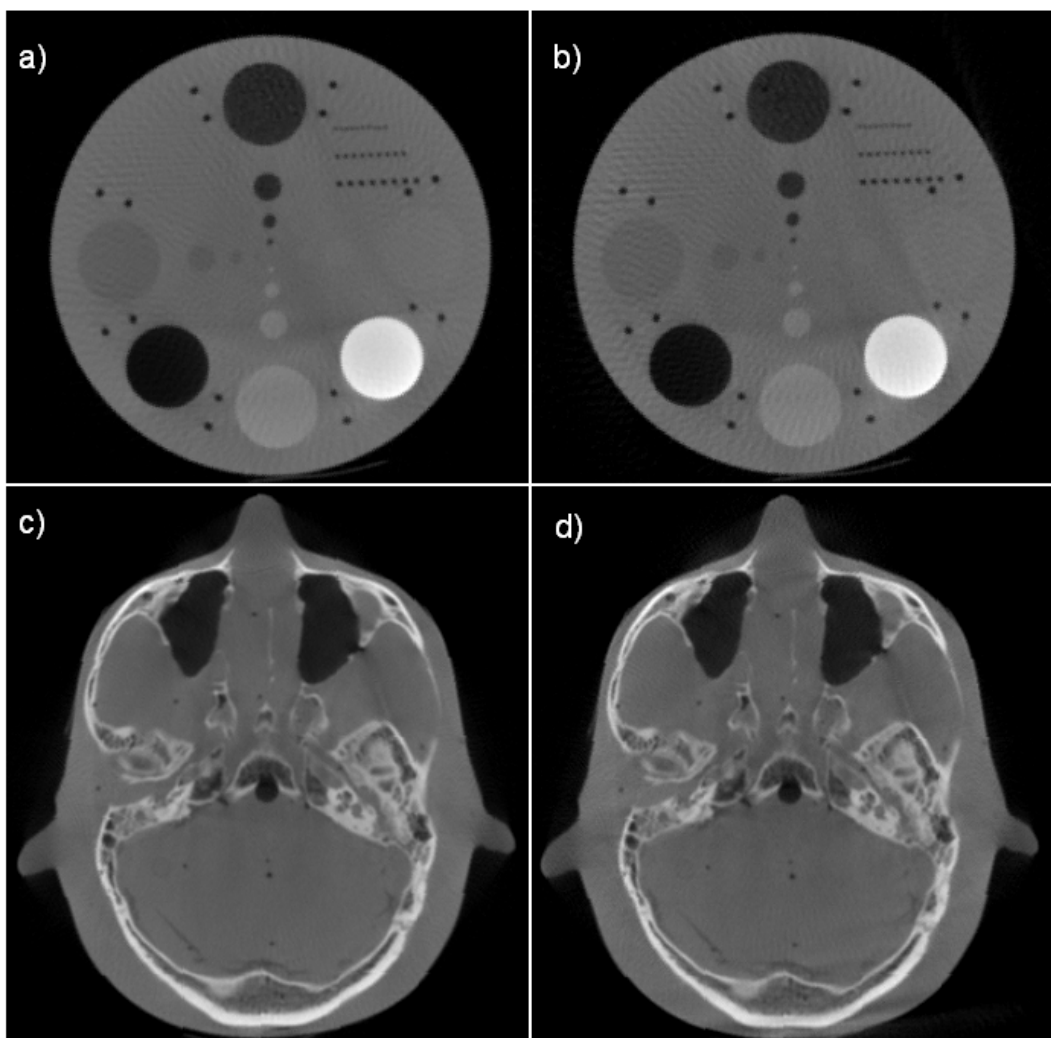
Figure 4.15: First CBCT reconstructions from the x-ray wagon

*The left side shows the full scan, the right side the short scan reconstruction of the contrast phantom and the Alderson head, respectively. The streak artifact in a) and b) are caused by the low angular resolution ($\Delta\Theta = 2°$) of the CBCT acquisition. Lower effective imaging doses cause a higher noise ration in the reconstruction, visible in b) and d). Nevertheless, the contrasts are well resolved in a) and b) and even the smallest holes having a diameter of $1\,mm$ and a spacing of $2\,mm$ are still distinguishable.*

# Chapter 5

# Integration of the kV-imaging system at the linear accelerator

With the transfer of the imaging component from the x-ray wagon to the treatment machine (linac) the principle of kV-image acquisition does not change. The main difference is the drive mechanism that is now replaced by the gantry. For 3D image acquisition the phantom is no longer rotated, but the imaging system rotates around the phantom. Therefore, the step motor and its related components are no longer needed and the image acquisition process must be synchronized with the gantry rotation. Furthermore, the much higher moments of inertia and the asymmetrical design of the gantry may lead to an imbalance of the rotation. This, and the influence of gravity that comes along with the rotation around a horizontal axis, which results in geometrical uncertainties like a variable sag of the components for different gantry angles, places particular importance on the geometrical calibration. Furthermore, the transformation of patient coordinates into room coordinates becomes important when using CBCTs for patient positioning purposes. To obtain a well-defined transformation according to equation 2.1 with $(x_r, y_r, z_r) = (0, 0, 0)$ the calibration phantom must be exactly aligned with the *room lasers* marking the three cartesian axes of the room coordinate system.

MV-imaging applications, that were not possible with the x-ray wagon bench top setup are provided by the linac-integrated system. In the following sections the setup is described in more detail.

## 5.1   Hardware setup

The x-ray tube and the FPI were mounted at the linac following the Inline concept. For this purpose, specially produced metal holders were used. The tube holder is screwed at the structure in a way that the central ray path coincides with the rotation axis of the MLC. The FPI holder provides the possibility to shift the FPI in 2 cm steps, up to 18 cm, out of its centered position for FOV extension, and is inserted into the accessory tray of the linac right below the MLC and fixed with screws. As the tube is installed to be stationary, the FPI can be easily removed at any time. The orientation of the FPI coordinate system with respect to the projection system depends on the MLC angle. The x-ray generator is placed inside the treatment room. The cables connecting the tube and the generator, as well as the FPI cables, are passed through the linac in a way as to not disturb any kind of linac or imaging operation. A *Siemens Primus* linac provided for research purposes was used for the kV-system integration. The geometric parameters are SID $\approx 100$ cm and SDD $\approx 142$ cm, and may vary slightly due to gravitational sag and uncertainties of the tube mounting position. Figure 5.1 shows the kV-imaging setup installed at the linac.
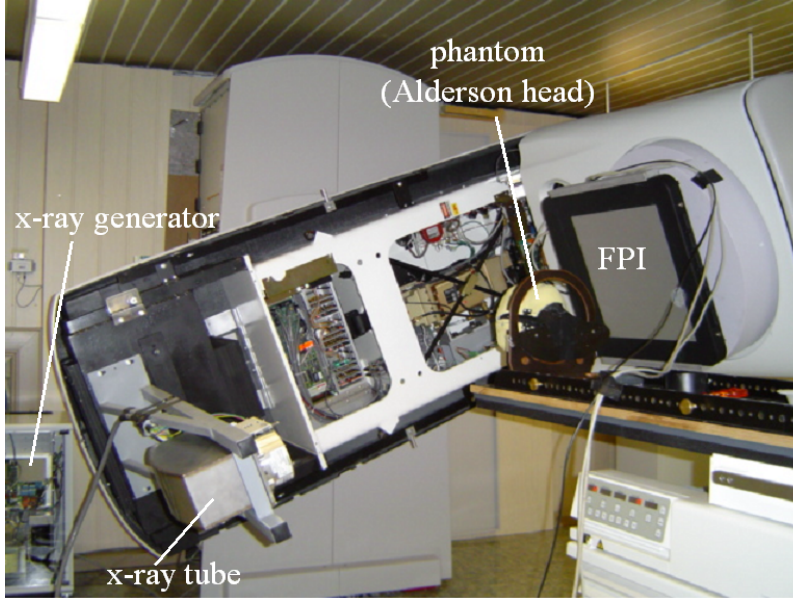
*The imaging components (x-ray tube and FPI) are installed at the linac following the Inline concept. The tube is installed with the anode-cathode direction parallel to the y-axis of the room co-ordinate system ($y_{cathode} > y_{anode}$). Here the MLC is at $90°$, and therefore the x-axis of the FPI is antiparallel to the room y-axis (cable plugs towards structure).*

Figure 5.1: Linac with kV-imaging components

## 5.2 KV-imaging

The process of 2D kV-imaging regarding the operation of the imaging components does not differ from the x-ray wagon. Due to the reduced SDD, pixel gray values increase by a factor of $\frac{(150\,\text{cm})^2}{(142\,\text{cm})^2}$, which must be taken into account concerning detector saturation. The field size on the detector plane reduces accordingly, and allows a wider beam collimation resulting in a slightly increased FOV. The projection angle $\Theta = (\gamma_g + 180)\,\text{MOD}\,360$ ($\gamma_g$: gantry angle) coincides with the tube angle and must, therefore, be adjusted via the linac console or the gantry hand control in possible steps of $0.1°$.

For CBCT acquisition, the gantry rotation must be synchronized with the x-ray control system. For this purpose the PROMs of several linac function controllers were replaced to run the machine with a research firmware, providing a special rotational treatment mode that is intended for MV-CT acquisition [64]. Usually, during a rotational treatment, the linac delivers at a constant dose rate while rotating with a constant speed over a predefined angular range. The operator sets the gantry start angle $\gamma_{\text{start}}$, the rotational direction, the angular range $\Delta\gamma$ and the total dose $D$. The angular gantry speed is $v = \Delta\gamma \cdot \frac{\dot{D}}{D}$. The dose rate $\dot{D}$ is automatically adjusted to

$$\dot{D} = \begin{cases} \dot{D}_{\text{max}} = 250\,\frac{\text{MU}}{\text{min}} & \text{, for } \frac{D}{\Delta\gamma} \geqslant \frac{\dot{D}_{\text{max}}}{v_{\text{max}}} \\ v_{\text{max}} \cdot \frac{D}{\Delta\gamma} & \text{, else} \end{cases}$$

with $v_{\text{max}} = 300°\,\text{min}^{-1}$. Using the research firmware, a constant dose rate is not employed but rather single beam pulses with a user defined length (in the magnitude of milliseconds) and angular spacing. Nevertheless, the gantry speed is the same as it would be for the common rotational treatment.

This mode is also used for kV-CBCT acquisition. To deactivate the MV-beam the electron injector is switched off. The linac must be operated in *service mode* because the *dose interlocks* must be disabled in order to avoid a sequence abort due to the dose delivery monitoring. For kV-pulse and detector triggering two digital outputs of the linac are used: The *RO output* and the *HV output*. The high TTL state of the RO output coincides with the beam-on phases (or rather with the intended beam-on phases when operating with a deactivated injector). The HV output provides a

high TTL signal during the complete rotational sequence. This output is connected to the ready input of the detector readout trigger board for initial FPI readout, and is used instead of the ready output of the x-ray console because the signal is directly correlated with the actual start of the CBCT sequence, always rising approximately two seconds before the first kV-pulse. The x-ray console ready signal is operation dependent and may start much earlier (as soon as the user starts the anode rotation). The RO output is connected to the hardware trigger input of the x-ray console. Therefore, the kV-pulses are no longer triggered by a software generated trigger signal, but by the rising edge of the RO-signal. The length of this signal has no influence on the kV-CBCT acquisition.

To acquire a kV-CBCT the operator has to perform the following steps:

1. Disable MV beam and dose interlocks.

2. Program rotational treatment (inclusive pulse length and angular spacing) at linac console.

3. Set x-ray parameters (x-ray console runs in hardware triggered mode).

4. Prepare imaging software (FPI runs in external triggered mode).

5. Start anode, release radiation.

6. Start sequence at linac console.

According to figure 4.5 a schematic overview of the main components and their interactions for CBCT acquisition is shown in figure 5.2.
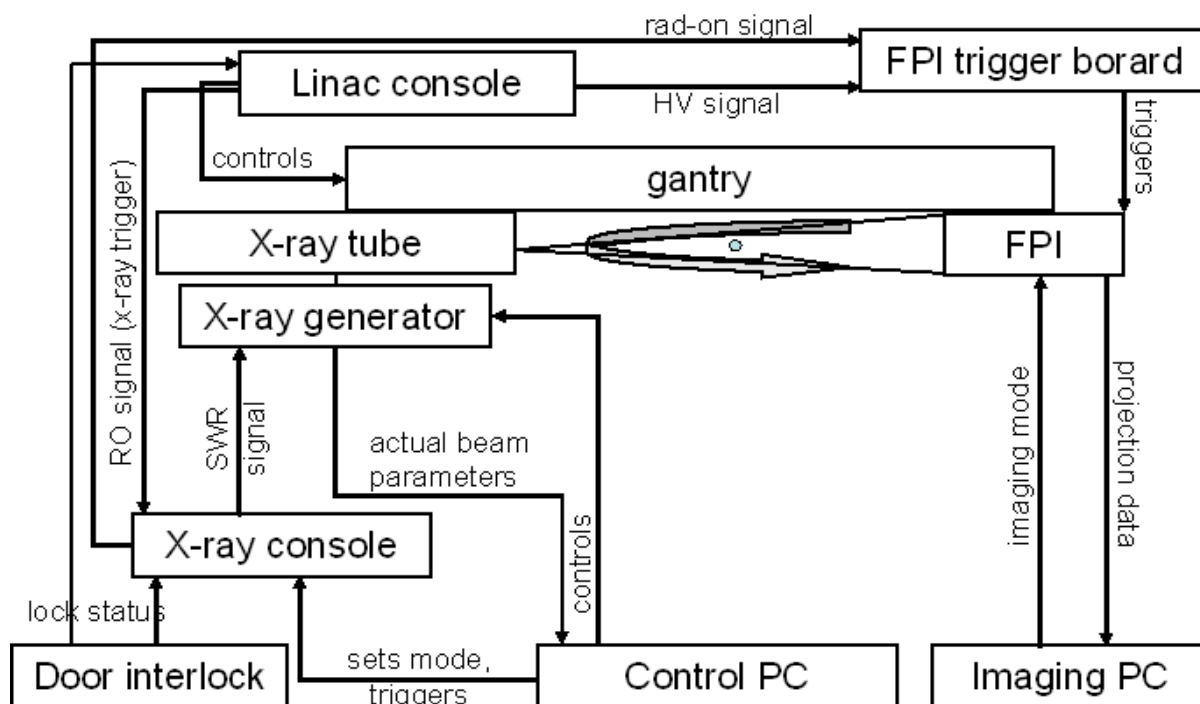


Figure 5.2: Interaction of components for linac integrated kV-CBCT imaging

*The interaction and the data flow between the different components for linac integrated kV-CBCT acquisition is illustrated. The arrows indicate the direction of the corresponding information flow.*

Figure 5.3 illustrates the chronology of signals and x-ray pulses during a linac integrated kV-CBCT sequence.
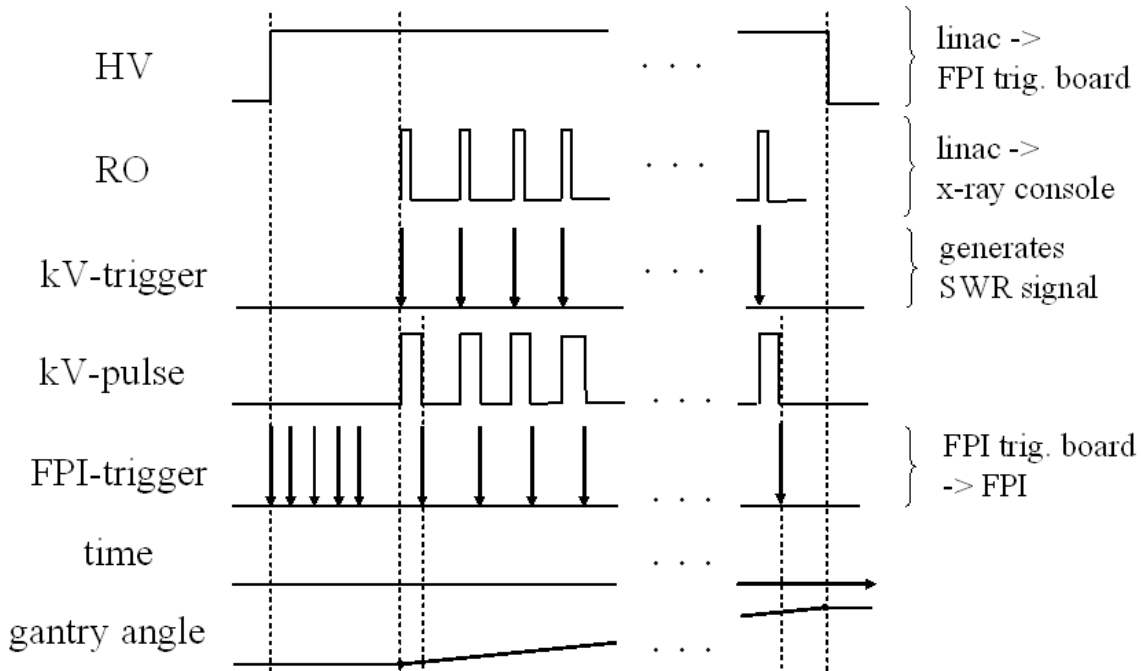


Figure 5.3: Chronological sequence of signals and pulses during a CBCT acquisition

*With the start of the sequence the HV-signal rises and triggers the FPI for an initial readout. Approximately two seconds later, the gantry rotation starts and the first RO pulse appears and triggers the first kV-pulse. The falling edge of the kV-pulse triggers the FPI readout. The following RO-signals are generated for constant gantry angle intervals. At the end of the sequence, the gantry stops and the HV-signal falls. The time axis is not necessarily linear. The vertical dashed lines are for orientation purposes and indicate certain points in time.*

## 5.3   MV-beam monitoring

MV-beam monitoring with the FPI has a couple of difficulties: It is not immediately possible to synchronize the MV beam and the FPI readout. This is because the MV beam does not provide a short-term uniformity in dose rates, but rather consists of multiple dose pulses with pulse lengths of a few microseconds. The distance between the pulses determines the nominal (long term) dose rate and is of the magnitude of milliseconds[1]. For a normal treatment, the dose pulse distance is much shorter and the beam-on time of one treatment segment is much longer than the readout time of the FPI. Due to the high intensity of the treatment beam and the close distance of the FPI to the MV source (here approximately 58 cm), the FPI must be operated in its free running mode with its shortest available integration time to avoid detector saturation. The asynchronism of the dose pulses and the FPI readout leads to moving intensity stripe patterns on the MV-beam projections. The brighter areas received one dose pulse more since their last readout than the darker ones. Summing up all frames that contain signal from dose pulses of one beam eliminates the stripe pattern and reflects the cumulative intensity of the beam.

The used FPI would get saturated by irradiating it in the designated position with the common dose rate of $\dot{D} = 250 \frac{\mathrm{MU}}{\mathrm{min}}$ even in free running mode. To allow MV-imaging the dose pulse distance must be decreased by at least a factor of approximately 25. The resulting dose rate is no longer

---

[1]The term 'dose pulse' is used for one single microsecond pulse, contrary to a 'beam pulse' containing several dose pulses.

suitable for treatment due to time constraints, but can be applied for testing purposes. The MV beam is designed to produce homogeneous dose profiles in a water depth of 10 cm. The intensity profile is not homogenous at the FPI plane. To correct the projections for the gain structure of the FPI, and obtain quantitative information about the beam intensity, a calibration can be performed by film measurements of the intensity profile. If only the beam shape itself is of interest, an open MV-field correction of the projections is sufficient. The correction image can be acquired by averaging multiple projections (e. g. 100) obtained in free running mode during a beam-on phase of the maximum open MV-field[2].

## 5.4 Special features I - kV-imaging during therapy

The Inline concept uses the same detector for kV- and MV imaging. To obtain a pure kV-projection during beam delivery, an interruption of the MV beam during the kV-acquisition process is necessary. The linac provides a *gated treatment mode* that allows such a short-term interruption of the treatment beam by means of a digital TTL signal connected to its *gate input*. A high signal at the input disables the beam, while a low signal releases the beam delivery. Therefore, pure kV-acquisition can be performed by the following workflow (linac running in gated mode, x-ray console in hardware triggered mode and FPI in external triggered mode):

1. Interrupt MV-beam (high signal at gate input)

2. Trigger FPI readout (clear current frame)

3. Wait for the FPI to finish the readout

4. Generate kV x-ray pulse

5. Trigger FPI readout

6. Wait for the FPI to finish the readout

7. Release MV beam (low signal at gate input)

Additional hardware, along with associated control software, was developed for the (2D) kV-imaging during treatment. The *KICK Box* provides the following imaging modes:

**Fluoroscopy mode** In this mode kV-projections of the patient are acquired in user defined intervals during the beam-on phases of the treatment.

**Positioning mode** In this mode a kV-projection of the patient is acquired before each treatment field (i. e. after a new gantry angle has been adjusted for treatment). Afterwards, the MV-beam is blocked until the operator releases it by a mouse click (or, optionally, it is released by the software after an automatic position verification process).

**Single shot mode** This mode allows the user to acquire one single kV-projection at any time during the treatment.

---

[2]The maximum field opening of the MV beam is $40 \times 40 \, \text{cm}^2$ at the isocenter plane according to approx. $23.2 \times 23.2 \, \text{cm}^2$ at the FPI plane.

Additionally the following features are provided:

- SW controlled switching between the single modes at any time.

- SW controlled MV- and kV-beam gating at any time.

- SW switchable permanent FPI readout during MV beam-on phases (for MV beam imaging purposes and to avoid FPI saturation)

  - triggered in predefined time intervals
  - or by means of FPI *frame readout finish* feedback

- SW switchable MV-field overlap on kV-images (applies a short MV beam of predefined length during kV-pulse acquisition).

- Frame type feedback to control-SW (indicates whether the current FPI frame contains kV- or MV image information).

All modes require the gated mode of the linac. The hardware is connected to a USB controlled PC card providing several digital and analog inputs and outputs. The PC card is integrated together with the KICK box in one cover supplied with a cable that can directly be plugged into the USB slot of the PC that runs the control software. The KICK box provides six BNC connectors for the connection to the linac, the FPI and the x-ray console. Figure 5.4 shows a photo of the box. The different modes and SW-switchable features are selected by setting the corresponding digital



Figure 5.4: KICK box

*At the front side (left) an LED indicates if the box is connected to the PC. At the back side the BNC connectors and the USB cable are applied.*

outputs of the PC card. The KICK box is connected via the BNC connectors to the following signals and inputs of its periphery: i) Linac HV-signal, ii) linac RO-signal, iii) linac gating input iv) FPI trigger input, v) x-ray console HW-trigger, and vi) x-ray console rad-on signal. The linac HV-signal indicates the start and end of each treatment field[3] by its rising and falling, respectively. The RO-signal is HIGH whenever the MV-beam is on. The TTL state of the HV- and the RO signal differs during the adjustment of two treatment segments of one treatment field and during MV-gating. The applied FPI does not supply a direct feedback of its actual readout state, i.e. the KICK box retrieves no information about the moment the FPI has finished a triggered readout and is ready for the next trigger. By the SW-selection the KICK box can use an internal timer to obtain a potentiometer adjustable integration time. In the following, the procedures of the different modes are described:

---

[3]In IMRT a 'treatment field' may contain several field- (or treatment) segments of the same gantry angle that are combined to one *IMRT group*. IMRT segments from different gantry angles belong to different treatment fields.

- **Single shot mode**

  Single shot request from SW

  gate MV-beam and stop permanent FPI trigger (if necessary)

  Ⓢ $\begin{cases} \text{wait for FPI to finish readout of current frame (if necessary)} \\ \text{trigger FPI readout} \\ \text{wait for FPI readout to be finished} \\ \text{trigger x-ray pulse} \\ \text{wait for end of x-ray pulse} \\ \text{signalize kV-image acquisition via digital PC card input} \\ \text{trigger FPI readout} \\ \text{wait adjusted integration time or for FPI readout to be finished} \end{cases}$

  release MV-beam and FPI permanent readout trigger.


- **Positioning mode**

  Start of treatment field (HV signal raises)

  Ⓢ

  wait for *position OK* signal from SW

  release MV-beam (+ FPI permanent readout trigger, where required)

  wait for subsequent treatment field.

▶ *Single shots* are possible during beam-off phases.


- **Fluoroscopy mode**

  Start of treatment segment (RO-signal raises)

  ↪

  start *fluoroscopic frequency* timer

  wait for timer to finish⋆

  gate MV-beam and stop permanent FPI trigger (if necessary)

  Ⓢ

  reset timer

  continue at ↪

  ⋆If end of treatment segment appears before: reset timer and wait for next segment.

The wild card Ⓢ stands for the sub-procedure that is marked at the description of the single shot mode. The fluoroscopic frequency can either be adjusted at a KICK box internal timer by means of an analog output voltage, or via the PCI timer card (not applied within the work). The frequency can be changed online at any time. With the start of each treatment field, a short MV-gating pulse is generated to avoid a timeout interlock at the linac that may appear in gating mode. A treatment resumption after an interruption caused by an interlock or a user intervention at the linac console is always handled as a new treatment field.

Imaginable applications of the KICK box are, for instance:

– Positioning of the target volume my means of the 2D projection (that optionally contains the actual MV field shape when applying the MV field overlap) before the application of every treatment field with the positioning mode.

– MV-beam gating on the basis of breathing motion that becomes visible in fluoroscopic mode.

– Control projections in single shot mode during beam delivery followed by gating of the MV-beam if necessary.

– ...

Applying overlapped MV fields may facilitate the analysis of the projections and the decision about a potential intervention of the treatment process[4].
The interactions of the KICK box with the components of the imaging system to which it is directly connected are summarized in figure 5.5. A software module was provided that, among other things,
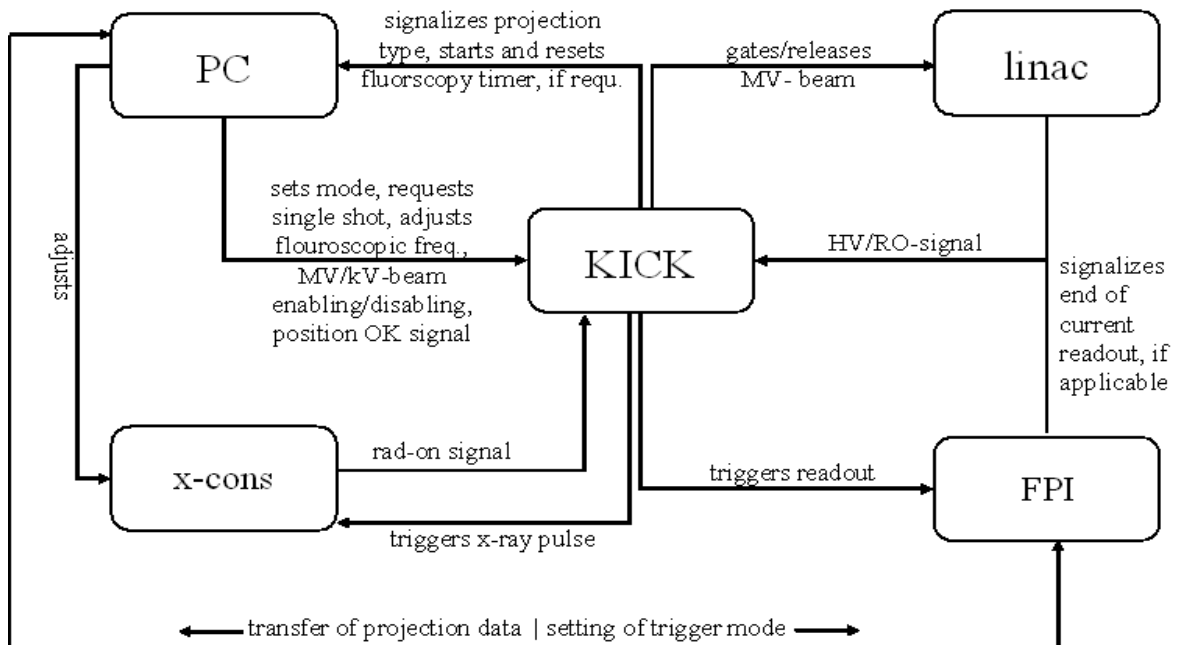


Figure 5.5: KICK box interactions with imaging components

*The KICK box is connected via an USB I/O card to the PC running its control software, to the rad-on and HW-trigger line of the x-ray console, to the gating, RO- and HV lines of the linac and to the trigger line of the FPI. It synchronizes special (2D) kV-imaging applications during treatment as illustrated and described in the text. The arrows indicate the direction of the signals or information flow.*

supports the different modes and features of the KICK box and includes an interface to the FPI for image data transfer. Figure 5.6 shows a screenshot of this tool.

---

[4]To apply an authentic MV field overlap on the kV-projections a (ideally automatical) postprocessing of the images must be applied that stretches the MV beam shape to its isocentric size and, if necessary, corrects the position on the projection on basis of the calibration matrices. This feature is not implemented yet.
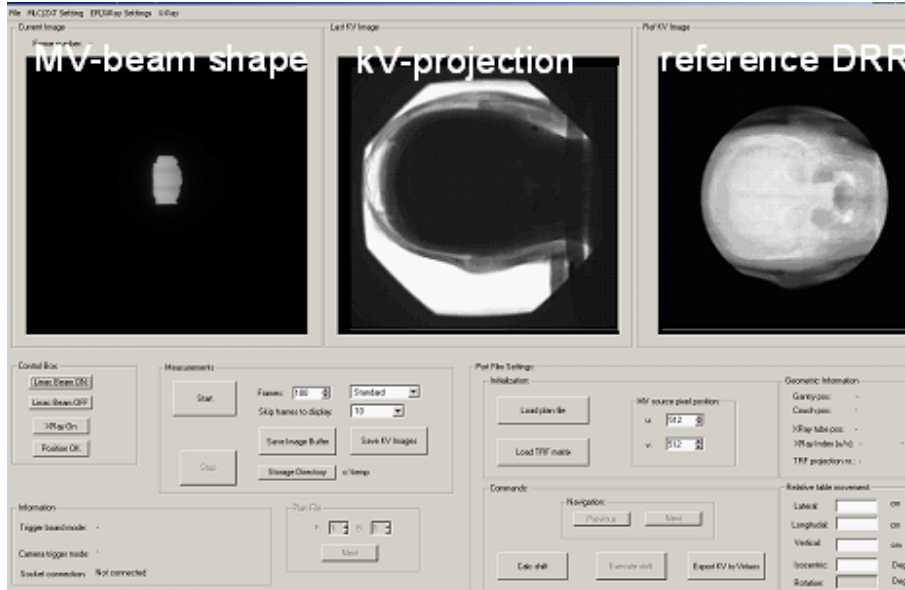
Figure 5.6: Software control for KICK box

*The software module supports the KICK box. The three image panels separately display current MV-and kV-projections. Additionally, a reference DRR of the phantom/patient at the actual projection angle obtained from the planning CT may be loaded for comparison purposes. The online application of a matching algorithm allows a 2D-based calculation of the shift between the kV-projection and the DRR, which optionally may be corrected by an automatic table shift.*

## 5.5 Special features II - 4D imaging

The time requirement for the acquisition of a linac integrated CBCT is at least $\frac{\Delta\gamma_{\min}}{v_{\max}} \approx 40\,\mathrm{s}$ and can be arbitrarily increased by gantry rotation slowdown. During this time the patient passes through several breathing cycles. Therefore, when scanning the lung, the single projections do not represent a static object; assuming so may lead to motion artifacts in CT reconstruction. There are approaches for motion artifact reduction using a pixel-specific filtered back projection [65]. One way to reduce motion artifacts on the projection level is to consider only those projections that were acquired at or around a certain breathing phase or amplitude [66] – [69], assuming a fixed correlation between the breathing phase or amplitude and the respiratory motion. This is given for the *moving lung phantom* shown in figure 5.7 [70]. The phantom performs a motor driven rigid motion in the CC direction. A real-time readout of the motion amplitude is provided by means of a linear sliding potentiometer. The amplitude is always well-defined by the active resistance of the potentiometer. The correlation between resistance and phase is motion disc dependent and it is $R(\varphi) = R(\pi - \varphi)$ with $\varphi \in [0, 2\pi]$ the motion phase and $R(\varphi)$ the corresponding resistance. A comparator circuit was built with a digital output providing a high TTL signal above a certain (adjustable) motion amplitude and a low signal below. This signal can, for instance, be used for MV-beam gating; this means the treatment beam is only released at a certain level around expiration or (by signal inverting) inspiration phase[5].

To obtain real-time information about a patient's breathing phase, the respiratory gating system (RGS) *AZ-733V* from Anzai Medical (see figure 5.8) is available [68], [71]. This system provides a stretchable belt with a pressure sensor that is tied around the patient's abdomen. The analogue sensor signal caused by respiratory motion of the patient is sampled by the system and supplied to a PC software that displays and stores it together with corresponding time flags. A gating signal,

---

[5]The *inspiration phase* is represented by the highest, the *expiration phase* by the lowest motion amplitude of a certain motion disc.
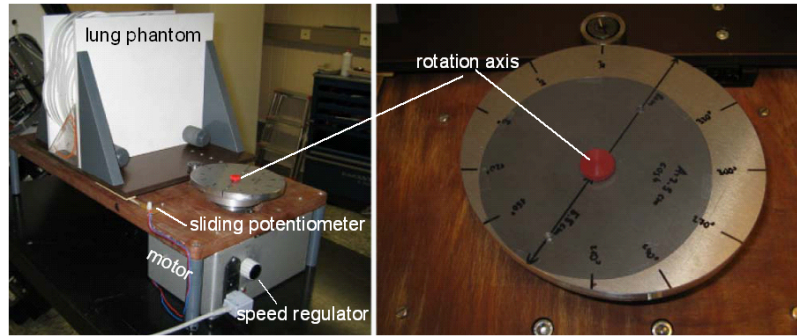
Figure 5.7: Moving lung phantom

*The phantom consists of RW3 plates with embedded lung equivalent material and an artificial tumor. The motor rotation is transformed into CC directional motion of the phantom via irregularly shaped motion discs defining the gradient and the amplitude of the motion. A power supplied linear sliding potentiometer attached to the phantom can be used for position amplitude measurement.*
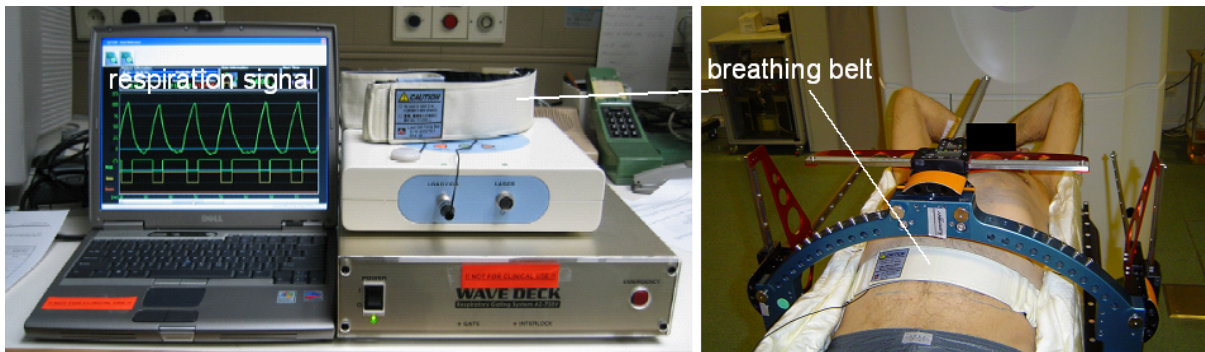


Figure 5.8: Respiratory gating system

*A pressure sensor in an expandable breathing belt is used for respiration tracking. The belt is tied around the patients abdomen (right picture) and stretches or compresses as a result of respiratory motion. A connected PC is supplied with the pressure signal for further processing.*

as described for the moving lung phantom, is provided between two user defined signal levels. The sensor provides only indirect information about respiratory motion by means of measured pressure. Furthermore, the signal amplitude depends on several factors that may vary from day to day for the same patient, like initial belt tension and belt position. The correlation between the relative pressure signal and diaphragm position (in the CC direction) was analyzed for several patients by means of x-ray projections that were acquired during respiration tracking [67], [68]. The evaluation showed impressive agreement even for extreme cases like patient coughing. Therefore, the system may be suitable to provide absolute amplitude information of respiratory motion[6] after a calibration based on simultaneous fluoroscopic x-ray acquisition and pressure signal tracking for at least one respiration phase. This calibration must be performed after every fastening of the breathing belt. To avoid a slipping of the belt that may nullify the calibration it should be performed in treatment position, i. e. using the linac integrated kV-imaging system.

**The 4D box**. To utilize the breath-dependent[7] gating signals for kV-imaging, an additional hardware component was built that is connected to a PC via an USB I/O card. The *4D box*

---

[6]From here on the respiratory amplitude refers to the diaphragm position in CC direction, which is not necessarily correlated with the remaining anatomy including possible existing tumors.

[7]The motion of the lung phantom motion is figuratively equated with *breathing*.

is connected upstream of the hardware trigger input of the x-ray console, and applies the gating signal of the lung phantom or the Anzai system in conjunction with the RO-signal for kV-triggering purposes. It features the following software selectable modes:

**CBCT mode:** This mode provides normal CBCT or 2D acquisition, ignoring the gating signal for x-ray trigger generation. However, it supplies the control software with the states of the x-ray trigger and, if existing, the gating signal, that are stored together with a time flag in a log file at a user defined sampling rate.

**4D-CBCT mode:** In this mode x-ray trigger signals are generated only when the gating signal provides a high (or optionally low) TTL signal. Therefore, every projection acquired in this mode belongs to certain breathing phase/amplitude interval. Besides the gating- and trigger signal, the control software is supplied with the intended x-ray trigger signals that were blocked due to wrong gating signal states.

**Static fluoroscopy mode:** In this mode an x-ray trigger signal is generated at every rising (optionally: and/or) falling edge of the gating signal. Therefore, every projection represents the same breathing phase/amplitude. The software is supplied with the trigger signal.

**Triggered fluoroscopy mode:** This mode provides the acquisition of a fluoroscopic sequence starting with the first rising, or optionally, falling edge after pressing the start button at the control software. The fluoroscopic frequency and the total sequence time are software selectable and transmitted to internal timers of the 4D-box via analogue output lines of the PC card. The control software is supplied with the gating and the trigger signal.

If imaging dose matters, the 4D-CBCT mode might be the best choice for CBCT acquisition of a certain predefined breathing amplitude interval. In this mode it is possible to acquire just the relevant projections during gantry rotation by appropriately adjusting the gating level. In this case, an off-line offset correction of the projections might be a necessary post-processing step due to possibly varying integration times of the projections. The integration times arise from the log file, as well as the mapping of the projections to their corresponding geometrical calibration matrix. To keep the option of reconstructing an arbitrary breathing amplitude interval, the CBCT mode must be used. In this case, the CBCT projections can be used for breathing amplitude calibration of the pressure sensor signal. The projections belonging to a certain amplitude interval can be found by means of their time flags and respiration signal log file.

The stability of the sensor calibration can be controlled using the static fluoroscopy mode. Sequences acquired in this mode should not show any respiratory caused motion. By applying the option to acquire projections both at the rising and at the falling edges of the gating signal, i. e. of different phases at the same amplitude, possible existing hysteresis effects between inhaling and exhaling can be evaluated.

Starting at a well-defined pressure signal level, and providing projections with a well defined frequency, sequences acquired in triggered fluoroscopy mode are well suited for a calibration of pressure signal to respiration amplitude.

Further 4D imaging methods, studies of the described phantom, and several patient applications using the described imaging system and 4D relating components are considered in [66] – [68].

## 5.6 Limitations & Upgrades

After a series of tests and phantom studies, the linac integrated kV-imaging system was considered suitable for first patient applications. During two clinical sessions, (3D-)CBCTs of seven patients classified into three head and neck cases, three prostate cases and one lung case, were acquired for positioning control purposes. Although the patients were not treated at the same linac, and only an off-line positioning control was performed, the CBCTs were used as substitutes for routinely taken MV-port films. While the port film acquisition exposure may result in imaging doses of up

to $5\,\mathrm{cGy}$, the imaging doses for the CBCTs ranged between approximately $1-2\,\mathrm{cGy}$ for the head and neck cases and $3-4\,\mathrm{cGy}$ for the extra-cranial cases. The equipment used thus far did not allow the treatment of the patients immediately following the CBCT acquisition at the same linac, for several reasons: i) The research version of the linac firmware needed for gantry angle feedback during CBCT acquisition was not released for patient treatment. ii) The used FPI is not designed to get irradiated with the dose rates applied during treatment. The high over-saturation caused by the MV-irradiation at the short distance from the FPI to the MV source may lead to long-standing afterglow effects and to long-term dark current increments.

For clinical applications, it is neither reasonable to change PROMS and remove the FPI between imaging and treatment, nor to decrease the dose rate.

The following sections describe changes and upgrades of the imaging system that have been performed during the further development process to overcome these and other limitations.

### 5.6.1   Inclinometer as substitute for CBCT PROMs

To reduce the interference of the kV-imaging system with treatment matters, an incremental inclinometer was attached at the gantry to obtain gantry angle feedback for kV-CBCT acquisition without the need of PROM replacement. The used inclinometer provides 3600 codes per revolution yielding an angular resolution of $\frac{1}{10}$ degrees. Internal magnetic damping assures fast response times while avoiding oscillations during gantry deceleration and acceleration. Since the inclinometer does not provide absolute gantry angles, no type of calibration is needed after the fixation to the gantry. An additional cable had to be passed through the gantry for power supply of the inclinometer and signal transfer of its 2-channel quadrature outputs. To integrate the inclinometer into the given setup, an additional hardware component, the *iBox*, was built to convert the inclinometer signals into x-ray trigger pulses for CBCT acquisition. The iBox provides the power supply for the inclinometer and is connected upstream of the hardware trigger input of the x-ray console or, if used, of the 4D-box. It uses as inputs the RO-signal and the inclinometer outputs. Angular spacings of $0.5°$ or $1.0°$ for CBCT acquisition are adjustable by jumper setting. Higher values of the angular spacing are not supported in order to avoid the occurrence of streak artifacts; lower spacings are not supported due to time and dose constraints[8].

CBCT acquisition using the standard firmware is performed in a manner analogous to that with the research PROMs (see section 5.2) apart from the setting of pulse length and angular spacing, which is no longer needed. During a common rotational treatment, the RO-signal rises as soon as the gantry rotation starts, and stops as soon as the gantry angle reaches its stop position. The gantry rotates a bit further to avoid deceleration between the start and stop angle. The iBox generates x-ray trigger signals only if the RO-line provides a high output signal. The first x-ray trigger is produced with the rise of the RO-signal, the following ones in intervals of $0.5°$ or $1.0°$. No x-ray pulse is triggered after the stop angle is reached.

Following figure 5.3, figure 5.9 shows the chronology of the signals for a CBCT acquisition (without 4D-box) using the inclinometer instead of the CBCT PROMs.

---

[8]Lower angular spacings result in a higher number of projections requiring a certain minimum dose for each projection. Furthermore, the minimum FPI integration time might force a gantry speed reduction.
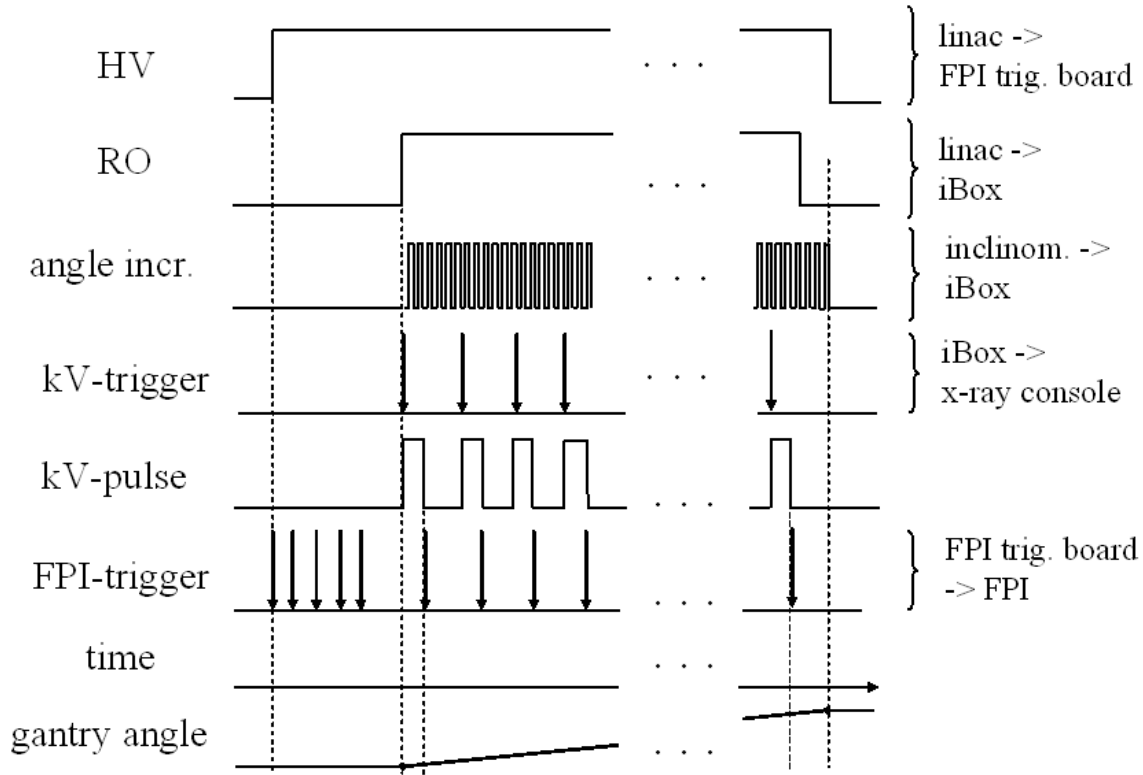
Figure 5.9: CBCT signal sequence with inclinometer

*The x-ray trigger pulses are generated by the iBox on the basis of the inclinometer signals. The first pulse appears with the rise of the RO signal. After the gantry reaches the intended stop angle, no further x-ray pulses are produced.*

### 5.6.2 FPI upgrade

The FPI used so far with a minimum integration time of $t_f = 285$ ms, limits the gantry speed for an CBCT acquisition with an angular spacing of $\Delta\Theta = 0.5°$ and an x-ray pulse time of $t_p = 20$ ms to $v < \frac{\Delta\Theta}{t_p+t_f} \approx \frac{100°}{\min}$. To support the maximum gantry speed of $v_{\max} = \frac{300°}{\min}$, an integration time of $t_f < 80$ ms is required.

With the given imaging setup, isocentric imaging doses at the water phantom of $D \gtrsim 45\,\mu$Gy per projection lead to FPI saturation outside the phantom shadow. Although better image quality may be obtained with higher imaging doses (see section 2.3), a further increment of the exposure would result in a truncation of the phantom edges. A higher saturation charge of the FPI would overcome this limitation. On the other hand, a lower saturation charge may lead to higher non-saturated gray values at the same imaging dose for a certain ROI inside the phantom shadow, and thus results in a higher SNR (due to a lower fraction of pixel- and dark current noise) and a better contrast resolution caused by a higher dynamic range of the projection.

To avoid saturation during MV beam tracking, both a higher saturation charge and a reduced FPI integration time are useful.

With the *XRD 1640 AN ES* a version of the FPI supporting the above described requirements was provided. The main properties agree with those of the thus far used RID 1640 AL1, but it applies a maximum frame rate of 15 Hz ($t_f \approx 67$ ms) and a selectable gain setting yielding saturation charges of $2.5 \cdot 2^n\,pC$, $1 \leq n \leq 5$. The gain level $n = 1$ corresponds to the saturation charge of the FPI used so far. The *new* FPI allows CBCT acquisition with an angular spacing of $0.5°$ at the maximum gantry speed $v_{\max}$. Applying $n = 5$ and the free running mode with the fastest integration time,

it does not saturate when irradiating it with $250 \frac{\text{MU}}{\text{min}}$ at the intended distance to the MV source (58 cm) for MV field sizes up to $30 \times 30 \, \text{cm}^2$.[9]

### 5.6.3   KV source upgrade

From the first clinical experiences with linac integrated CBCT acquisition an estimate of actual requirements of the tube and generator capability for a clinical situation could be made. Exposures for CBCTs of the pelvic region have already been limited by the load charts and heat capacity constraints of the thus far used kV source. For clinical practice, the imaging system should be designed to have the ability to perform CBCT scans in 15 – 30 minute cycles. Furthermore, fluoroscopic sequences might be applied in between. The given kV source was found to be inappropriate for the required exposures and duty cycles. Therefore, the kV source was replaced by an *OPTITOP 150/40/80* x-ray tube from *Siemens* powered by a *Polydoros A100* x-ray generator, considered to fulfill the requirements. The properties of this kV source are summarized as follows:

| | | |
|---|---|---|
| Nominal voltage (maximum) | 150 kV | |
| Focal spot nominal value | small focus: 0.6 | large focus: 1.0 |
| Nominal power | small focus: 40 kW | large focus: 80 kW |
| Anode target anlge | 12° | |
| Anode material | Rhenium-tungsten, molybdenum, graphite | |
| Anode heat storage capacity | $5.8 \cdot 10^5 \, \text{J}$ | |
| Tube assembly heat storage capacity | $1.8 \cdot 10^6 \, \text{J}$ | |
| Max. anode heat dissipation | $1.2 \cdot 10^5 \, \text{J/min}$ | |
| Max. heat diss. of tube assembly | 300 W | |
| Max. average anode input power | 300 W | |
| Inherent filtration (IEC 60601) | 2.5 mm Al | |

The increased tube power and heat storage capacities allow higher exposures and duty cycles. Again, the tube is switchable between two focal spots. For all applications within this work, the smaller focal spot is used unless otherwise noted. The same holder was used to mount the tube at the linac at an unchanged SID of approximately 100 cm. Again, the anode-cathode direction is parallel to the y-axis of the room system with $y_{\text{cathode}} > y_{\text{anode}}$. The tube is delivered with a removable rectangular field collimator. The field size can be adjusted independently in the u- and v-directions but not asymmetrically with respect to the central ray. Furthermore, an additional copper filtration of 0.1 mm, 0.2 mm or 0.3 mm can be applied to harden the beam spectrum. Unless otherwise noted, the kV-beam is collimated to fully illuminate the active area of the FPI and no additional filtration is applied. A picture of the modified setup is shown in figure 5.10.

   The replacement of the kV source required minor hardware and software adaptations. For one thing, a hardware module was built, which is interposed between the x-ray console and the x-ray generator to transform the SWR signal according to changed specifications. Furthermore, two additional hardware signals provided by the generator are transformed to TTL signals for further processing purposes. The x-ray pulse feedback (anode current and pulse time) is no longer transmitted via CAN protocols, but frequency encoded via a hardware line ($10^6 Hz \stackrel{\triangle}{=} 1A$). The second signal indicates the beam-on phases. For tube output analysis, the frequency pulses during each beam-on phase are counted. Single x-ray pulses are separated by means of a hardware beam-on indication. However, by only counting the frequency pulses, the x-ray pulse feedback is no longer split up into the pulse time and the anode current, but given by the fluence proportional product $I \cdot t = 10^{-6} \frac{As}{\# \, \text{counts}}$. The proportionality of tube output and frequency pulse counts was analyzed similarly to section 4.5.1. Twenty five different combinations of pulse length and anode current (I = [10,20,40,80,160] mA and t = [5,10,20,40,80] ms) at U = 120 kV were set at the control software.

---

[9]MV field sizes refer to the isocenter plane unless otherwise noted.

The Optitop x-ray tube is installed at the linac the same way as the P 125 tube but comes along with a new rectangular collimator. At this picture the MLC is at 0°, and therefore the y-axis of the FPI is antiparallel to the room y-axis.

Figure 5.10: Optitop @ linac

The mean charge produced during 50 pulses in the ionization chamber placed within the primary x-ray beam were measured at each setting as a function of the mean corresponding frequency pulse counts. Deviations of the counts-per-measured-charge quotient ($CPC$) from a constant value were assumed to result from a frequency pulse offset. Therefore, all counts were corrected by subtracting a constant offset $f$ to calibrate the generator feedback for measured charge. To obtain the best correction value, the standard deviation of the corrected $CPC(f)$ as a function of $f$ was minimized. It was found, that applying $f = 130$ showed the best proportionality of the corrected frequency pulse counts and the measured charge at the ionization chamber. Figure 5.11 shows the uncorrected $CPC\,(f = 0)$ and $CPC\,(130)$. Furthermore, the standard deviation of $CPC(f)$ is plotted against $f$. The correction was implemented into the pulse count analysis of the control software, so that a
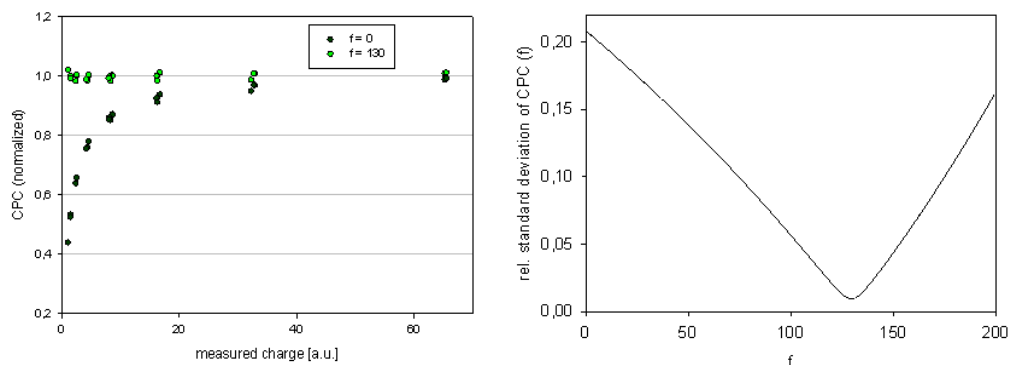


Figure 5.11: Calibration of generator feedback

*The deviations of the CPC from a constant value could be corrected for by offset subtraction from the counted frequency pulses. The deviations of CPC (130) from a constant value stay below 2% for all measured charges (left). The standard deviation of CPC (f) has a minimum of less than 1% at f = 130 (right).*

corrected $I \cdot t = 10^{-6} \frac{As}{\# \text{counts - 130}} \propto D$ (D: imaging dose at an arbitrary point of the imaged object) is written to the text file for each pulse. The written output does not necessarily represent the exact $I \cdot t$ but nearly coincides with adjusted values, especially for high tube outputs.

### 5.6.4   Antiscatter grid

As an addition to the imaging system an antiscatter grid became available. The overall size of the grid coincides with the active area of the FPI. The FPI holder was upgraded with a special antiscatter grid holding, allowing one to insert and fixate the grid at the front side of FPI towards the x-ray source. The grid can be orientated along the u-direction, i. e. the grid lines are perpendicular to the axis of rotation; or it is oriented along the v-direction, meaning the grid lines are parallel to the axis of rotation during a CBCT acquisition. The used antiscatter grid absorbs approximately 30% of the primary beam intensity of the 120 kV spectrum. Therefore, the tube output must be increased by a factor of approximately 1.4 to achieve gray values at the FPI projections that are similar to those obtained without an antiscatter grid. The influence of antiscatter grids on CBCT imaging is discussed in more detail in [72].

## 5.7   System calibration measurements

### 5.7.1   Imaging dose calibration

A dose calibration for the new kV source was performed according to section 4.5.3. The water phantom was attached to the treatment table and placed with its longitudinal axis along the room y-axis and its center at the isocenter. The treatment table is outside the FOV at any projection angle. Additionally, a body phantom (figure 6.23a) was used to obtain an estimation of imaging doses resulting from extra-cranial CBCTs scans. This phantom was placed on the treatment table. For dose measurements, 360° CBCTs of the phantoms were acquired with the ionization chamber located at the phantom centers. The measurements were performed using a 120 kV spectrum and different additional filtrations provided by the kV source. Calibration factors were calculated on the basis of the measured dose and the cumulative tube output of the corresponding CBCT sequence. Additionally, the mean energy of the primary beam was calculated for each filtration on the basis of spectra simulations using the *x-ray toolbox*. The results are summarized in table 5.1.

Table 5.1: Imaging dose calibration factors for CBCTs with the Optitop tube

| | calib. factors [mGy/As] | | | |
|---|---|---|---|---|
| Additional filtration [mm Cu] | none | 0.1 | 0.2 | 0.3 |
| Mean spectrum energy [keV] | 56.6 | 60.7 | 63.5 | 65.7 |
| Water phantom | **70** | **57** | **49** | **42** |
| Body phantom | **44** | **37** | **33** | **29** |

*The calibration factors are given in $\frac{mGy}{As}$. They are based on the measured dose at the phantom center during one 360° CBCT scan and on the cumulative corrected $I \cdot t$ values written to the corresponding text file. The beam attenuation in the additional copper filtration leads to hardened spectra resulting in higher mean energies and to lower primary fluences resulting in lower doses. A 2.5 mm Al filtration is always existing.*

These values are used for dose estimations of similarly sized phantoms or body parts imaged with the new kV source.

### 5.7.2 Reliability of geometrical calibration

To illustrate deviations of the linac integrated kV-imaging system from an ideal imaging geometry, figure 5.12 shows the distance of the isocenter projection coordinates from the detector center as a function of the projection angle. This was measured by acquiring a CBCT sequence of the isocentric adjusted calibration phantom. The projection coordinates were calculated by means of the obtained projection matrices for each projection angle.

The reproducibility of the non-ideal projection geometry determines the stability of the imaging
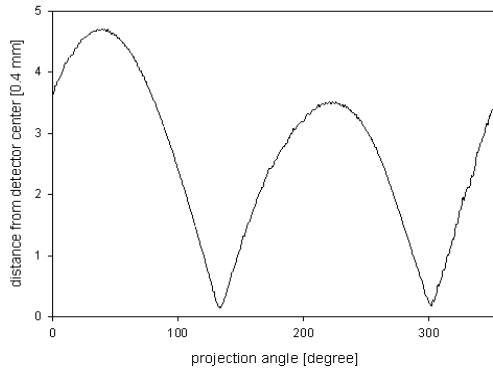


*Distances are given in pixels. The variations indicate a non-ideal projection geometry that must be corrected for by geometrical calibration.*

Figure 5.12: Distances of isocenter projections from detector center

system's geometrical calibration and is an important issue for accurate CBCT reconstruction. Reliability tests were performed by multiple CBCT acquisition of the calibration phantom and generation of corresponding projection matrices. In a preliminary test, four sets of projection matrices were determined from four different calibration sequences ($\Theta_{\text{start}} = 0°, \Delta\Theta = 1.0°, \Theta_{\text{start}} = 360°, v = \frac{200°}{\text{min}}$, each) acquired during one day without moving the calibration phantom inbetween. The calibration phantom was roughly adjusted with the help of the room lasers. The phantom center does not necessarily coincide exactly with the isocenter. By means of the projection matrices, the projection coordinates of 21 points with a distance between 0 and 20 cm from the origin of the patent coordinate system (i. e. the center of the calibration phantom) were calculated. The coordinates of the points are: $x = y = z = \frac{n}{\sqrt{3}}; n = 0, 1, 2, \ldots, 20$. For each point at each projection angle, the maximal deviation of projection coordinates between the four calibration sets were calculated. Figure 5.13 shows these deviations for four different projection angles and for three different points, respectively. In a second test, the influence of a gantry speed variation on the calibration reliability was analyzed. For this purpose, two calibration CBCTs were acquired in two sessions with two different gantry speeds each. Both times, the gantry speeds were set to $v_1 = \frac{200°}{\text{min}}$ and $v_2 = \frac{90°}{\text{min}}$, respectively. The other parameters were fixed to $\Theta_{\text{start}} = 0°$ and $\Delta\Theta = 1.0°$. The maximum deviations of projection coordinates between both speeds were again evaluated for every projection angle and the 21 above defined points. The results are illustrated in figure 5.14).

The plots indicate a good reproducibility of the projection geometry when using a fixed rotation speed. Deviations at the detector plane of 0.5 pixels correspond to lateral distances of approximately 0.14 mm at the isocenter plane (perpendicular to the projection direction). Therefore, no deformations in the reconstructions are expected. When using a calibration for positioning purposes, an accurate adjustment of the calibration phantom is necessary. For pure imaging purposes, the absolute patient system coordinates may be less important.

Variations in gantry speed are shown to decrease the reliability of the geometrical calibration especially concerning peripheral points, where deviations up to 4 pixels ($\overset{\wedge}{\approx} 1.1$ mm at isocenter plane) were observed. To overcome such inaccuracies calibrations might be performed for all applied gantry speeds.
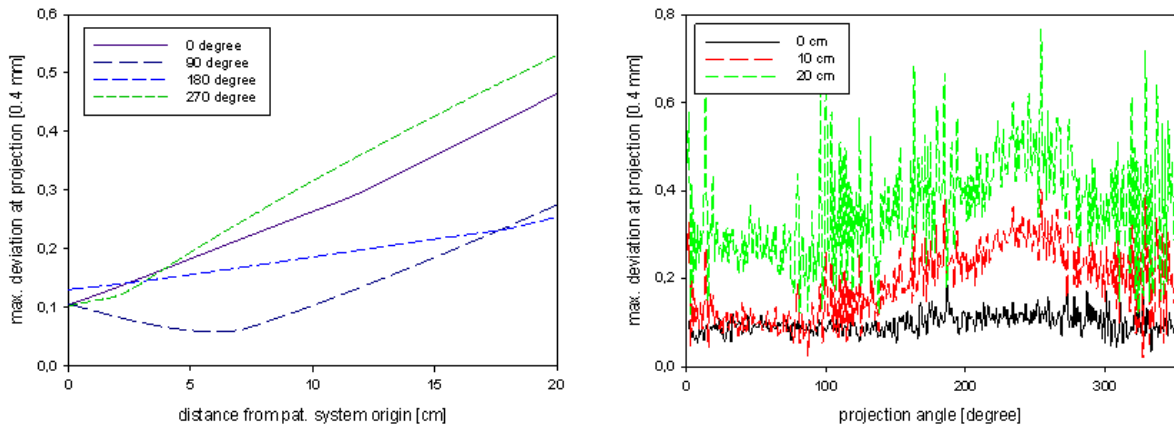
Figure 5.13: Calibration reliability

*The maximum deviation between the projection coordinates rises with increasing distance of the projected points from the center of rotation, but stays mainly below 0.5 pixels even for peripheral points. The slightly initial drop of the $90°$ and $270°$ curves may result from an inaccurate adjustment of the calibration phantom.*
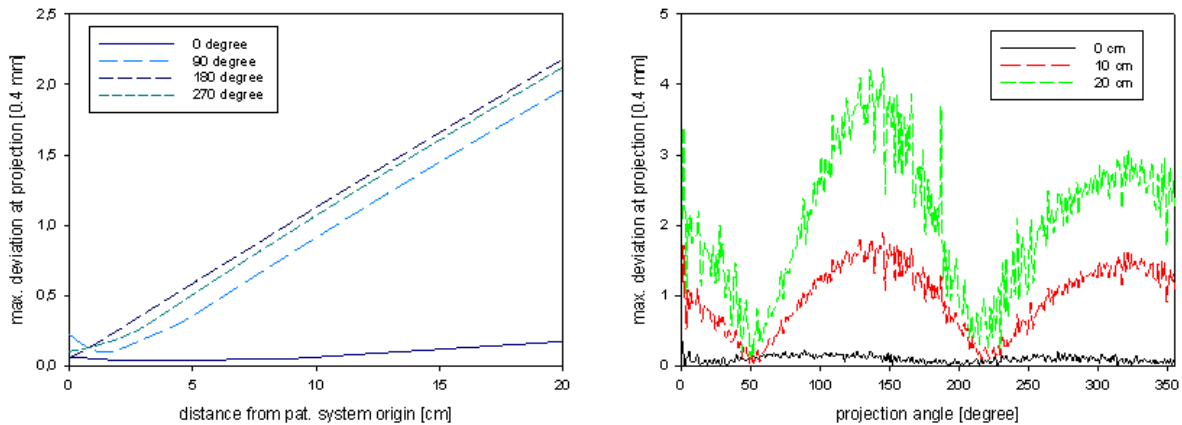


Figure 5.14: Calibration reliability for different gantry speeds

*The plots indicate a sensitivity of the geometrical calibration on the variation of the acquisition speed. The deviations at $0°$ between the calibration for $v_1$ and the calibration for $v_2$ are comparable to those of a constant speed (figure 5.13), resulting from the fact that the initial kV-pulse is triggered at $\Theta_{start}$ before the gantry has started to move (see figure 5.9).*

### 5.7.3   MV beam attenuation of the FPI

The Inline concept is arranged for an entrance MV beam tracking during treatment. In this case the FPI is located between the MV source and the patient. Therefore, properties of the treatment beam such as intensity and spectrum are different with respect to the commonly used non-attenuated MV beam. For photon treatment purposes, only the delivered dose distribution inside the patient is of interest. Therefore, measurements have been performed to analyze and quantify the influence of the FPI on the treatment dose. In a water tank, depth dose curves and lateral dose profiles with and without the FPI (without antiscatter grid) inserted into the accessory tray using an ionization chamber were measured.

Figure 5.15 shows the normalized depth dose curves for a central $10 \times 10 \, cm^2$ beam and the quotient of measured absolute doses with FPI ($D_w$) and without FPI ($D_{w/o}$). The FPI causes a beam
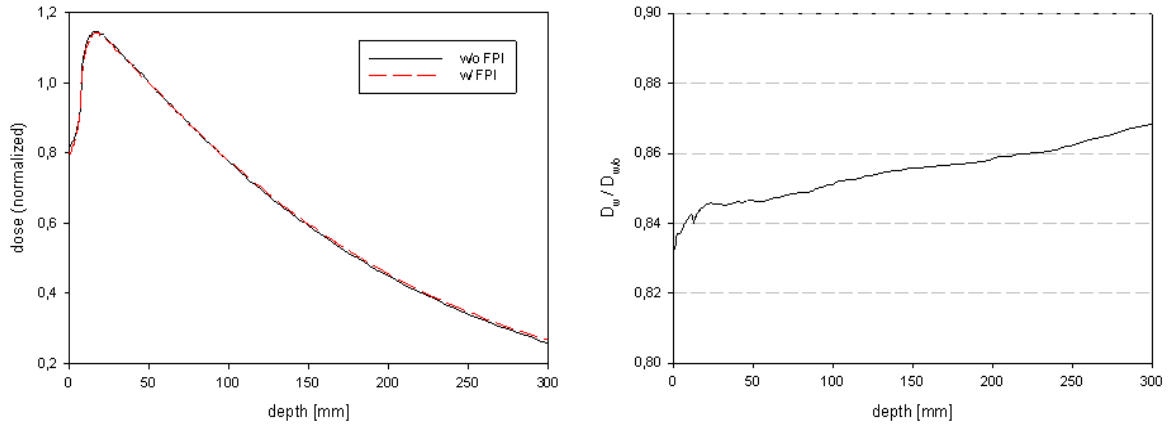


Figure 5.15: Depth dose curve comparison w/ and w/o FPI

*The normalized depth dose curves of the central ray measured in water with a 6 MV beam at an SSD of 100 cm and a field size of $10 \times 10 \, cm^2$ (left) and the absolute dose ratio are plotted (right). A slightly shifted maximum of $D_w$ towards deeper values and the slower decline are signs of a slightly hardened beam.*

attenuation of approximately 15 %. The spectrum is slightly, hardened resulting in a slightly changed gradient of the depth dose curve. The doses in water of the attenuated beam range between approximately 84.5 % of the non-attenuated beam behind the maximum and 86.5 % in a depth of 30 cm for a $10 \times 10 \, cm^2$.

Figure 5.16 shows a comparison of lateral dose profiles in the x-direction (room coordinates) at a water depth of 5 cm. No differences in the normalized profiles are visible. The absolute dose values have a constant ratio of approximately 84.5% along the profile.
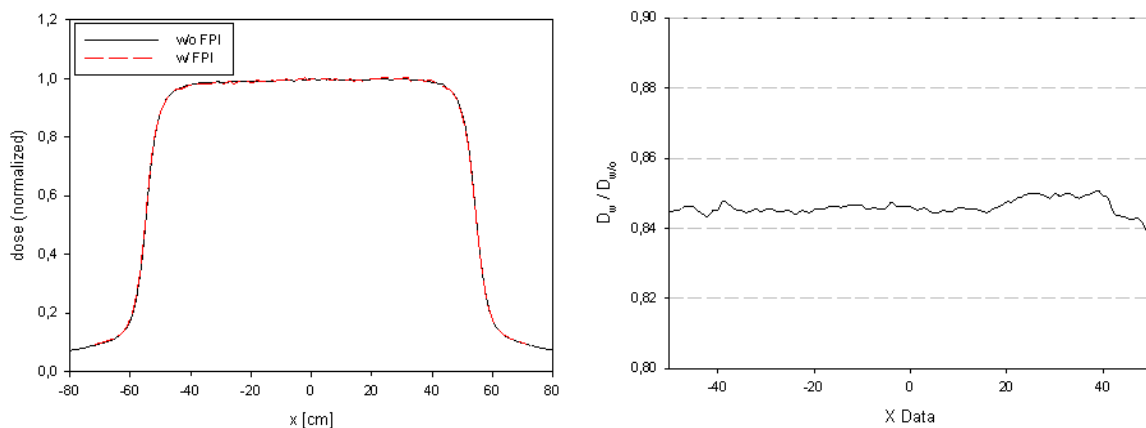


Figure 5.16: Dose profile comparison w/ and w/o FPI

*The dose profiles along the x-axis were measured at a water depth of 5 cm, an SSD of 100 cm and a field size of $10 \times 10 \, cm^2$. Throughout the profile the dose values with FPI are approximately 15.5 % lower than without FPI.*

Depth dose curves and dose profiles of other beam sizes and water depth show comparable results, which are discussed in more detail in [73]. The influence of the FPI must be considered for treatment purposes. This can be done by integrating the FPI (with and without antiscatter grid) into the planning system for dose optimization and calculation [74]. As a possible further solution, the scaling of the MUs of each treatment segment by a factor of 1.18 with respect of the treatment plan optimized without FPI was analyzed. This method requires, in any case treatment verification with FPI due to the disregard of the changed beam spectrum [76], [77]. Figure 5.17 shows an example of comparison of dose distributions carried out by film measurements. An original 7-beam IMRT plan optimized for a prostate cancer patient was applied on an IMRT verification phantom without FPI, as well as with FPI, and scaled MUs. The dose difference distribution and a gamma criteria
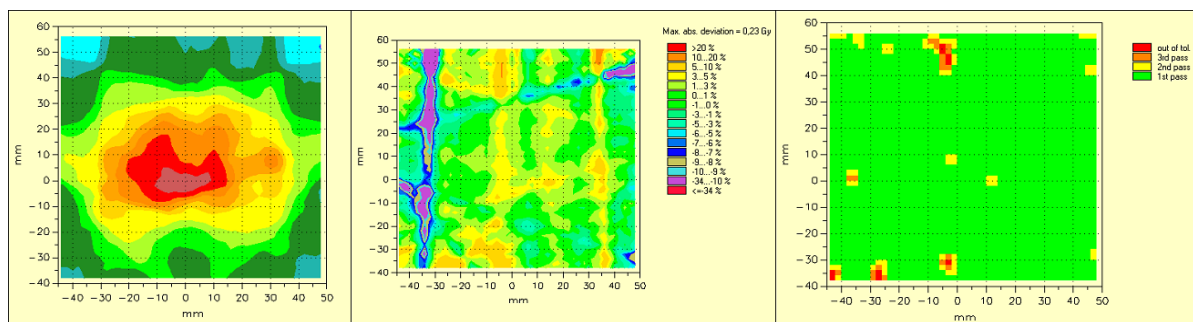


Figure 5.17: Comparison of IMRT dose distribution w/ and w/o FPI

*Left: Film measured dose distribution of the central transversal slice (patient system: z = 0) of a prostate cancer IMRT plan (without FPI). Middle: Dose difference distribution at z = 0 between the original IMRT plan and the scaled plan with FPI. The high-difference areas are passed at the gamma analysis of this slice (right). The parameters of the gamma analysis are $\Delta D = 3\%$ for dose difference and $\Delta d = 3\,mm$ for spatial distance.*

analysis [75] of the central transversal slice do not reveal any serious differences of the delivered dose. Other slices showed comparable results. Therefore, this case outlined the MU scaling of 1.18 as an adequate method for FPI consideration. More examples and detailed analyses are given in [73]. With the antiscatter grid, the scaling factor increases to 1.205.

# Chapter 6

# Investigations & Applications

In the previous chapters, the development of the linac integrated imaging system, as well as its associated components, features and applications, were described in detail. This chapter describes several investigations concerning imaging and image quality and describes clinical applications performed with this system thus far.

## 6.1 Investigations on CBCT image quality

In this section, several influences on CBCT image quality are experimentally analyzed. This is mainly done on appropriate phantoms by varying single parameters of the CBCT acquisition or reconstruction process. In the following, the already introduced contrast phantom (figure 4.7) and lung phantom (figure 5.7) are used. A view inside the phantoms is given in figure 6.1. The different inlays of the phantom are described in table 6.1.
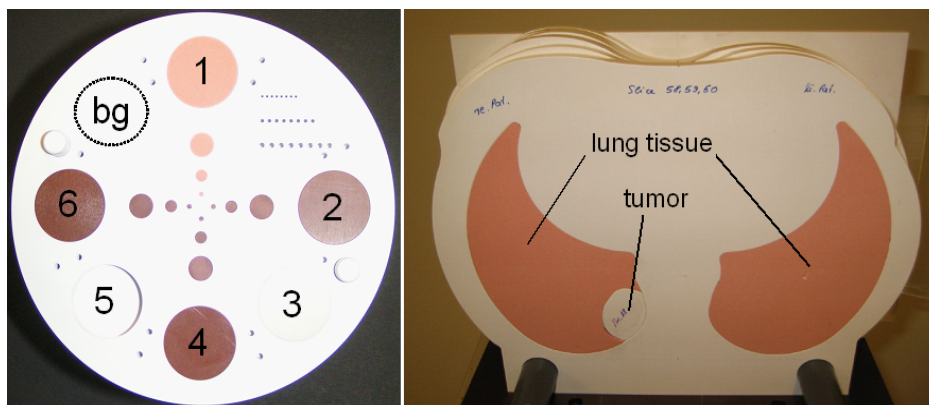


Figure 6.1: Inside view of the contrast- and the lung phantom

*The middle slice of the contrast phantom (left) is equipped with different inserts that are described in table 6.1. The diameter of the phantom is 16 cm; the inserts have diameters of 30 mm, 10 mm, 5 mm and 2 mm. The diameters and distances of the serially-arranged holes at the upper right part of the phantom are 2 mm, 1.5 mm and 1 mm, respectively. The lung phantom (right) is equipped with lobes-shaped lung tissue equivalent material and an artificial RW3 tumor.*

Table 6.1: Inserts of the contrast phantom

| insert | equivalent to | rel. electron density | HU at FBCT |
|:---:|:---:|:---:|:---:|
| 1 | lung tissue | 0.28 | $-739 \pm 27$ |
| 2 | muscle | 1.05 | $43 \pm 8$ |
| 3 | cortical bone | 1.69 | $1424 \pm 34$ |
| 4 | spongy bone | 1.11 | $259 \pm 10$ |
| 5 | air | 0.001 | $-1021 \pm 5$ |
| 6 | fatty tissue | 0.9 | $-109 \pm 6$ |
| bg | RW3 | 1.012 | $7 \pm 9$ |

*The numbers of the inserts correspond to the labels at figure 6.1. 'bg' is not a real insert, but represents the RW3 background of the phantom. The given HUs were measured with a diagnostic fan beam CT. The electron densities are given relative to the electron density of water. The lung equivalent inserts are formed out of a brittle polyurethane based material containing air holes (Obumodulan). It is, therefore, not homogeneous, which results in higher uncertainties of the HU determination.*

## 6.1.1 Impact of additional filtration

The collimator of the x-ray tube provides additional copper filtration of the x-ray beam, which can be used for hardening the primary beam (see table 5.1). To study the influence of the filtration on CBCT image quality, four CBCT scans of the contrast phantom were acquired applying 0 mm, 0.1 mm, 0.2 mm and 0.3 mm copper filtration, respectively, in addition to the existing 2.5 mm aluminium filtration. The scans were acquired as full scans with an angular spacing of $1.0°$ at $U = 120$ kV. The x-ray parameter $I \cdot t$ was adapted to the corresponding filtration by means of table 5.1 to keep a constant estimated imaging dose of 13 mGy for all scans. No antiscatter grid was used. The CBCT sequences were reconstructed with a $0.5 \times 0.5$ mm$^2$ resolution of the transversal slices ($p_x = p_y = 0.5$ mm). For evaluation purposes, the mean reconstructed attenuation coefficients ($\mu_1, \mu_2, \ldots, \mu_6$ and $\mu_{bg}$) and their standard deviations ($\sigma_1, \sigma_2, \ldots, \sigma_6$ and $\sigma_{bg}$) of the 30 mm inserts at the central slice were determined for each scan. As an indicator for contrast, the differences of reconstructed attenuation coefficients between each insert and the RW3 background[1] $C_i = |\mu_i - \mu_{bg}|$, and a contrast to noise ratio $\text{CNR}_i = \frac{C_i}{\sigma_i + \sigma_{bg}}, i = 1, 2, \ldots, 6$, is plotted in figure 6.2.

As expected, higher photon energies lead to lower contrasts (see figure 2.12). A reverse trend is visible for the CNR up to a additional filtration of 0.2 mm copper. This can be understood by analyzing the FPI gray values of the CBCT (raw) projections of the phantom produced by the different spectra. In figure 6.3, the mean gray value of a $100 \times 100$ pixels ROI at the middle of the phantom shadow within a corresponding projection of each CBCT scan is plotted as a function of additional filtration. An increasing detector signal $S$ having uncertainties of $\sigma_S \approx \sqrt{S}$ lead to lower uncertainties at the reconstructions[2] due to an increased SNR ($\approx \sqrt{S}$) and may therefore yield in a better CNR despite a lower contrast. The effect is reduced and the CNR decreases again by further beam hardening. The higher detector signal may not only result from a lower attenuation at higher energies, but also from a higher amount of scattered radiation, reducing both, the contrast and the noise.

---

[1] The absolute difference of reconstructed attenuation coefficients corresponds to the difference of displayed brightness when using a constant and linear windowing and can therefore be seen as a measure of visible contrast.

[2] $p \stackrel{(2.14)}{=} \int \mu(x)\, \mathrm{d}x = -\log(S \pm \sigma_S) \approx -\log S \pm \frac{\sigma_S}{S} \approx -\log S \pm S^{-\frac{1}{2}}$ (S already normalized to the non-attenuated signal.)
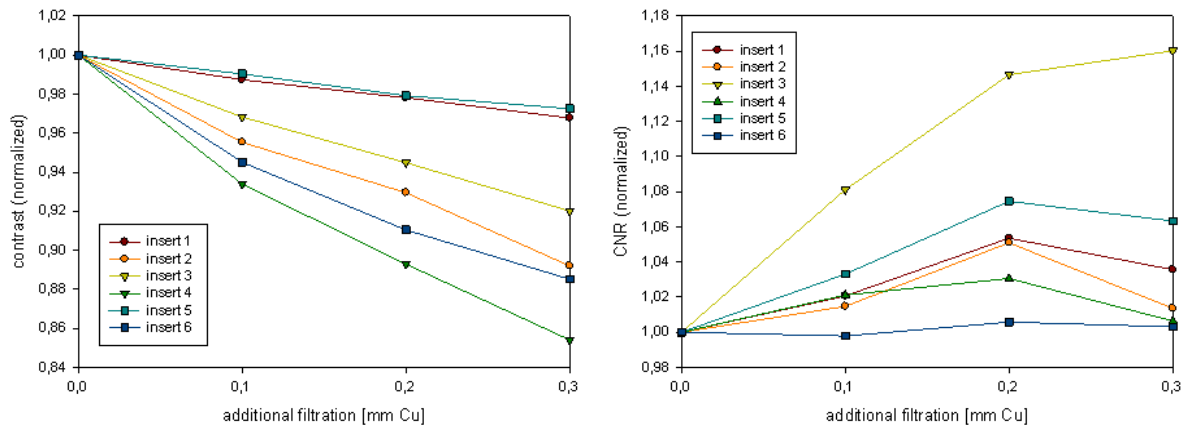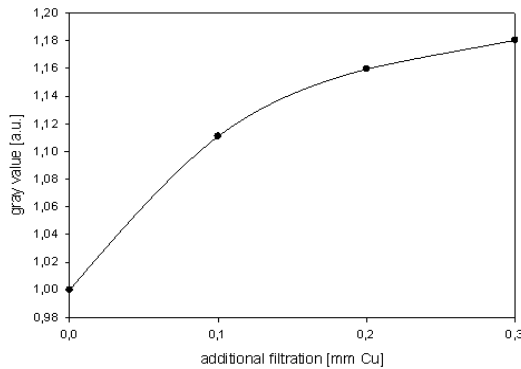
Figure 6.2: Contrast and CNR as a function of additional filtration

*Contrast and CNR are normalized to the 0 mm Cu scan for a better overview. The contrast decreases with the hardening of the energy spectra, while the CNR increases to a certain level. The CNR of the lung tissue equivalent insert 1 may not be well-defined due to the inhomogeneity of the material.*



*Due to lower attenuation, higher gray values are produced at the phantom shadow for higher energies at the same imaging dose. This trend weakens by further beam hardening due to a decreased detector response for higher energies.*

Figure 6.3: FPI signal at phantom scatter

## 6.1.2 Impact of imaging dose

To analyze the impact of imaging dose $D$ on image quality, four CBCT scans of the contrast phantom were acquired applying estimated isocentric imaging doses between $D = 3.8\,\text{mGy}$ and $D = 31\,\text{mGy}$. Full scans at an angular spacing of $1.0°$ were acquired without additional filtration and without an antiscatter grid. The sequences were reconstructed choosing $p_x = p_y = 0.5\,\text{mm}$. The contrasts $C_i$ are not expected to be significantly dose dependent. Therefore, the noise ratio $\frac{\mu_i}{\sigma_i}$ of the inserts and the background was analyzed as an indicator for image quality and is plotted in figure 6.4. An expected behavior of the curves can be estimated by the noise $\sigma_S$ of the projection signals $S$. Theoretically, it is $\sigma_S \propto \sqrt{D}$. This leads to an uncertainty of $\sigma_p \propto D^{-\frac{1}{2}}$ of the line integrals $p$ used for image reconstruction [$\sigma_p \approx S^{-\frac{1}{2}}$ (see footnote in section 6.1.1)]. Therefore, the noise ratios $\frac{\mu_i}{\sigma_i}$ can be expected to be proportional to $\sqrt{D}$. The deviations from the theoretical run may be caused, for instance, by influences of the discrete angular and spatial sampling at the CBCT acquisition, by scattered radiation and beam hardening, or by uncertainties occurring at offset- and open field correction, etc. [78].
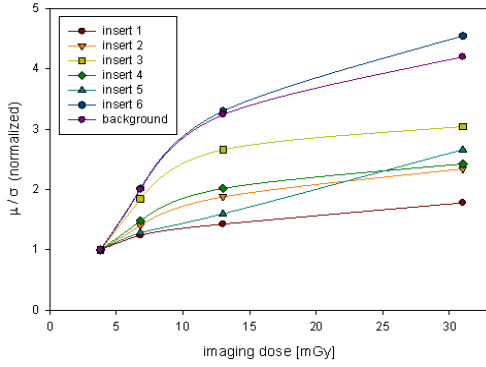
*Increasing SNRs at the projections at higher imaging doses ($SNR \propto \sqrt{D}$) leads to decreased noise in the reconstructions. Due to material inhomogeneities, $\sigma_1$ has an offset value and, therefore, shows the lowest relative reduction. The deviant behavior of the curve representing insert 5 (air) may be caused by the higher sensitivity on variations in $\sigma$ at $\mu_5 \gtrsim 0$.*

Figure 6.4: Dose dependence of noise ratio

### 6.1.3  Impact of projection compression

A rebinning of the projection data to $1024 \cdot 2^{-n} \times 1024 \cdot 2^{-m}$ pixels by neighborhood averaging should have similar effects on image noise as increasing the imaging dose, but decreases the spatial resolution of the projections and therefore also of the CBCT reconstructions. Furthermore, additional image artifacts may occur by an excessive compression due to the unification of overly large areas. To analyze the impact of compression, a CBCT of the contrast phantom was acquired (full scan, $\Delta\Theta = 1.0°$, $D \approx 13\,\text{mGy}$, no additional filtration, $p_x = p_y = 0.25\,\text{mm}$). The sequence was reconstructed four times with various compressions in the u-direction ($n = [0..3]$). No compression in the v-direction was performed ($m = 1$) to avoid interferences between different axial slices of the phantom[3]. Figure 6.5 shows the reconstructions of the central transversal slice for $n = 1$ and $n = 3$. The effects of an excessive compression are clearly visible. Not only does the
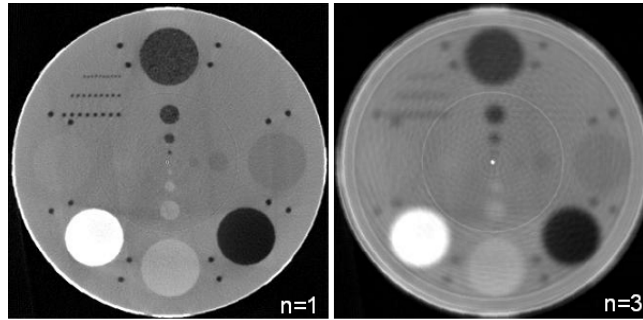


Figure 6.5: Reconstructions of rebinned CBCT projections

*Both images have the same gray level windowing. The rebinning with $n = 1$ delivers scatter reduced images with a good spatial resolution. Excessive compression ($n = 3$) may result in unusable reconstructions with high blurring and low spatial resolution. Artifacts such as the ring in the middle or at the border of the reconstruction, which might be caused by inappropriately corrected dead pixels, are emphasized in the reconstruction with the $n = 3$ compression.*

spatial resolution decrease significantly for $n = 3$, but the overall image quality appears to decrease dramatically. For quantification purposes the ratio $\frac{\mu_i}{\sigma_i}$ was again analyzed at the central transversal slice for all inserts, and the background as a function of the compression $2^n$. Furthermore, the impact on the spatial resolution was analyzed by extracting profiles along the 1 mm hole line and the 2 mm hole line for each $n$. The results are shown in figures 6.6 and 6.7. The curves show the

---

[3]For a non-ideal imaging geometry this assumption may be given only approximately because the rotation axis might not be exactly parallel to v-axis at all projections.
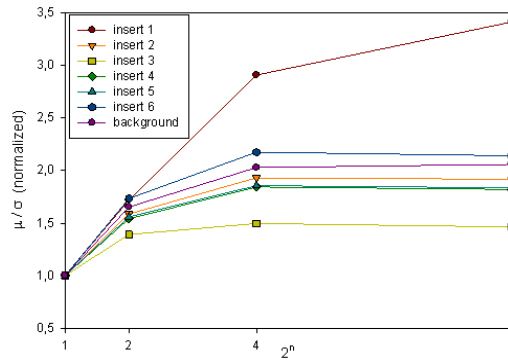
Figure 6.6: Projection compression dependence of noise ratio

*The increment of $\frac{\mu}{\sigma}$ up to $n = 2$ approximately coincides with the expected decrease of $\sigma$ that is caused by averaging, which approximately corresponds to a dose increment for small area of averaged pixels. The deviating increment of the curve representing insert 1 is caused by the blurring of existing inhomogeneities due to decreased spatial resolution.*
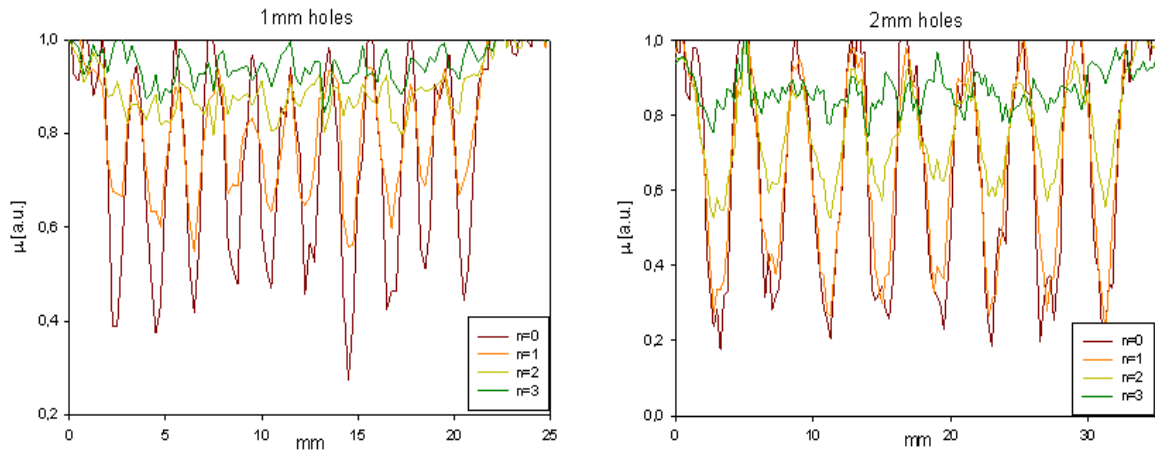


Figure 6.7: Spatial resolution of CBCTs from rebinned projections

*The plots show profiles along the serially arranged 1 mm and 2 mm holes of the contrast phantom for the reconstruction of differently rebinned projections. The background is normalized to $\mu_b = 1$. The holes contain air and would ideally have a value of $\mu_h = 0$. While the curves representing $n = 0$ and $n = 1$, respectively, show a good resolution of both hole lines, the small holes for $n = 2$ and $n = 3$ can hardly be distinguished.*

expected noise reduction up to $n = 2$. Also, the magnitude complies to the expected approximate proportionality to $2^{\frac{n}{2}}$ according to the estimated dose dependence of $\sigma$. The additional artifacts appearing at $n = 3$ cause an increment of $\sigma$ resulting in decreased values of $\frac{\mu}{\sigma}$. The $\mu$-profiles along the hole lines approximately reflect the normalized MTF values (MTF$(0) = 1$) at $0.25 \, \text{mm}^{-1}$ (2 mm holes, $\frac{1 \, \text{cycle}}{4 \, mm}$) and $1 \, \text{mm}^{-1}$ (1 mm holes) by $1 - \frac{\mu_h}{\mu_b}$ ($\mu_h$: reconstructed attenuation coefficient of the (air-)holes, $\mu_b$: reconstructed attenuation coefficient between the holes). Table 6.2 gives a summary of the eight roughly estimated MTF values extracted from figure 6.7. Summarizing the results about image noise and spatial resolution, $n = 1$ seems to be a good choice for projection rebinning of the given setup. A further application of $m = 1$ (rebinning in the v-direction) may further reduce noise without a significant decrease of spatial resolution. As already mentioned in section 4.4, the choice of $n$ and $m$ should also incorporate the choice of $p_x, p_y$ and $p_z$.

Table 6.2: Estimated CBCT-MTF values

|  | $n = 0$ | $n = 1$ | $n = 2$ | $n = 3$ |
|---|---|---|---|---|
| $MTF(0.25\,\text{mm}^{-1})$ | 0.8 | 0.7 | 0.35 | 0.05 |
| $MTF(0.5\,\text{mm}^{-1})$ | 0.6 | 0.35 | 0.05 | 0 |

*The values are roughly estimated from the profiles along the hole lines. The background is normalized to $\mu = 1$. The ideal value of $\mu_h$ is assumed to be 0.*

### 6.1.4 Impact of angular spacing for 4D-CBCTs

CBCT acquisition at a low angular resolution causes streak artifacts in the reconstructed images. These are already clearly visible at an angular spacing of $\Delta\Theta = 2°$, as can be seen in the example of the contrast phantom in figure 4.15. Therefore, the system developed so far only supports CBCT acquisitions with an angular spacing of 0.5° and 1.0°. However, lower angular resolutions may be of interest for 4D-CBCT acquisition of a certain breathing phase. Assuming a patient to breath regularly at a frequency $\nu$, with a breathing phase triggered acquisition during a full gantry rotation with constant speed $v$, the CBCT sequence consists of $360° \cdot \frac{\nu}{v}$ equidistantly spaced projections with an angular spacing of $\Delta\Theta = \frac{v}{\nu}$. Assuming, furthermore, a constant imaging dose per projection, the image quality is expected to decrease with decreasing number of projections because of higher noise due to lower total dose and stronger streak artifacts, due to lower angular resolution. To simulate such CBCT sequences, a full scan of the motionless lung phantom was acquired with an angular spacing of $\Delta\Theta = 0.5°$ and a total imaging dose of approximately $36\,\text{mGy}$ (other parameters: $n = m = 1$, $p_x = p_y = 0.5\,\text{mm}$, no additional filtration). Reconstructions were performed using different numbers of equidistantly spaced projections out of the complete sequence. Ten different angular spacings between 0.5° and 30° were chosen. Therefore, sequences between 12 and 720 projections according to imaging doses between $0.6\,\text{mGy}$ and $60\,\text{mGy}$ were reconstructed. Figure 6.8 shows an example of a transversal slice of the reconstruction applying angular spacings of 3° and 12°, respectively. The right image could, for instance, represent a possible 4D-CBCT
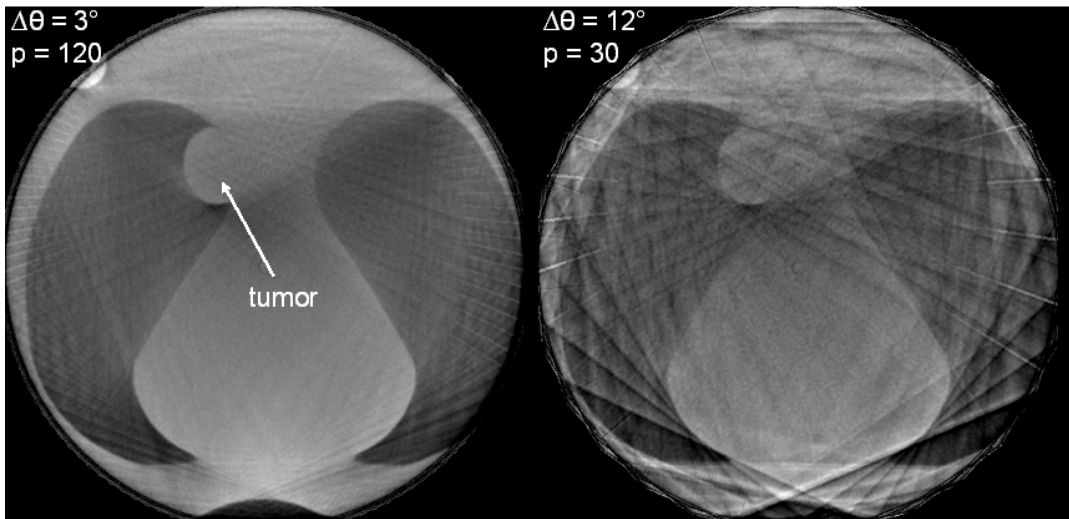


Figure 6.8: Streak artifacts of different angular spacings

*The lung phantom was scanned with a limited FOV (centered detector geometry). Therefore, only a circular part of it is visible at the reconstructions. Applying angular spacings of 3° already leads to visible streak artifacts but the reconstruction of only 30 projections still allows to distinguish between tumor and lung tissue.*

scenario with the realistic parameters $\nu = 10 \, \mathrm{min}^{-1}$ and $v = \frac{120°}{\mathrm{min}}$. The strong streak artifacts still allow a clear delineation of the tumor volume. To analyze the image quality and to possibility to distinguish between tumor and lung tissue as a function of the number of projections, the CNR between the tumor volume at the shown slice and the surrounding lung tissue was determined as discussed in section 6.1.1. The corresponding plot is shown in figure 6.9.



*CNR depending on the number of equidistantly spaced projections used for the reconstruction. The solid line represents an exponential fit to the data. The number of projections is approximately proportional to the total imaging dose.*
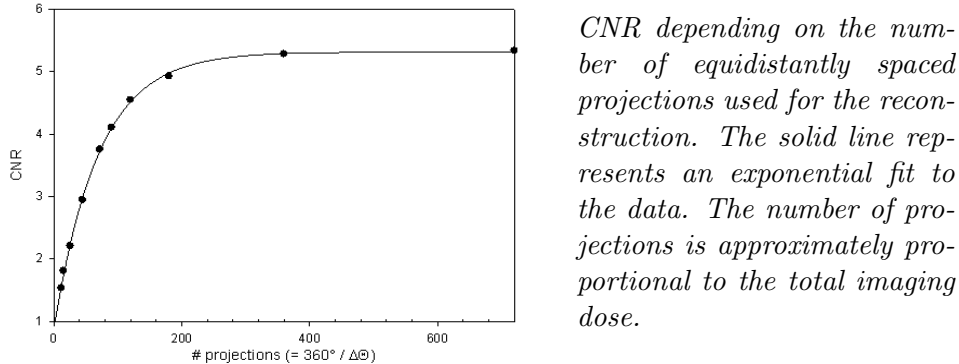
Figure 6.9: 4D-CBCT CNR as a function of breathing cycles

In this case, the ratio is described in the range from 12 to 720 projections ($\Delta\Theta = 0.5° \ldots 30°$) by

$$\mathrm{CNR} \approx 0.875 + 4.440 \cdot [1 - \exp(-0.0143 \cdot p)] \tag{6.1}$$

Sequences of fewer projections result in more and more unusable reconstructions. The CNR only rises to certain maximum value despite increasing imaging dose and angular resolution. This is due to the inhomogeneities of the lung tissue equivalent material, and also due to imaging artifacts caused, for instance, by scattered radiation and phantom truncation; the noise cannot be completely eliminated in the CBCT reconstructions. The maximum value is already nearly reached at an angular spacing of 1°.

For 4D-CBCT acquisitions of lung cases, realistic numbers of breathing cycles range between approximately 10 and 60, depending on gantry speed and breathing frequency. Actually, not just one projection but a bundle of neighbored projections, is used per breathing cycle for a pseudo-static reconstruction of a certain range of breathing amplitudes or phases; this results in higher imaging doses, but possibly at the expense of motion artifacts. If neither the inhale nor the exhale phase is included in that range, two (in general, not equidistantly spaced) projection bundles might be used for a reconstruction per breathing cycle, resulting in a higher angular resolution, but usually also at the expense of either imaging dose or motion artifacts due to the higher breathing velocities apart from the turning points of the respiration cycle [79], [80].

## 6.2   Clinical applications

During the development process, the current setup of the imaging system was transferred four times to a clinically used linac to perform several imaging and treatment applications on 19 patients. The four clinical runs are summarized in table 6.3. For any clinical run special permission

Table 6.3: Clinical applications of the imaging system

| run | date | patients | cases | applications |
|-----|------|----------|-------|--------------|
| # 1 | 07/2004 | # 1 | 1 head & neck | kV-CBCT acquisition<br>off-line positioning control. |
| # 2 | 09/2004 | # 2 – # 7 | 1 head & neck<br>3 prostate<br>1 lung | kV-CBCT acquisition,<br>off-line positioning control. |
| # 3 | 03/2005 | # 8 – # 13 | 2 head & neck<br>3 prostate<br>1 lung | kV-CBCT acquisition,<br>4D-CBCT acquisition with RGS,<br>fluoroscopic kV-tracking of respiratory motion,<br>immediate positioning control (and correction) followed by dose delivery through FPI [81]. |
| # 4 | 10/2005 | # 14 – # 19 | 1 head & neck<br>2 prostate<br>2 lung<br>1 lumbar spine | as run # 3, plus:<br>FOV extension for prostate cases,<br>gated treatment of one lung case,<br>MV-beam tracking during treatment for entrance dosimetry purposes [82]. |

*The table summarizes all 19 patient applications of the four clinical runs with the described linac integrated imaging system.*

for the respective patient applications was granted by the authorities. In the following sections the latest run of patient applications (# 4) and their methods are considered in more detail [82].

### 6.2.1   Patients and methods of clinical run # 4

The characteristics of the patients from the forth clinical run, and special applications, are summarized in table 6.4.

For all patients, full scan CBCTs with an angular spacing of $\Delta\Theta = 0.5°$ yielding sequences of 720 projections. An antiscatter grid was used. No additional filtration was applied. If necessary, a target position correction by means of the CBCTs was performed before the start of the dose delivery. For all patients, the treatment beam shape and intensity was tracked by means of the FPI that was left inserted at the accessory tray of the linac during dose delivery.

A photo of the clinical setup, including covers at both the linac and the x-ray tube, is shown in figure 6.10.

Table 6.4: Patient characteristics

| Patient | diagnosis | treatment technique | special applications |
|---------|-----------|---------------------|----------------------|
| # 14 | lung cancer | stereotactic RT | 4D-CBCT, fluoroscopic respiration tracking, gated dose delivery. |
| # 15 | oropharyngeal cancer | IMRT | |
| # 16 | prostate cancer | IMRT | FOV extension |
| # 17 | prostate cancer | IMRT | FOV extension |
| # 18 | unresectable chordoma | IMRT | 4D-CBCT |
| # 19 | soft tissue sarcoma | IMRT | |

*The table summarizes the patient characteristics and special applications other than MV-beam tracking and target position correction by means of CBCT acquisition.*



*The picture shows the setup of the imaging system for the clinical run #4 together with the fixation for the first patient. The experimental look of the system was disguised by linac and x-ray tube covers.*

Figure 6.10: Clinical setup of the imaging system

**Target position correction.** The workflow used for patient repositioning is illustrated in figure 6.11. A very accurate alignment of the calibration phantom for the geometrical calibration of the imaging system is performed prior to the CBCT acquisition to ensure that the axes of the patient coordinate system coincides with those of the room system, resulting in a transformation matrix according to equation 2.1 with $[x_0, y_0, z_0] = [0, 0, 0]$. This is required to precisely calculate the table shift for target position correction.

After the CBCT acquisition and reconstruction of the patient at the intended treatment position, and the matching of the image data with the diagnostic planning CT, the registration of the two data sets is approved by a visual comparison of different bony landmarks within both image sets. With the information now available, the error in the location of the radiation target can be calculated. In this procedure, the radiation target is treated as a rigid body, i. e. its new position in space is determined by a rigid transformation with six degrees of freedom consisting of a 3-dimensional spatial translation and the 3 Euler-rotations of the target around its respective axis through the isocenter. Deformations of the target were not accounted for. Only the target translations could be used for the target positioning process, in which the determined translation vector of the target
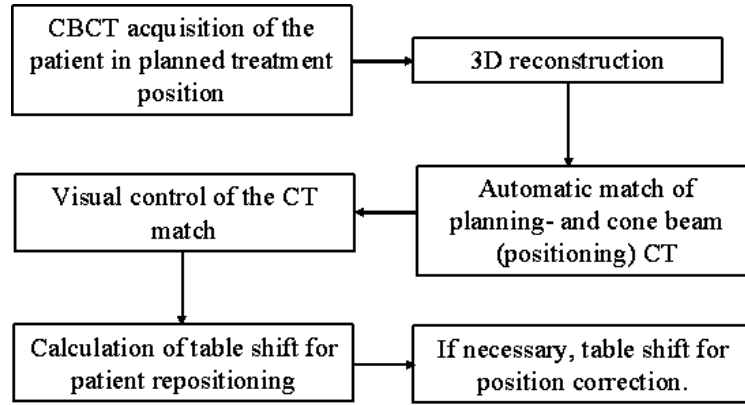
```
┌─────────────────────────┐          ┌─────────────────────────┐
│   CBCT acquisition of the│          │                         │
│ patient in planned treatment│──────▶│    3D reconstruction     │
│        position          │          │                         │
└─────────────────────────┘          └─────────────────────────┘
                                                   │
                                                   ▼
┌─────────────────────────┐          ┌─────────────────────────┐
│                         │          │   Automatic match of     │
│  Visual control of the CT│◀────────│ planning- and cone beam  │
│        match            │          │   (positioning) CT       │
└─────────────────────────┘          └─────────────────────────┘
            │
            ▼
┌─────────────────────────┐          ┌─────────────────────────┐
│ Calculation of table shift for│────▶│ If necessary, table shift for│
│  patient repositioning  │          │  position correction.    │
└─────────────────────────┘          └─────────────────────────┘
```

Figure 6.11: Workflow for patient positioning

*Position control and, if necessary, correction, was performed for all patients. The CBCT acquired in the attended automatically matched with the planning CT by means of a mutual information algorithm. The match is visually validated by a physician. If necessary, the calculated table shift is executed by the RTT for target position correction.*

is converted to a respective shift of the treatment table. The shift was executed manually by the responsible RTT.

Since the current treatment couch is only capable of performing a translation along the three main axes any rotation calculated for target position correction was ignored if the rotation angles for all three room axes were smaller than 2 degrees. Otherwise, the patient must be repositioned and the process starts over again with the acquisition of a new 3D image data set. Fortunately, for all evaluated cases this threshold of 2 degree rotations was not violated. For the translations, an action level of 2 mm for each component of the translation vector was defined. Only if the offset-components were larger than the action level, was the patient shifted to the new treatment position.

**FOV extension.** To cover the whole lateral extent of the patients during CBCT acquisition, a FOV extension by a FPI shift in the u-direction of 14 cm, resulting in a maximum FOV at the isocenter of approximately 48 cm, was performed for patients #16 and #17. To adjust the kV-beam to the changed FPI position, the x-ray tube was slightly tilted along its cathode-anode axis (the y-axis of the room system) in a way that the central ray approximately hit the center of the FPI's active area. The beam was collimated to cover nearly the whole active area. A safety margin of about 1 cm was applied at all edges to ensure the protection of the FPI electronics, resulting in a slightly reduced maximum FOV. The process of geometrical calibration of this setup, and the target volume positioning control and correction occur in an analogous manner as for the centered FPI geometry. Particulars concerning the FOV extension, especially the reconstruction of the CBCT sequences, are discussed in more detail in [43].

**4D-CBCT acquisition.** The acquisition of the 4D-CBCT sequences is performed by means of the RGS *AZ-733V*, as described in section 5.5. The belt of this system was fixed to the upper abdominal regions of patients #14 and #18 by the responsible RTT to measure pressure changes at the sensor caused by the expansion of the thorax and the abdomen. To each projection of the acquired CBCT sequence, a certain pressure value could be associated by means of the respective time stamps. These data were used for off-line determinations of the correlation between the surrogate (pressure signal) and the actual organ motion (diaphragm position), and for off-line reconstructions of arbitrary motion amplitude ranges. These methods are discussed in more detail in [68], [67]. The patient positioning was applied on the basis of the complete CBCT sequence independent belt signal. The RGS belt was not removed until the end of the treatment fraction.

**Fluoroscopic motion tracking.** Prior to the application of two different treatment fields, fluoroscopic kV-sequences of patient #14 were acquired at the corresponding gantry angle for several breathing cycles. These sequences were also used to determinate the correlation of motion and pressure signal, and for the determination of the actual tumor motion amplitude. Furthermore, static fluoroscopic sequences (see section 5.5) were acquired, triggered by the rising gating signal of the RGS at a certain breathing phase. These sequences can provide an indication of the stability of the signal-to-motion correlation.

**Gated dose delivery.** For patient #14, a diagnostic 4D (fan beam-)CT, in addition to the conventional treatment planning, was acquired. The movement of the tumor was analyzed by a physician and a treatment plan was created following the existing planning protocol. For gated dose delivery, the gating signal of the RGS was adjusted to release the treatment beam only at breathing phases corresponding to a pressure signal of less than 40 % of a previously determined threshold, representing the inhale phase of a typical breathing cycle of the treated patient. Due to the MV-beam gating, the total treatment time increased to about 16 minutes which is approximately 50 % longer than in the case without the gating [70].

**MV beam tracking.** The entrance fluence of the treatment beam was measured with the FPI for all patients during the complete dose delivery process. The field size at the FPI plane is scaled by factor a of $\frac{58\,cm}{100\,cm}$ at both dimensions with respect to the nominal field size according to the isocenter plane. The maximum field size of $40 \times 40\,\text{cm}^2$ is therefore completely covered by the active area at the centered FPI. For patients #16 and #17, the FPI was operated in its shifted position for kV-FOV extension. In order to spare the electronics of the FPI, it to had be ensured that the treatment beam did not exceed the active area at any time.

For MV-beam tracking, the FPI runs in free running mode at the highest saturation charge, and the gray values of every frame are recorded during the beam-on phases (RO signal = HIGH), summed up and stored to hard disk for each treatment segment separately. Summing up the data of the segments belonging to a certain treatment field yields a matrix that can be converted into the actual delivered primary input fluence. For this purpose, several corrections based on detector response and beam profile calibrations and a deconvolution with an empirically derived scatter kernel for the elimination of head scatter effects and optical scattering within the detector must be performed. These methods are described in more detail at [45]. For *entrance dosimetry* the derived fluence maps of each treatment field are fed into the dose calculation algorithm of the treatment planning system (TPS) to calculate the actual delivered dose distributions of the respective treatment fraction. Those calculations were performed off-line for all patients of this clinical run.

The described method for fraction-wise calculations of delivered dose distributions by means of entrance dosimetry assumes either unchanged patient anatomies during the whole treatment course when performing dose calculations on the basis of the anatomical snapshot of the planning CT, or requires the ability of performing dose calculations on the CBCT acquired at the corresponding treatment fraction. Dose calculations on CBCTs are discussed in section 6.3.

For the MV-beam tracking it was necessary to irradiate the patients such, that the beam transverses the FPI. To adapt the treatment plans to this special situation of this single treatment fraction the MUs of every segment were scaled by a previously determined factor of 1.205 (see section 5.7.3). The agreement of the dose distributions resulting from the adapted treatment plans with those described by the treatment planner were carefully verified by phantom measurements.

### 6.2.2 Results of the clinical run

In the following, some results and experiences obtained from the different applications of the descried clinical run are summarized.

**Target position correction.** Bony landmarks were easily detected and a table shift for correction of the setup-deviation could be automatically calculated in all cases. The image quality was sufficient for verifying the required table shift by comparison of the desired target point with the isocenter visible on the CBCT. To offer an impression of the CBCT image qualities, figure 6.12 and 6.13 show examples of CT data for transversal slices of patients # 15 (centered FPI geometry) and # 16 (extended FOV). Besides the bony landmarks, also a good soft tissue contrast was achieved. This can, for instance, be seen in figure 6.12b, where the optical nerves of the patient are visible in the CBCT reconstruction.
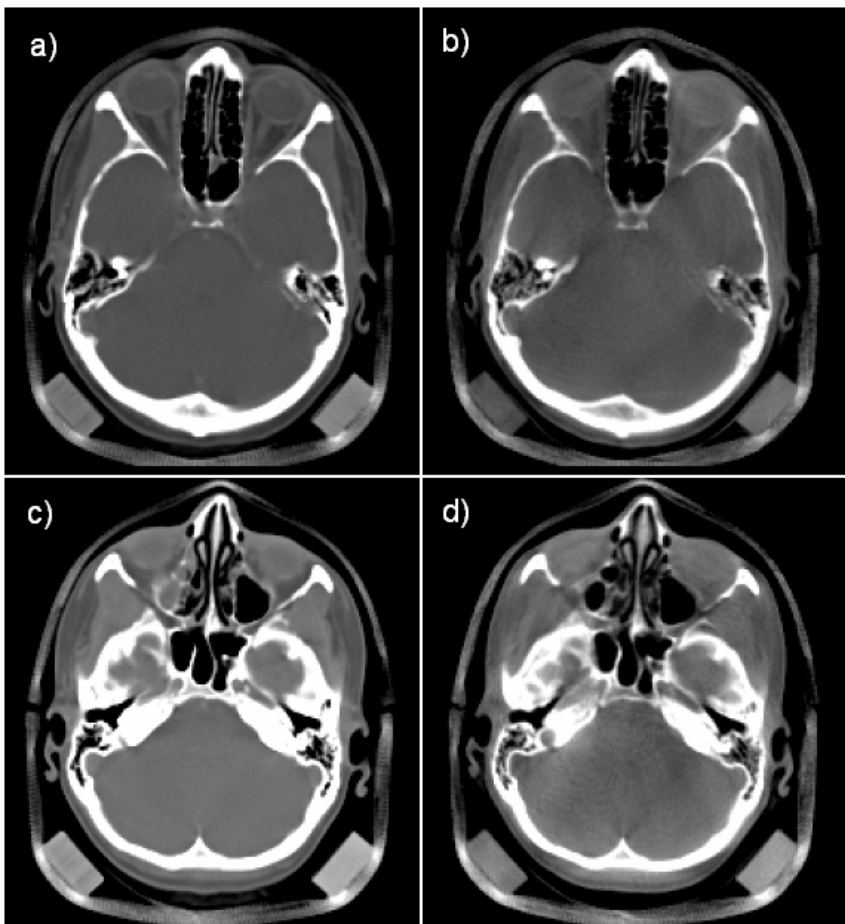


*The left panels a) and c) show transversal slices of the planning CT; the right panels show the corresponding slices of the CBCT. The CBCT was initially reconstructed with $p_x = p_y = 0.5\,mm$ and re-scaled by the image registration process to the pixel sizes of the planning CT ($p_x = p_y \approx 1\,mm$). The CBCT reconstruction corresponds to an estimated imaging dose of approximately $25\,mGy$. Both slices show a good image quality of the CBCT. Especially the visibility of the optic nerves at panel b) indicate a good soft tissue contrast.*

Figure 6.12: Transversal slices of patient # 15
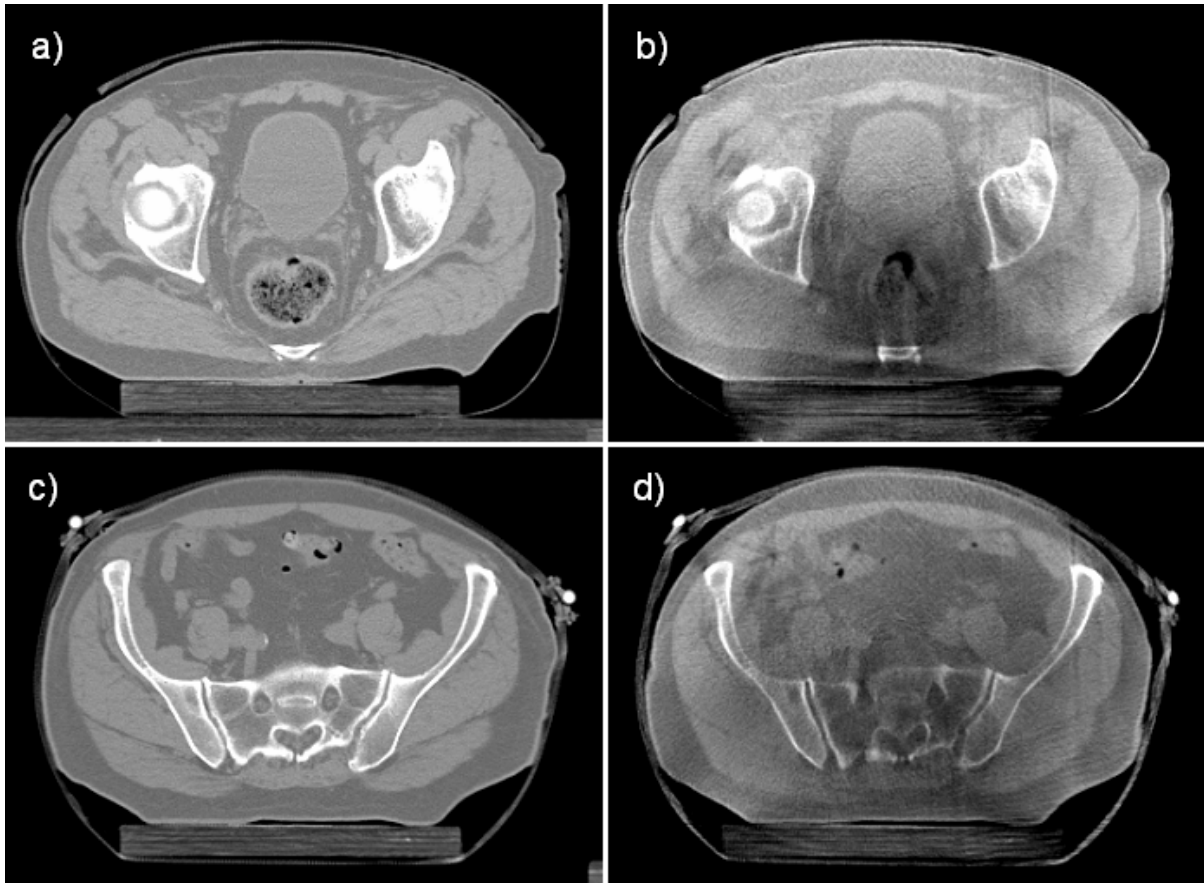
Figure 6.13: Transversal slices of patient #16

*The left panels a) and c) show transversal slices of the planning CT; the right panels show the corresponding slices of the CBCT. The CBCT was initially reconstructed with $p_x = p_y = 0.78\,mm$ and re-scaled by the image registration process to the pixel sizes of the planning CT ($p_x = p_y \approx 1\,mm$). The CBCT reconstruction corresponds to an estimated imaging dose of approximately $30\,mGy$. The CBCT was acquired with a FOV extension. Higher ratios of scattered radiation produced in the abdomen compared to the example of figure 6.12 cause cupping artifacts at the CBCT. A low primary signal at the FPI due to higher beam attenuations results in noisier images. Nevertheless, the CBCT image quality is still sufficient to detect certain soft tissue structures.*

The detected maximum setup-deviation of all patients was 6 mm (table 6.5). Due to a defined action level of 2 mm, a target point correction was carried out in 4 cases.

The additional workload of the described workflow compared to a normal treatment fraction led on average, to an extra time of about 10 minutes. The time interval from the start of the CBCT acquisition to the beginning of the dose delivery was divided into the required time for: i) CBCT acquisition, ii) CBCT reconstruction, iii) image registration, and iv) setup evaluation (and correction). The itemized time intervals for each patient are given in [82].

Table 6.5: Setup deviations evaluated with CBCT

| Patient | latero-lateral shift [mm] | ventro-dorsal shift [mm] | cranio-caudal shift [mm] | max. rotation | target point correction |
|---------|---------------------------|--------------------------|--------------------------|---------------|-------------------------|
| # 14 | 3.1 | 0.1 | 6.0 | 0° | yes |
| # 15 | -0.6 | 0.5 | -0.7 | 0.6° | no |
| # 16 | -0.7 | -1.2 | 2.3 | 0.7° | yes |
| # 17 | 1.2 | 3.6 | 0.1 | 1.1° | yes |
| # 18 | 0.3 | 0.1 | 0.1 | 0.0° | no |
| # 19 | -2.6 | -1.7 | -1.7 | 1.5° | yes |

*According to an action level of 2 mm, target point corrections were performed for four out of the six patients by an according table shift. The maximum evaluated rotations stayed below 2° and therefore did not induce any correction.*

**4D-CBCT.** A projection-wise breathing phase and amplitude mapping of the CBCT sequences of patients # 14 and # 18 was possible by means of data from the RGS. These datasets could be reconstructed for arbitrary breathing phases or amplitude ranges. Figure 6.14 shows a selected frontal slice of patient # 14 reconstructed using all 720 projections, as well as only those associated with a certain amplitude range of the exhale and inhale phase, respectively. The angular spacing,
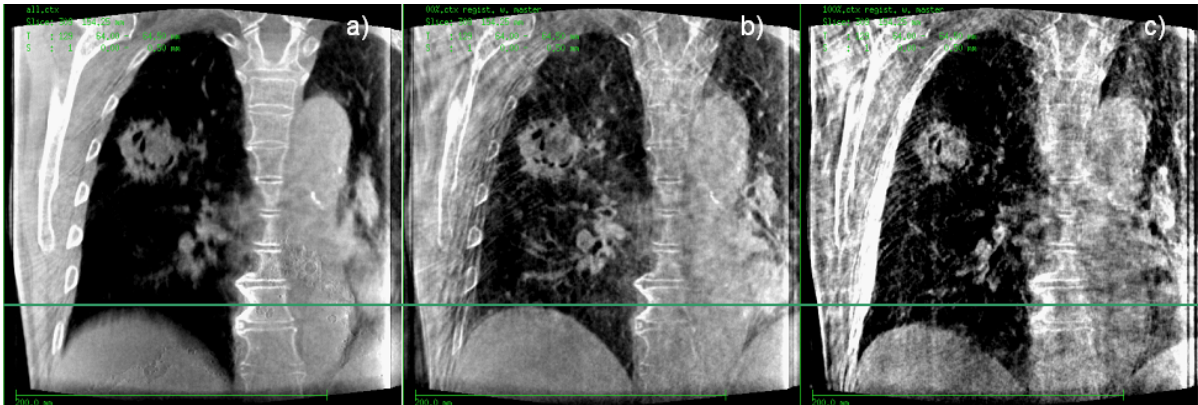


Figure 6.14: CBCT reconstructions of a 4D-CBCT data-set

*The pictures show a frontal slice of patient # 14 using a) all acquired projections, b) projections around the exhale phase (68 projections) and c) around the inhale phase (166 projections). The horizontal green line is for illustration purposes and indicates the CC position of the diaphragm at the exhale phase. The image quality reduces with decreasing number of projections used for reconstruction due to higher noise ratios. Nevertheless, the static reconstructions are still appropriate for 4D image registration purposes and the evaluation of tumor organ motions.*

and therefore also the number of projection bundles used for the inhale and exhale reconstructions, are comparable (approximately 30). Nevertheless, the inhale reconstruction shows noisier images of poorer quality. This is because the total number of used projections is lower due to higher respiration-caused velocities at the exhale phase.
In the non-static reconstruction, especially at the edge of the diaphragm, the effect of blurring due to the movement can be easily shown. This blurring is significantly reduced in the static reconstructions. Furthermore the different positions of the diaphragm for both phases are evident. If a 4D CT data set is acquired beforehand to generate a treatment plan for a gated dose delivery approach, a CBCT reconstruction at the same respiration phase can be used to calculate a potential

displacement of the patient for a repositioning of the patient. Using a mutual information matching algorithm, it is also possible to quantify the maximum tumor motion between the inhale and exhale position, if 3D data sets for both phases are available. If a gated dose delivery approach with a predefined gating threshold is scheduled, it is also possible to use the minimum and maximum phase within the given threshold for the reconstruction. So it is possible to estimate the movement of the tumor within the gating window to adjust the margins around the target volume.

The fluoroscopic sequences could also be used to evaluate the tumor motion and to check the correlation between the signal of the RGS and respiratory caused motion. The 'static fluoroscopy' sequences delivered images of a defined breathing phase, free from respiratory motion. Only different phases of the heart beat were distinguishable between the single projections. This indicated a good stability of the pressure-to-motion correlation.

**MV beam tracking.** The cumulative FPI gray values produced by the primary fluence of the treatment beam were stored separately for each treatment segment. Figure 6.15 shows an example of the cumulative signal produced during the delivery of two different treatment beams of patient # 15. As expected, the shapes and intensity levels coincide with the specification of the treatment
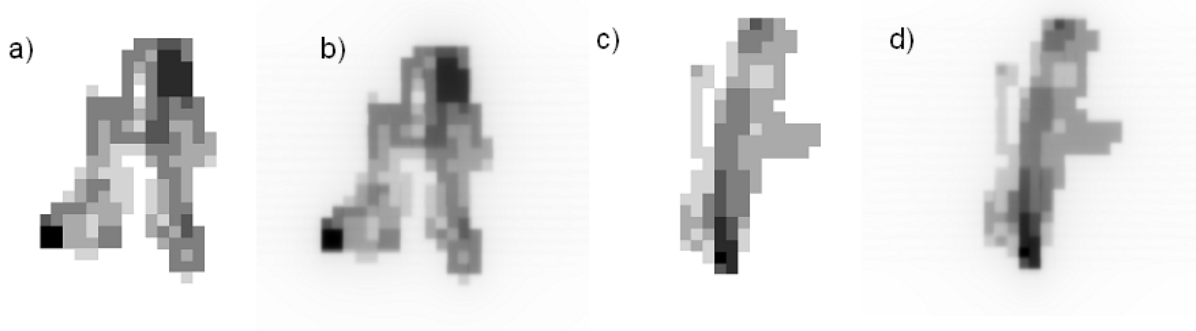


Figure 6.15: Measured and calculated primary fluence

*Panels a) and c) show the fluence matrices created by the TPS and used for dose calculation of two treatment beams consisting of 12 and 7 segments , respectively. Panels b) and d) show the corresponding FPI measurements. Darker areas indicate higher fluences.*

plan. Corrections and deconvolutions of the measured signals were carried out in order to obtain the fluence matrices needed for the dose calculation. The realization and results of the entrance dosimetry investigations on the planning CTs of the treated patients are described in [45], [28].

## 6.3   Dose calculations on CBCTs

First investigations of how to switch from pure image guided RT towards dose guided RT with the Inline concept have already been described in the last section with the introduction of the methods of entrance dosimetry. However, due to interfractional anatomical changes like loss or gain of weight, tumor regression, fill level of the bladder, etc., the actually delivered dose distribution may differ from the calculation that is based on the planning CT. Such uncertainties may be avoided if an accurate dose calculation on the CBCT acquired for patient positioning prior to the dose delivery of the respective treatment fraction is possible. In the following sections the accuracy of dose calculations on CBCTs is discussed [83], [84].

### 6.3.1   Motivation

Photon dose calculations are based on the electron density distribution of the irradiated material or tissue. This information is indirectly provided by the CT cube in terms of attenuation coefficients or HUs that are translated to electron densities by means of a CT scanner specific conversion function [85], [86].

Higher scatter ratios in the wide field projections of CBCTs cause cupping artifacts at the reconstructions [87]. This may result in a spatial dependency of the reconstructed attenuation coefficients, as illustrated in figure 6.16. The profile through the central transversal slice of the reconstruction of a cylindrical water-filled perspex phantom with a diameter of 18 cm shows a cupping of approximately 4 %.[4]



*The plot shows the profile along the black line of the reconstruction of the cylindrical water phantom. The two small circles are cylindrical holes through the phantom that are partly filled with perspex sticks. The treatment table was outside the FOV during CBCT acquisition.*
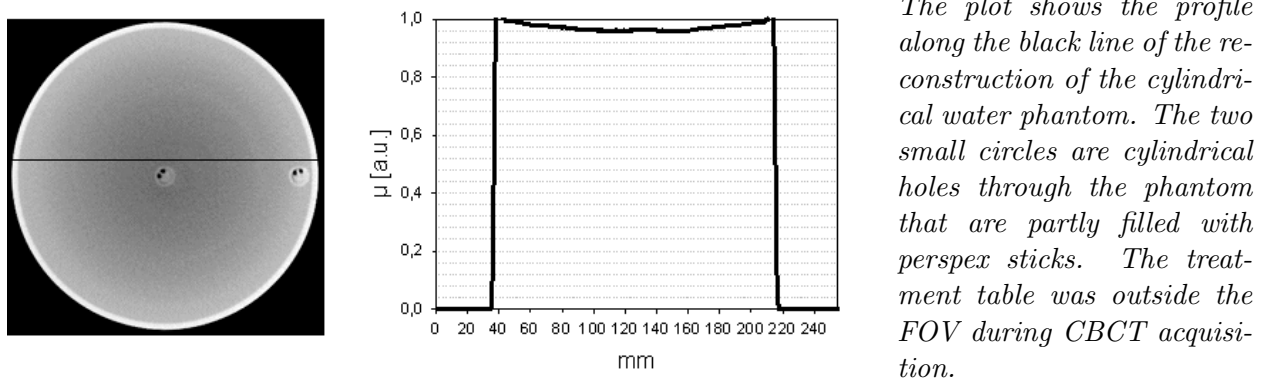
Figure 6.16: Cupping at the water phantom

Figure 6.17 gives an example of a typical HU to electron density conversion and a HU histogram of a head and neck CT from a diagnostic CT scanner. Most of the voxels are represented by HUs around 0. In this range, the conversion function has a smooth gradient. Therefore, slight inaccuracies of the HUs may only have a low impact on the electron density distribution and still allow a sufficiently accurate dose calculation, despite scatter artifacts such as those shown for a water phantom in figure 6.16.

In the following sections, it is shown, that for small phantoms and head and neck patients HUs can be reconstructed with a an accuracy that is sufficient for dose calculation purposes. This is no longer the case for larger phantoms and extra-cranial patients due to higher scatter distributions. Therefore both cases are analyzed separately.

---

[4]All CBCTs dealt with in section 6.3 and its subsections are acquired with antiscatter grid.
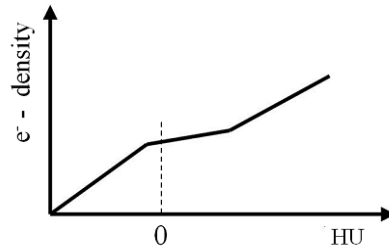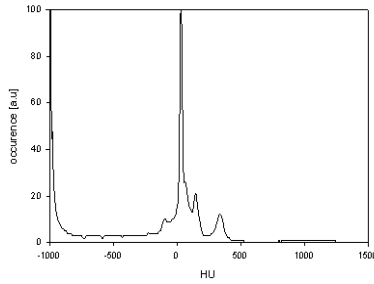
*The left plot shows the distribution of HUs at a diagnostic head and neck CT. The graph in the right gives an example of a typical HU to electron density conversion.*

Figure 6.17: HU histogram & electron density conversion

### 6.3.2 Small phantoms and head and neck patients

When head and neck (CB)CTs are acquired the treatment table is outside the FOV. The patient's head is fixed with a head mask, as can be seen in figure 6.10. All phantoms discussed in this section are fixed similarly; i. e. the treatment table is always outside the FOV.

To perform dose calculations on CBCTs of head and neck cases, or phantoms of a similar size as the water phantom, a HU to electron density conversion function was generated by means of the inlays of the already introduced contrast phantom. For the calculation of HUs (see equation 2.17), the mean value of the profile through the water phantom was used as $\mu_w$. Table 6.6 lists the HUs of the contrast phantom extracted from a CBCT reconstruction. Along with the electron densities

Table 6.6: CBCT HUs of the contrast phantom

| insert | 1 | 2 | 3 | 4 | 5 | 6 | bg |
|---|---|---|---|---|---|---|---|
| H | $-699 \pm 82$ | $125 \pm 37$ | $1354 \pm 80$ | $327 \pm 39$ | $-969 \pm 36$ | $-81 \pm 31$ | $47 \pm 31$ |

*Mean HUs and standard deviations of the 3 cm inlays of the contrast phantom extracted from the central slice of a CBCT reconstruction of the contrast phantom. Only the mean values are used for HU to electron density conversion.*

listed in table 6.1, these values were used to generate the conversion function. Interim values were calculated by linear interpolation between the neighboring values from the table.

Dose calculations were performed of CBCTs of the water phantom, the contrast phantom, the head phantom and on the data set of patient # 15.

For comparison purposes, reference CT data sets of the phantoms were acquired using a diagnostic FBCT. Artificial contours were defined for IMRT optimization[5] and dose volume histogram (DVH) comparison. The CBCT data cubes were spatially matched to their reference cubes. Treatment plans were created and dose calculations with a clinically approved pencil beam algorithm [89] were performed for identical treatment plans on the reference CT and the matched CBCT cube.

For the patient case, the original contours defined by the physician were used on the planning CT and on the CBCT that had already been matched to the planning CT for positioning purposes. For dose calculation the original treatment plans were used. Since CBCTs of patients acquired before treatment fractions are usually used for positioning purposes, dose calculations of the applied radiation sequence on the matched CBCT cube should, aside from intra-fractional organ movements (like breathing), correctly predict the dose distribution in the patient for the particular treatment fraction.

---

[5]IMRT optimization is done with a research version of KONRAD® [88].

Dose calculations using the reference CTs were done with the standard HU to electron density conversion also used in clinical routine. Dose calculations from CBCTs were performed using the adapted conversion obtained from the contrast phantom.

**Water phantom.** To estimate the influence of the remaining cupping on small phantoms on dose calculation accuracy, a depth dose curve from one incident $5 \times 5\,cm^2$ beam and the dose distribution of three equiangular spaced $5 \times 5\,cm^2$ beams in the water phantom were calculated. The differences between the reference CT and the CBCT stay below $2\,\%$ in the profiles shown in figure 6.18. This emphasizes the insensitivity of small HU inaccuracies in the soft tissue range.
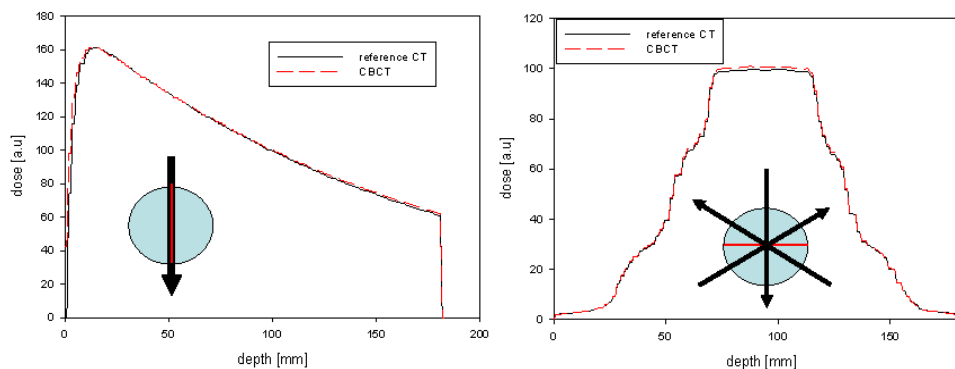


Figure 6.18: Water phantom – dose profiles

*Profiles through the water phantom of a one-field and a three-field plan dose distribution. The black arrows symbolize the beam configuration; the profiles were measured along the straight red line through the water phantom.*

**Contrast phantom.** The dose distribution of a coplanar five-beam IMRT plan was calculated for the contrast phantom. A target volume and several OARs were defined. Figure 6.19a shows the central transversal slice of the reference CT with contours and the calculated dose distribution in this slice; figure 6.19b shows a DVH comparison of the reference CT and the CBCT. The DHVs of all contours are overlaid in one plot. The colors of the DVHs correspond to the contours of 6.19a. The pink DVH corresponds to an OAR that does not intersect the central slice. On the left side the DVHs of the OARs seem to coincide exactly; no differences are visible on the overlay. The differences between the single DVHs are plotted in figure 6.19d. Only slight differences are visible for the high dose area of the target volume. Additionally, a dose difference distribution of the central slice is shown in figure 6.19c. Local differences in the high dose area are visible but stay below $3\,\%$.

Figure 6.19: Contrast phantom – comparison of dose distributions
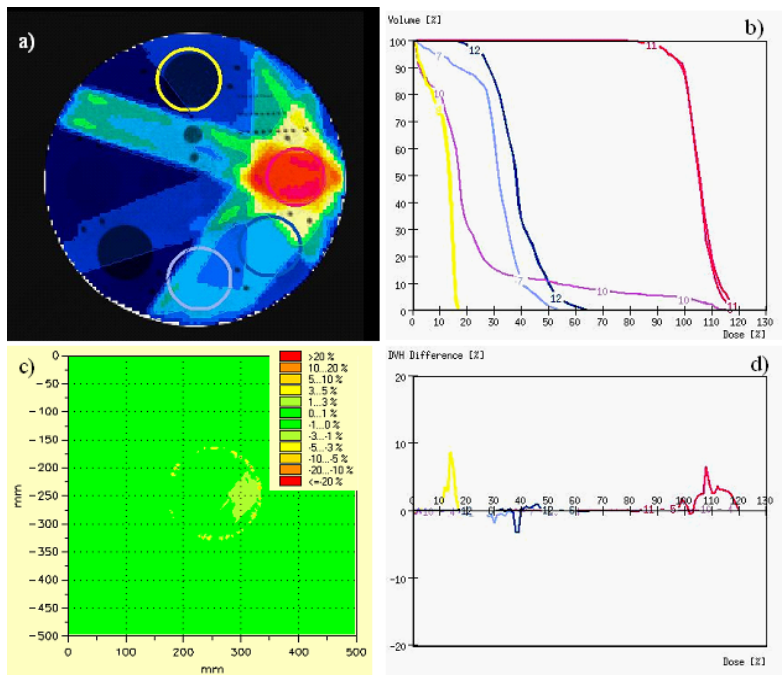
*Contrast phantom. a) Contours and reference CT dose distribution; b) DVH comparison; c) Dose difference distribution (local percentage difference); d) DVH difference (positive if a larger volume of the CBCT contour receives the according dose value).*

**Head phantom.** A similar analysis also with a coplanar five-beam IMRT plan was carried out on the head phantom. The results are shown in figure 6.20. Again, nearly no difference is visible between the DHVs and the dose distribution of the shown transversal slice. Observable differences in the dose distribution only occur at the border of the phantom. This may happen if there are small inaccuracies in the image match, but it does not affect any VOIs.
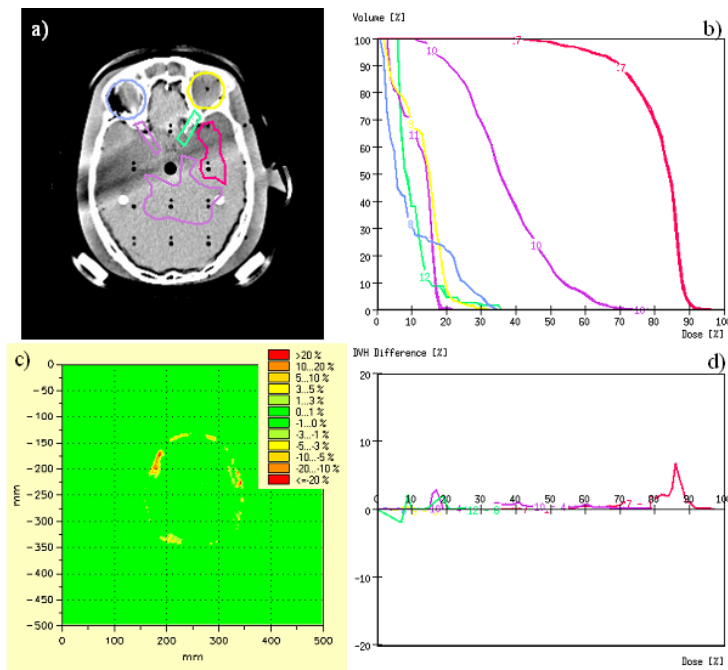


*Head phantom. A) Contours on a transversal slice. The dark stripe through the slice represents an air gap crossing the slice. This gap results from the fact that the phantom is assembled from different sloped slaps. B) DVH comparison; c) dose difference distribution (local percentage difference); d) DVH difference (positive if a larger volume of the CBCT contour receives the according dose value).*

Figure 6.20: Head phantom – comparison of dose distributions

**Patient.** The phantoms analyzed up to that point showed that an accurate dose calculation from CBCT for small objects without the treatment couch being placed within the imaging volume is feasible with a simple calibration method.

For the following clinical example (patient # 15), the CBCT was acquired in the last week of the treatment course. That means there was nearly one month between the planning CT and the CBCT acquisition. In between, a control CT of this patient with a diagnostic FBCT scanner was acquired which was also used for the analysis of the CBCT dose calculation accuracy. Figure 6.21 shows two transversal slices of the three matched CTs with different contours. On the upper slices
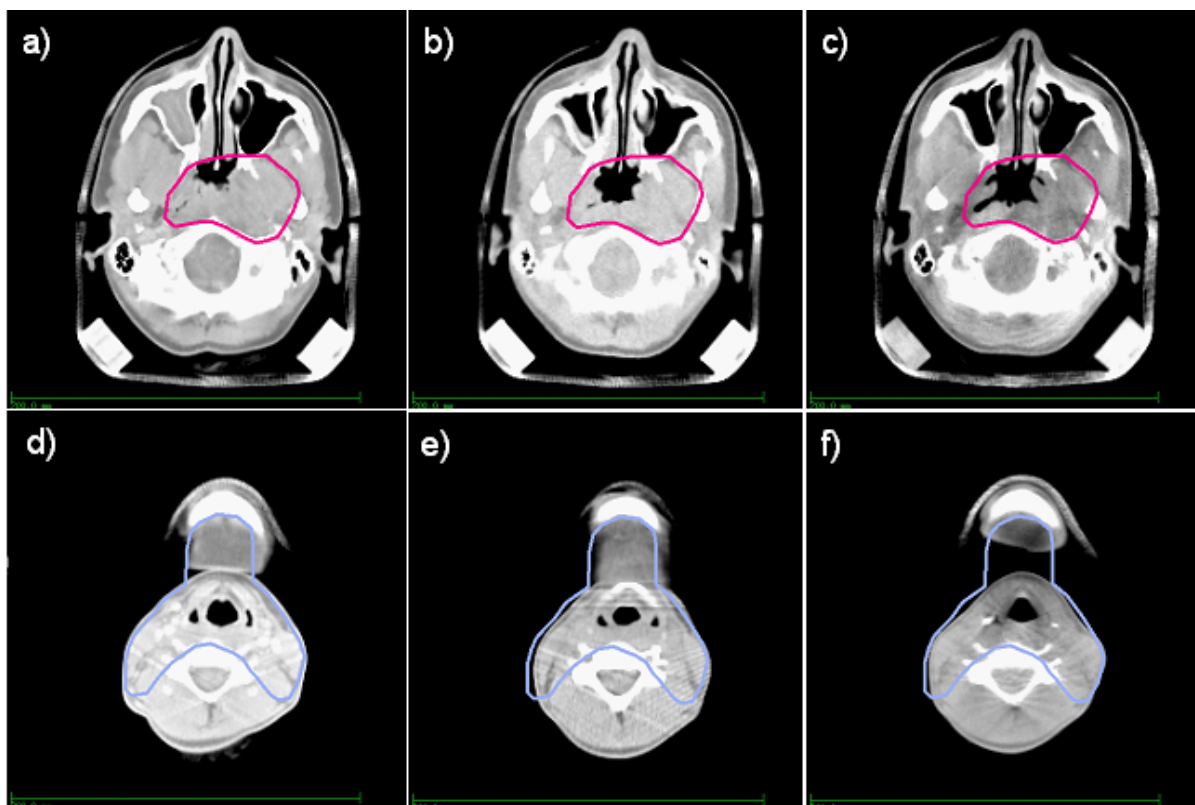


Figure 6.21: Patient # 15 – planning-, control- and CBCT

*Transversal slices of patient # 15 with a target volume contour and a planning contour, respectively. A), d) planning CT; b), e) control CT acquired with a diagnostic CT scanner at a late fraction of the treatment course; c), f) CBCT acquired at the end of the treatment course.*

a), b), and c) one can already see a tumor regression within the red target volume contour between the planning CT and the control CT, and even more between the planning CT and the CBCT. Furthermore, the right sinuses were plugged during the time of planning CT acquisition. The cold disappeared during the treatment course, and is visible neither on the control CT nor on the CBCT. The lower panels d), e), and f) show another transversal slice with a contour used for dose optimization purposes. On these slices the lower part of the patient's chin and the neck is visible. Due to loss of weight during the treatment course, a gradual reduction of tissue between the chin and neck is visible. The dose calculation from these three CTs was based on the original coplanar nine-beam IMRT treatment plan. In figure 6.22, DVH comparisons of both shown contours are plotted. Figure 6.22a shows the comparison between the planning CT and the control CT, and figure 6.22b shows the difference between the planning CT and the CBCT. All other contours are neglected for clarity, because they again, show nearly no visible differences in the DVHs.
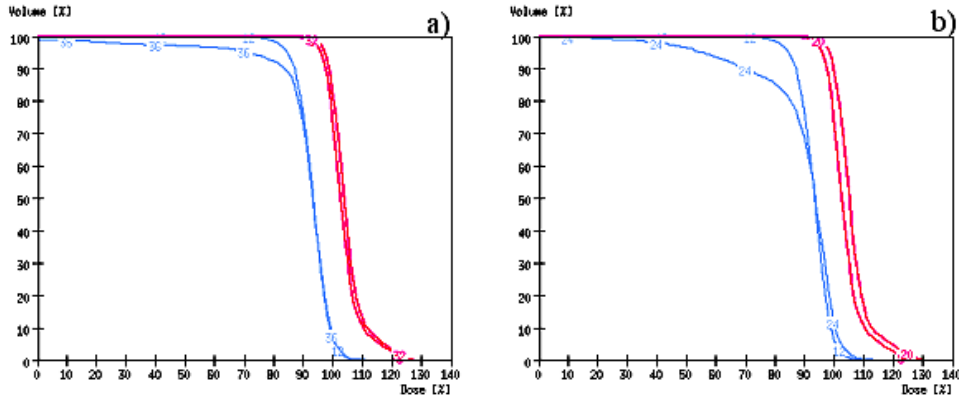
Figure 6.22: Patient # 15 – DVH comparison

*DHV comparison for the two shown VOIs of patient # 15. A) Comparison between planning CT and control CT dose distribution; b) comparison between planning CT and CBCT dose distribution. The curve labelled with number 12 belongs to the planning CT. For the target volume (red) in both cases the curve with the lower maximum dose belongs to planning CT.*

The trend of the DVHs from the planning CT to the control CT concerning the two shown contours increases for the CBCT. The target volume DVH shifts to higher calculated dose values due to lower radiological depths with progressive tumor regression. Increasing parts of the other contour receive lower doses due to missing tissue and missing build-up effect. The plugged sinuses have no impact on the dose calculation because there is no incident beam passing through this part of the patient. Due to its consistency with the expectation and the (not shown) good agreement with the other DVHs of the planning CT and the control CT, the dose distribution calculated from the CBCT can be assumed to be accurate.

### 6.3.3 Larger phantoms and extra-cranial cases

X-ray projections of larger objects, especially when they are placed on the treatment table, contain much more scattered radiation. Even with the use of an anti-scatter grid, the induced artifacts interfere to such an extent that an accurate dose calculation may no longer be possible from CBCTs. Cupping artifacts may dominate the images, and attenuation coefficients may have a strong spatial dependance. The plot in figure 6.23 shows profiles of reconstructed attenuation coefficients through a transversal slice of the abdominal part of a body phantom placed on the treatment couch and imaged with a diagnostic FBCT scanner, and the CBCT setup to illustrate this issue. In such cases (cupping up to 20 % despite the use of an anti-scatter grid), the dose calculation is no longer adapted to the CBCT data set as in the HU to electron density calibration method described above, but vice versa. Therefore, the following new method was tested for CBCT dose calculation using image information from the reference CT, and using the standard HU to electron density conversion of the diagnostic CT scanner:

At first, it is assumed that after the repositioning of the patient, all rigid objects such as the treatment couch and an optional base frame used for patient fixation, have the same coordinates as on the planning CT[6]. The patient's lowest point in the AP direction (i. e. the point with the lowest room z-coordinate[7].) is above the highest point of the base frame. HUs of the CBCT below the top side of the base frame are replaced by those from the reference CT, so that dose distributions

---

[6]After the registration of the CBCT with the reference CT, both CT cubes have the same voxel sizes and use the same patient coordinate system.

[7]With this section 'lower/higher points' mean points with a lower/higher z-coordinate of the room coordinate system
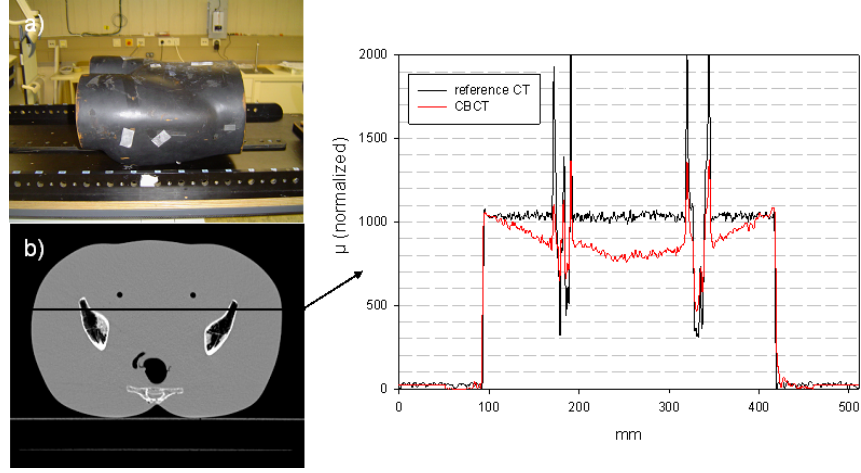
Figure 6.23: Body phantom – cupping at a CBCT reconstruction

*A) Abdominal part of a body phantom placed on the treatment couch. B) FBCT reconstruction of a transversal slice of the phantom. C) Normalized profiles of measured attenuation coefficients in the LR direction along the black line in b). The black curve showing a homogenous attenuation coefficient distribution corresponds to the FBCT, the black line showing a cupping of approximately 20 % to the CBCT reconstruction.*

of beams coming from below and passing through the treatment couch are calculated correctly within the replaced volume. The patient himself is not assumed to be rigid. Otherwise, there would be no reason to perform a dose calculation from the CBCT because the dose distribution would definitely coincide with the planned one. However, the patient's anatomy is assumed not to change significantly between the acquisition of the planning CT and the CBCT. Indeed, if only the planning CT is available, one must assume the patient's anatomy as static in order to get a cumulative dose distribution for the complete treatment course. Furthermore, it is assumed that higher values of reconstructed attenuation coefficients $\mu(x, y, z)$ represent higher electron densities $\varrho_e^-(x, y, z)$ within any sufficiently small cubic region of the CBCT ($\mu(x, y, z) > \mu(x', y', z') \Leftrightarrow \varrho_e^-(x, y, z) > \varrho_e^-(x', y', z') \, \forall \, [x, y, z], [x', y', z']$ within a sufficiently small cubic region). This relation is also globally fulfilled for the HUs of the reference CT and electron densities. On the basis of these assumptions, the volume of interest for the dose calculation is divided into (ideally, as few as possible and as many as necessary) quadratic cuboids having their axis parallel to the z-axis of the patient coordinate system. Then the attenuation coefficient histogram of each region is adapted to the HU histogram from the corresponding region of the reference CT. This is done in the following way:

Let each region contain $n$ serially numbered voxels. $H_i$ is the HU of voxel $i$ of the reference CT and $\mu_i$ the attenuation coefficient[8] of the corresponding voxel of the CBCT.
Let

$$f, g : [1, n] = \{m \in \mathbb{N} \mid 1 \leq m \leq n\} \rightarrow [1, n] \tag{6.2}$$

be two bijective mappings with

$$H_{f(i)} \leq H_{f(j)} \; \forall \, i, j \in [1, n] \text{ with } i \leq j \tag{6.3}$$

$$\mu_{g(i)} \leq \mu_{g(j)} \; \forall \, i, j \in [1, n] \text{ with } i \leq j \tag{6.4}$$

Furthermore, let

$$\mathcal{K} = \{k_1, k_2, \ldots, k_{m-1}\} \mid 1 \leq k_i \leq n \; \forall \, i \in [1, m - 1] \tag{6.5}$$

be a set of $m - 1$ natural numbers with

$$k_i - k_{i-1} = a \cdot n, \; 0 \leq a \leq 1, \; \forall \, i \text{ with } 2 \leq i \leq m - 1 \tag{6.6}$$

---

[8]Throughout this section attenuation coefficients are regarded to be of dimensionless quantity.

The ranges of both histograms $\big([H_{f(1)}, H_{f(n)}]$ and $[\mu_{g(1)}, \mu_{g(n)}]\big)$ are each divided into $m$ subsets $(3 \leq m \ll n)$:

$$
\mathcal{S}_{H,i} = \begin{cases} [H_1, H_{f(k_1)}] & , \text{ for } i = 1 \\ [H_{f(k_{i-1})}, H_{f(k_i)}] & , \text{ for } 2 \leq i \leq m-1 \\ [H_{f(k_{m-1})}, H_{f(n)}] & , \text{ for } i = m \end{cases} \tag{6.7}
$$

$$
\mathcal{S}_{\mu,i} = \begin{cases} [\mu_1, \mu_{g(k_1)}] & , \text{ for } i = 1 \\ [\mu_{g(k_{i-1})}, \mu_{g(k_i)}] & , \text{ for } 2 \leq i \leq m-1 \\ [\mu_{g(k_{m-1})}, \mu_{g(n)}] & , \text{ for } i = m \end{cases} \tag{6.8}
$$

That means the same number $(a \cdot n)$ of voxels belong to each subset, for example, 5-10 percent of all considered voxels. The first and the last subset (i.e. those including the voxels with the lowest and highest HUs or attenuation coefficients) may be an exception and contain fewer voxels.

Let

$$
\mathfrak{T}[\mu_1, \mu_n] = \{t_i\} : \begin{cases} \mathcal{S}_{\mu,1} \to [-1000, H_{f(k_1)}] & , \text{ for } i = 1 \\ \mathcal{S}_{\mu,i} \to \mathcal{S}_{H,i} & , \text{ for } 2 \leq i \leq m-1 \\ \mathcal{S}_{\mu,m} \to [H_{f(k_{m-1})}, 3000] & , \text{ for } i = m \end{cases} \tag{6.9}
$$

be a set of transformations with $\qquad t_i(\mu \in \mathcal{S}_{\mu,i}) =$

$$
\begin{cases} \max\left[-1000, \left(\mu - \frac{\mu_{g(k_2)} - \mu_{g(k_1)}}{2}\right) \cdot \frac{H_{f(k_2)} - H_{f(k_1)}}{\mu_{g(k_2)} - \mu_{g(k_1)}} + \frac{H_{f(k_2)} - H_{f(k_1)}}{2}\right] & \text{for } i = 1 \\ \left(\mu - \frac{\mu_{g(k_i)} - \mu_{g(k_{i-1})}}{2}\right) \cdot \frac{H_{f(k_i)} - H_{f(k_{i-1})}}{\mu_{g(k_i)} - \mu_{g(k_{i-1})}} + \frac{H_{f(k_i)} - H_{f(k_{i-1})}}{2} & \text{for } 2 \leq i \leq m-1 \\ \min\left[\left(\mu - \frac{\mu_{g(k_{m-1})} - \mu_{g(k_{m-2})}}{2}\right) \cdot \frac{H_{f(k_{m-1})} - H_{f(k_{m-2})}}{\mu_{g(k_{m-1})} - \mu_{g(k_{m-2})}} + \frac{H_{f(k_{m-1})} - H_{f(k_{m-2})}}{2}, 3000\right] & \text{for } i = m \end{cases}
$$
$$\tag{6.10}$$

Now, for each region of the CBCT, the attenuation coefficients histogram is adapted to the HU histogram of the corresponding region of the reference CT separately by a continuous, monotonically increasing transformation:

$$
\mathfrak{T} : \mu \to H^{\text{CBCT}} \mid H^{\text{CBCT}}(x, y, z) = \mathfrak{T}(\mu(x, y, z)) \tag{6.11}
$$

That means all subsets, except the first and the last one, of the CBCT are linearly transformed to their respective subsets of the reference CT. The first and the last subsets are transformed the same way as their neighboring subsets. Afterwards, the histograms of both the CBCT and the reference CT are similar, but not necessarily identical. To aid better understanding, the principle of the histogram adaptation is illustrated in figure 6.24.

Transforming the first and the last subset independently from their corresponding ones in the reference CT prevents noise from artificially increasing the considered HU range. Furthermore, it avoids the situation in which slight changes in the anatomy, which introduce or remove extreme HUs or attenuation coefficients (for example, a section without air cavities in the reference CT includes air cavities in the CBCT, or vice versa) does not effect the transformation. Moreover, dividing the histogram into an appropriate number of subsets adapts the CBCT histogram quite well to that of the reference CT, but still respects anatomical changes and deviations in HUs.

One could go one step further in the adaptation process and also assume the skeleton as rigid, thus identifying the coordinates of bony structures in the reference CT and replacing the adapted HUs of the CBCT at these coordinates by those of the reference CT. Bony structures in the reference CT can easily be identified by searching for HUs above a certain threshold. This method is not applied because satisfactory results can already be obtained without bony HU replacements.
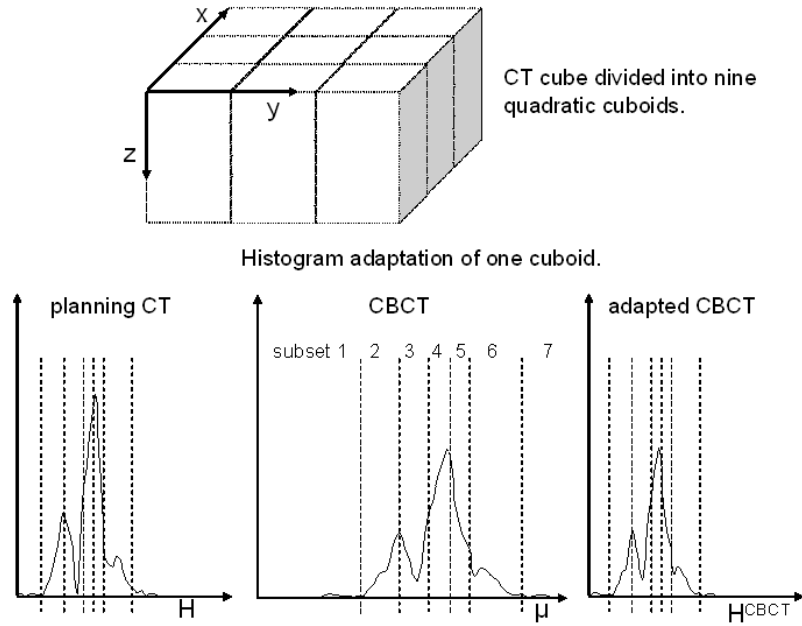
Figure 6.24: Histogram adaptation of a CBCT

*First, the considered part of the planning CT and the CBCT is divided into cuboids with a quadratic base area. The axis of the cuboid is parallel to the longitudinal axis of the CT. Therefore, the transversal slices are divided into squares. For each cuboid the histogram of the CBCT is adapted to the corresponding one in the planning CT. For that purpose the histograms are divided into subsets, each representing the same number of voxels (except the first subset (1) and the last one (7). Then each subset (except 1 and 7) of the CBCT is linearly transformed to the corresponding one of the planning CT. That means it is shifted and stretched in a way that the borders of the subset coincide with those of the planning CT after the transformation. The first and the last subset undergo the same transformation (i.e. the same shift and stretch) as their neighboring ones. Within the single subsets the CBCT keeps it individual shape after the adaptation.*

**Results.**

**Body phantom.** The above described method has been applied to the CBCT of the abdominal body phantom (figure 6.23). Figure 6.25a shows a transversal slice of the adapted CBCT. The slice is divided into numerous quadratic regions of $32 \times 32$ pixels ($\times 25$ pixels in the z-direction) corresponding to $32\,mm \times 32\,mm$ ($\times 75$ mm in the z-direction) that have been adapted to the corresponding regions of the reference CT on the basis of their histograms. In figure 6.25b, a comparison of the HU histograms between the reference CT and the adapted CBCT shows the similarity of both histograms as a result of the adaptation. Ideally, the histograms of both CTs coincide for the phantom because there is no change in the geometry. This is not exactly the case, due to non-linearities in the attenuation coefficients of the CBCT. Nevertheless, these small deviations have only a small impact on dose calculation as is shown in the DVH comparisons in figure 6.25c. A five-beam IMRT plan was generated, optimized on the basis of the horseshoe shaped target volume and the remaining contours defined as OARs. Nearly no differences are observable between the DHVs of the reference- and the adapted CBCT (figure 6.25c. The dose difference distribution of the presented slice stays below $1\,\%$ in nearly the whole area (figure 6.25d.)

The inaccuracies that would occur, when applying the method for small phantoms, described in section 6.3.2, for the dose calculation on the CBCT of the body phantom, are illustrated in figure 6.26. The DVH comparison shows not acceptable differences up to $10\,\%$, for instance in the 'target volume'.

A) Transversal slice of the adapted CBCT of the body phantom. The arrangement of the quadratic regions are visible due to discontinuities at the borders. B) Comparison between HU histograms of the reference CT and the CBCT. The histogram is well adapted but not identical. C) DVH comparison of a five beam IMRT plan. No differences are observable between the VOIs of the reference and the CBCT. D) Dose difference distribution (local percentage dose) of the dose calculations of the reference- and the adapted CBCT.

Figure 6.25: Body phantom – results of CBCT adaptation
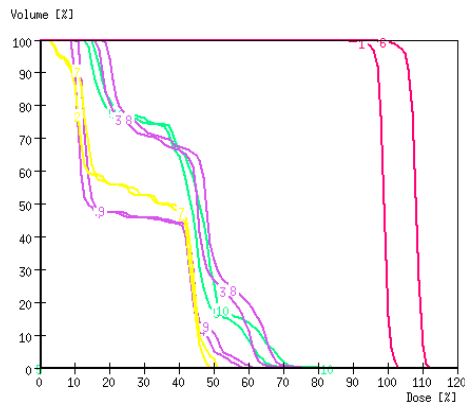


The plot shows a comparison of DVHs between the dose distribution of the planning CT and the dose distribution on the CBCT obtained with the dose calculation method described for small phantoms. The curves labelled with higher numbers (6, 7, 8, 9, 10) belon to the CBCT. Differences up to 10 % are visible.

Figure 6.26: Body phantom – DVH comparison for the 'small-phantom-method'

**Patient.**
As a further example, the CBCT of patient # 17 was adapted to its planning CT using the described method. Dose calculations on the adapted CBCT were performed on the basis of clinical contours and the original seven beam IMRT plan, and compared to those of the planning CT. Figure 6.27a shows a transversal slice with the original contours of the planning CT defined by a physician, the CBCT and the adapted CBCT. In this case, the CBCT was divided into regions of areas four times larger ($64 \times 64$ pixels). That this fragmentation is still sufficient for cupping reduction and HU adaptation is shown in figure 6.27b. HU profiles of the planning CT, and the adapted CBCT in the LR directions, are plotted along the horizontal line drawn onto the CT images. The adapted CBCT shows the same structures as the original CBCT. Small differences to the planning CT, such as can be seen within the rectum and the target volume contours, are respected by the adaption. Differences in the region of the left pelvic bone (that appear due to slight inaccuracies of the image registration) are still present. Nevertheless, the HUs are well adapted to the planning CT, and cupping artifacts that might inhibit an accurate dose calculation are removed by the adaptation.

As the planning CT and the positioning CBCT only differ slightly, the dose distribution of the original seven beam IMRT treatment also does not differ much. The DHV comparison of both dose calculations is plotted in figure 6.27c. Again, the OARs coincide extremely well and only small differences can be seen in the DVH of the target volume at higher doses. The dose difference distribution (figure 6.27d) of the slice shows nearly no difference above one percent in the inner part of the patient.
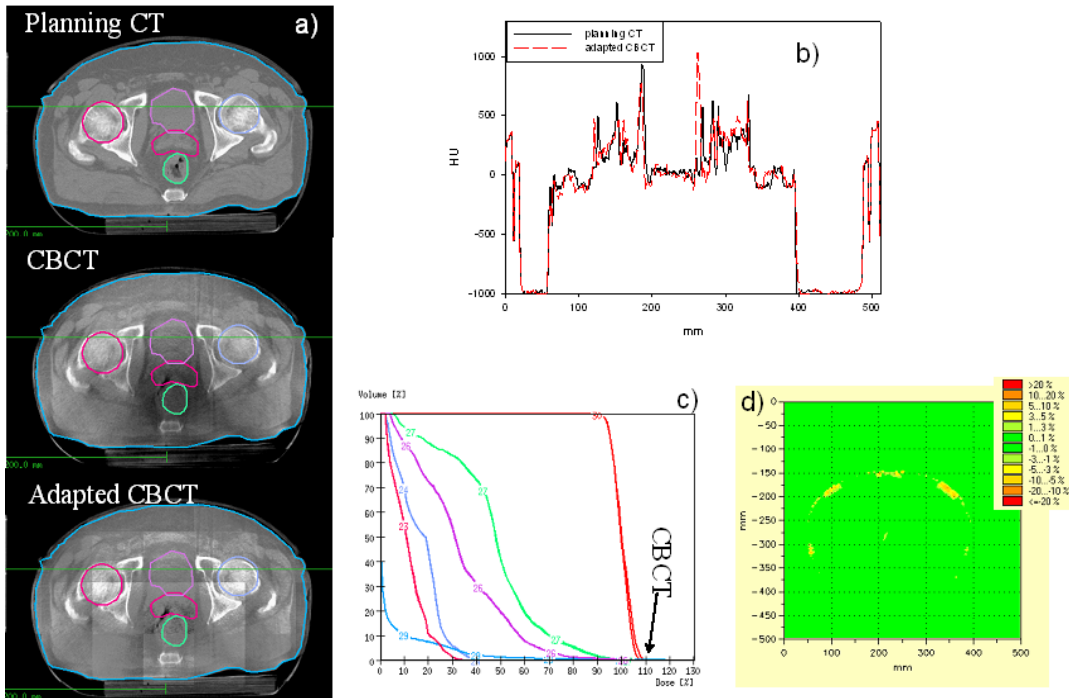


Figure 6.27: Patient #17 – results of CBCT adaptation

*A) Transversal slice of the planning CT, the CBCT and the adapted CBCT. B) HU profiles along the horizontal green line at a) for the reference CT and the CBCT. C) DVH comparison of the original seven beam IMRT plan between the planning CT and the CBCT. Only small parts of the target volume receive slightly higher doses for the CBCT calculation. D) Dose difference distribution (local percentage dose) of the dose calculations of the planning- and the adapted CBCT.*

### 6.3.4   Summary

The weak dependence of electron densities on HU changes in the soft tissue range, which is true for most of the human anatomy, including the head and neck region as shown in figure 6.17, allows small and local HU inaccuracies to be ignored in the dose calculation. With a simple calibration procedure on based on a mean attenuation coefficient for water HUs for a few materials, dose calculations from CBCTs of small objects acquired in free air (without the treatment table within the FOV) using an anti-scatter can be performed very accurately. This could be demonstrated on several phantoms, as well as for head and neck patients.

Larger phantoms and extra-cranial patients already produce more scatter, but there is also additional scatter due to the treatment couch they are placed on, especially at projection angles of around 0°, where the detector is very close to the treatment couch. In this case, even the use of an anti-scatter grid cannot reduce scatter sufficiently to obtain images with only low residual cupping artifacts. It is plausible that the large differences in the measured attenuation coefficients for

homogeneous tissues as exemplarily shown in figure 6.23 inhibit an accurate dose calculation using a single spacially independent HU to electron density function. Therefore, additional information from the reference CT is needed. Since dose calculations are usually based on the planning CT, the setup during the CT acquisition must be identical to the treatment setup. Everything outside the patient that is transversed by the treatment beam must be identical. Therefore, HUs of voxels that are outside the patient in both CTs, such as those from the treatment couch, can be replaced on the CBCT by the original values. Furthermore, the attenuation coefficients inside the patient's anatomy obtained from the CBCT reconstruction had to be transformed into HUs by means of the HU histogram of the reference CT. Although, disturbing quadratic region boundaries arising from the region-wise histogram adaptation are visible on the adapted CBCT, but the adaptation is performed only for dose calculation purposes. The visualization and analysis of the dose distributions can be done on the original CBCT.

A more preferable CBCT dose calculation on CBCT of large objects, independent of the reference CT, at least presumes an accurate scatter correction of the CBCT projections in order to avoid disturbing cupping artifacts [90]. An approach using a simple, direct raw image based scatter estimation and correction proposed in [91] is tested in the next section.

## 6.4   Application of a simple, direct method of scatter correction

A simple and direct method for scatter estimation and correction is proposed by Siewerdsen et.al. [91]. The published method is based on the assumption that no primary x-ray- signal of a kV-beam can measured on the FPI in the collimator shadow (behind the leaves). This can be taken for granted for the used spectrum. Therefore, the complete signal in the collimator shadow results from scattered radiation. The 2D scatter fluence shall then be estimated by interpolating the shadow signal over the complete area of interest, i. e. the phantom shadow on the FPI. The interpolation is applied by fitting second order polynomials to the gray value data in the collimator shadow along the columns in the v-direction. For scatter correction, the polynomials are then subtracted from the raw data.

**Constraints.** Even if there is only the air gap and no phantom or any other scattering object between the x-ray source (including the aperture) and the FPI, one will measure a signal in the collimator shadow beyond the penumbra for any non-closed beam shape. This is true for several reasons:

1. Light scatter in the scintillator material. This signal depends on the FPI signal of the irradiated pixels and drops down to approximately one percent after 20 pixels behind the beam edge.

2. Scatter from the collimator edges and, presumably to a minor degree, from the tube filtration that includes an aluminium disk at the beam exit. Figure 6.28 shows a projection of a phantom that is partly covered by the collimator leaves. The red lines indicate the leaf edges. With an adapted windowing setting, structures of the phantom can be recognized in the collimator shadow. These structures are visible due to the attenuation of the scattered x-rays from the collimator.
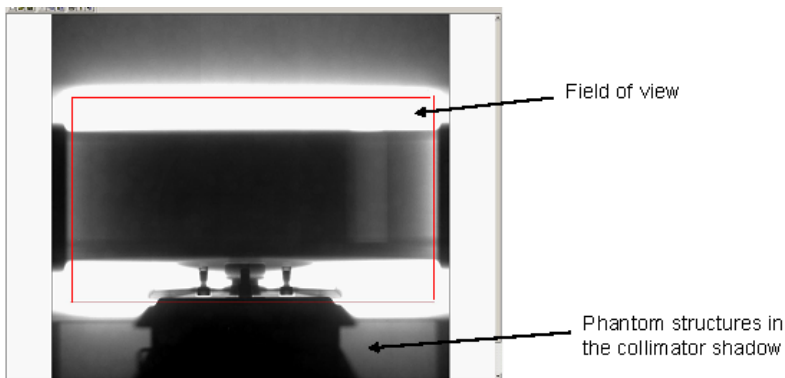


*The picture shows a screenshot of the FPI imaging software. The red rectangle indicates the FOV. Primary x-rays are absorbed to more than 99.9 % within the collimator leaves. The signal outside the FOV (behind the collimator leaves) is caused by off-focal radiation.*

Figure 6.28: Phantom structures within the collimator shadow

It is assumed that, within the phantom shadow, both effects are low compared to the phantom scatter. However, the sum of these effects may lead to gray values within the collimator shadow that are higher than those in the phantom shadow of the FOV. This is mostly the case if the off-focal radiation hits the FPI without further attenuation by the phantom. This is illustrated in figure 6.29, which shows a projection of a phantom not exceeding the field edges in the v-direction[9] (a), a profile of FPI signal through the phantom shadow along the red line (b), and a profile through the collimator shadow along the green line (c). The pixel values in the collimator shadow are much higher than in the phantom shadow. Therefore, the amount of scatter would be enormously overestimated with this attempt.

Outside the phantom shadow, gray values resulting from these effects may exceed those from

---

[9]The v-axis is taken to be parallel to the y-axis, and the u-axis parallel to the x-axis of the FPI.
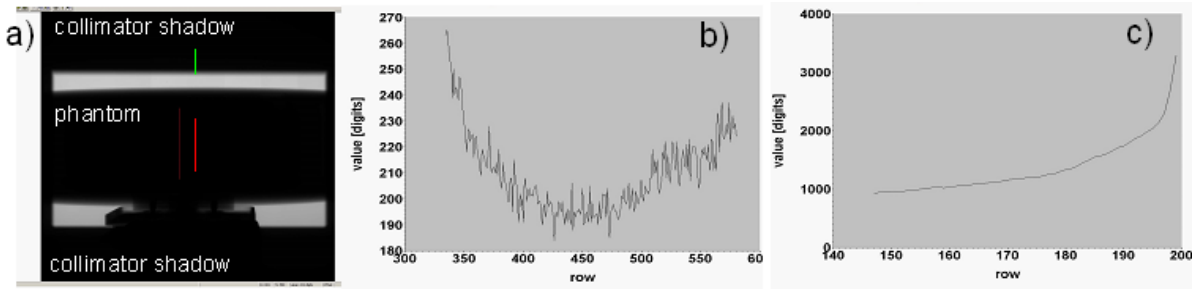
Figure 6.29: Profiles through phantom- and collimator shadow

*A) Screenshot of the FPI imaging software. B) Profile through the collimator shadow along the green line . C) Profile through the phantom shadow along the red line. The origin of the FPI's active area ([x,y] = [0,0]) is represented by the upper left corner of the imaging screen (see figure 2.5). Lower rows represent lower y-coordinates.*

the phantom scatter. Therefore, the applied method is only applicable if the phantom size sufficiently exceeds the field edges in the v-direction. This requirement is assumed to be fulfilled unless otherwise noted.

### 6.4.1 Scatter fluence estimation of single projections

First tests of the scatter estimation/correction were applied on the water phantom (radius: 9 cm, length: 24 cm). KV cone beam projections were acquired for the following orientations: at $\Theta = 0°$ (gantry: 0°), phantom placed in free air (i. e. treatment table outside the FOV), phantom center at room-coordinates [x,y,z] = [0,0,0] (isocenter) and, to increase the amount of scattered radiation on the projections, also at [0,0,-10 cm] and [0,0,-20 cm]. Other orientations included $\Theta = 180°$, phantom on treatment couch, and phantom center at [0,0,0], [0,0,10 cm] and [0,0,20 cm], respectively. To get an idea of the real amount of scatter (here, and in the following references, scatter denotes only the scattered radiation from the phantom and the treatment couch) on the FPI, the acquisitions at $\Theta = 0°$ were repeated with a beam blocker (BB: a circular piece of lead, radius: 1.5 cm, thickness: 3 mm - attenuation of initial radiation > 99.9 %) on top of the phantom within the FOV. The signal on the FPI in the shadow of the BB should mainly result from scatter. Images were acquired at 50 mA × 20 ms and averaged over 10 projections corresponding to a dose of approx 0.7 mGy at the phantom for the phantom placed free air at the isocenter. Images were acquired with and without an anti-scatter grid[10]. The FOV was fixed to 12 cm in the v-direction and 40 cm in the u-direction on the FPI plane. The projection data (1024 × 1024 pixels at 0.4 mm pitch) were processed at half-resolution to yield projections of dimension 512 × 512 pixels with pixel pitch 0.8 mm, which is what is used for CBCT reconstruction. All data were open-field corrected. The following discussion refers to 512×512 open-field corrected data unless otherwise noted.

**Signal decay in the v-direction at FOV edges.** Figure 6.30 shows an example of signal decay at the FOV edges in the v-direction. The steep gradient between pixel #314 and pixel #322 belongs to the signal in the leaf edge penumbra. In this example, pixels #322 onwards can be used for scatter fluence estimation. For each column of the image data, the 50 pixels closest to the leaf penumbras on both sides outside the v-boundary of the FOV were (row by row) interpolated using a quadratic function for phantom scatter estimation. No filtering was applied in the u-direction. The estimated scatter fluence was subtracted from the projection data. The negative logarithm of the 'scatter corrected' data represents the total x-ray attenuation $p$ through the phantom (and treatment couch), and, therefore, for the free air imaged water phantom, the path length of the primary x-rays through the phantom (assuming the attenuation coefficient of air is zero). These

---

[10]Within this section it is always explicitly mentioned if the anti-scatter grid was used.
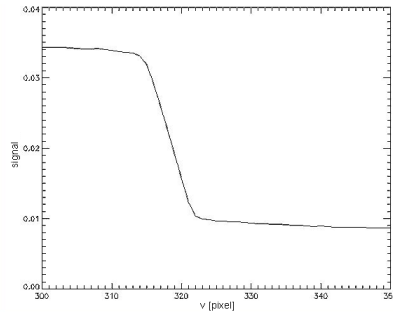
*An example of signal decay (within the phantom shadow) at the collimator edges is shown. Signal values refer to open-field corrected projections, pixel numbers to a 0.8 mm pitch.*

Figure 6.30: Signal decay at the FOV edges

data were analyzed and compared to data that had not been scatter corrected, data acquired with the anti-scatter grid, and the expected 'ideal' data. Furthermore, the amount of estimated scatter was compared to the signal behind the BBs.

**Profiles in u-direction.** Figure 6.31 shows profiles of logarithmized (and open-field corrected) FPI values through the shadow of the water phantom in the u-direction.
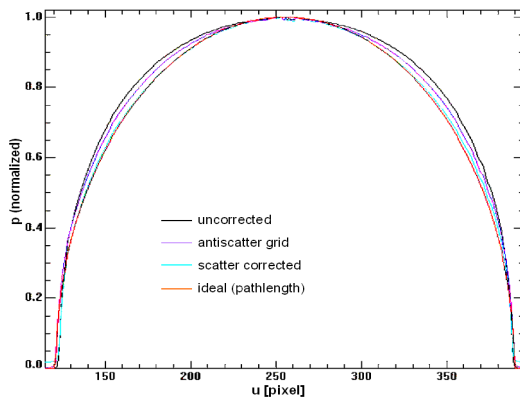


*The plot compares path lengths through the water phantom (obtained from the uncorrected, from the scatter-corrected projection and from the projection acquired with an anti-scatter grid) to the idealized path lengths for a punctiform x-ray source. All curves are normalized to their maximum for better comparability.*

Figure 6.31: Radial profiles through the shadow of the water phantom

Projections were acquired at $\Theta = 0°$ with the phantom center placed at $z = -20$ cm. All profiles are normalized to their maximum. The black curve represents the uncorrected image, the blue one the scatter corrected, and the violet one the projection acquired with anti-scatter grid. The orange curve represents the path length of the x-rays under the given geometry. The broader shape of the uncorrected profile indicates cupping artifacts. The path length through the periphery of the phantom center seems to be overestimated without scatter correction. In fact, considering the absolute p-values, path lengths are more underestimated through the phantom center than through the periphery. In this (relative) profile comparison, the scatter correction yields better results than the anti-scatter grid and delivers profiles, hardly distinguishable from the idealized curve.

**Quantification of the scatter correction:** To estimate the real amount of scatter on the FPI, the expected scatter-free signal was simulated and compared to the measured signal[11] and the scatter corrected signal. The quotient of the measured signal $p$ and the simulated signal $p_{sim}$ should be 1 for scatter-free projections, less than 1 for projections including scatter, and greater than 1 for projections corrected on the basis of an overestimated scatter distribution. The simulated signal

---

[11]Here, and in the following references, 'signal' means the logarithmized, open field corrected FPI signal; 'FPI signal', 'FPI values' or 'FPI (raw) data' mean the (open-field corrected) FPI gray values.

is based on the simulated x-ray spectrum[12] to account for beam hardening effects, and on the assumption that the detector response is proportional to the energy absorbed in the scintillator. Both the spectrum and the detector response simulation may be subject to errors, so this quantification may only be seen as an approximation. Figure 6.32 shows the quotients for uncorrected, and corrected, to simulated signal in the u-direction for the middle of the phantom center placed at z = -20 cm ($\Theta = 0°$). The absolute values and the black curve indicate the amount of scattered
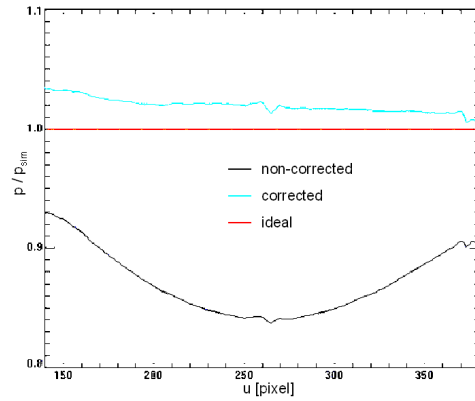


*Water phantom: Ratio of measured to expected signal (absorbed energy fluence of primary x-rays at the scintillator) in the u-direction. The red line indicates (signal ratio = 1) expected ideal run of the curves.*

Figure 6.32: Ration of measured and expected u-profile

radiation and the increasing scatter ratio towards the center of the phantom shadow, as already shown in figure 6.31. The approximate homogeneity, and the values close to 1 of the blue curve compared to the black one, indicate a quantitatively satisfactory scatter estimation, in addition to the already illustrated qualitative, cupping reducing scatter correction (see figure 6.31).

As a further test for the method, the kV-acquisitions at $\Theta = 0°$ were repeated with a BB on top of the phantom. The corrected FPI data should deliver zero values in the BB shadow. Figure 6.33 shows a FPI projection of the phantom with a BB (a) and the associated estimated scatter fluence (b) that was subtracted for scatter correction.
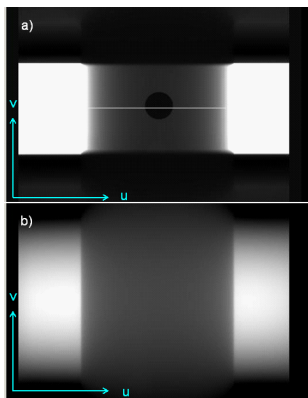


*A) Projection of the water phantom with BB. B) Estimated scatter fluence of the projection. Brighter pixels indicate higher values. Outside the phantom shadow, the scatter fluence is highly overestimated. The plot shows a profile along the white line in (a) of the uncorrected (black) and the corrected FPI signal (blue).*

Figure 6.33: Scatter estimation check with BB

The profiles along the white line in (a) shows, that the corrected FPI values within the shadow of the BB are mostly very close to zero (blue curve), which is a further sign for a quantitatively good scatter correction of the measured profile (black curve).

---

[12]The spectrum was simulated with the *x-ray toolbox*.

Different acquisition setups yield similar results. An example of this is illustrated in figure 6.34. The graph shows plots in accordance with figures 6.32 and 6.33 for the phantom placed on the couch at z = -20 cm (i. e. the couch is placed in the FOV between phantom and FPI) and $\Theta = 0°$. The higher scatter ratios at the projections with the treatment table within the FOV, indicated
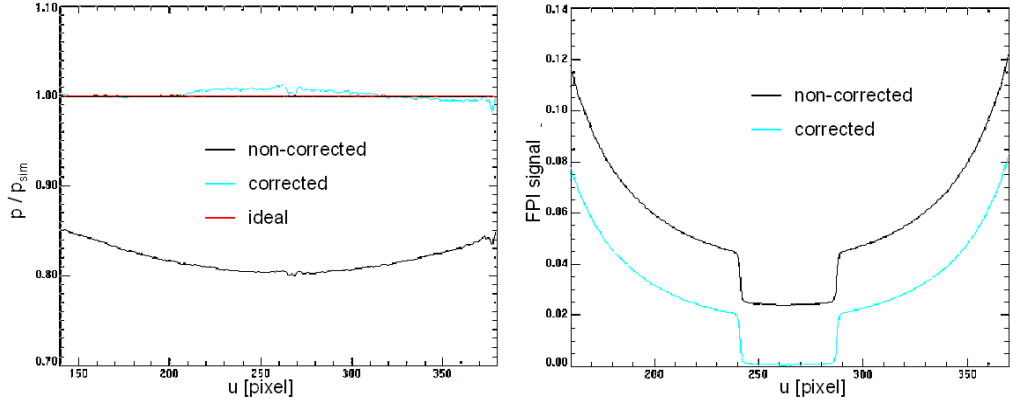


Figure 6.34: Scatter correction with treatment table in within FOV

*Left: Ratio of measured to expected signal in the u-direction. The red line indicates (signal ratio = 1) expected ideal run of the curves. Right: Profile through phantom shadow and BB shadow of the uncorrected (black) and the corrected EPI signal (blue).*

by the lower values of the black curve at the left graph compared to figure 6.32, are corrected very well towards the estimated ideal profile with the described method (blue curve). This is also obvious in the right graph; the comparison of the black curve with the plot in figure 6.33 shows that slightly higher signals are measured with the FPI despite the presence of an additional x-ray absorber (treatment table), due to an increased amount of scattered radiation. Nevertheless, it may be corrected very accurately for the given geometry.

**Influence on CBCT reconstructions.** To evaluate the influence of the projection profile accuracy on CT reconstruction, the u-profiles from the phantom placed in free air at z = 20 cm ($\Theta = 0°$) were duplicated in a CBCT sequence of 360 projections simulating an SID of approximately 120 cm and a fixed SDD of approximately 142 cm. This setup was chosen to obtain a larger amount of scatted radiation on the FPI to correct for, compared to an isocentric phantom geometry. An actual cone beam CT acquisition with this geometry would exceed the FOV because the phantom would be placed too far outside the isocenter. Figure 6.35 shows profiles through the reconstructed attenuation coefficients in the LR direction (along the x-axis of the patient system) for the uncorrected CBCT reconstruction (black), the CBCT reconstruction from the anti-scatter grid projection (violet), the scatter-corrected CBCT reconstruction (blue), and the CBCT reconstruction of the idealized profile. The curves are normalized to the phantom center's attenuation coefficient. As expected, due to the better projection profiles in the u-direction (see figure 6.31), the scatter correction delivers better results than the anti-scatter grid acquisition. As an indicator to quantify the cupping on the reconstruction, the normalized attenuation coefficient $\mu_{8cm}$ at 8 cm from the phantom center ($x = \pm 8$ cm) is considered. The values are as follows: uncorrected: $\mu_{8cm} = 1.22$ a.u., antiscatter grid: $\mu_{8cm} = 1.10$ a.u., scatter corrected: $\mu_{8cm} = 1.03$ a.u. In other words, the cupping was reduced from 22 % to 3 % outside the outside the phantom center by the scatter correction.
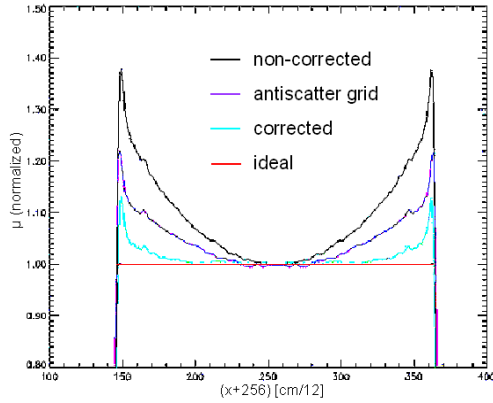
Reconstructed attenuation coefficients along the x-axis of the patient coordinate system for artificial CBCT sequences with and without scatter correction, and with anti-scatter grid. The red line indicates the ideal run of the profile. The profiles are normalized to the attenuation coefficient of the phantom center.

Figure 6.35: Cupping at simulated CBCTs

## 6.4.2 Application on CBCT data

To test the method with real CBCT data, the sequence of a cubic $30 \times 30 \times 30 \, \text{cm}^3$ RW3 phantom assembled from quadratic slabs was acquired, with and without an anti-scatter grid. The middle disc of the contrast phantom was integrated into the central slab of the phantom. The phantom was placed on the treatment couch with its center at the isocenter and the contrast phantom disc at y=0. CBCT acquisition was performed as full scan with $\Theta = 1.0°$. The 2D scatter fluence estimation, a lateral smoothing in the u-direction across all columns, was performed, characterized by a rectangular kernel of 20 pixels to reduce noise in the reconstruction. The projection at $\Theta = 0°$, sans anti-scatter grid, was repeated with a BB on top of the phantom to get an idea of the scatter estimation accuracy. Figure 6.36 shows profiles of the uncorrected and scatter-corrected projections including the BB shadow, comparable to the graph in figure 6.33. Although the scatter seems to
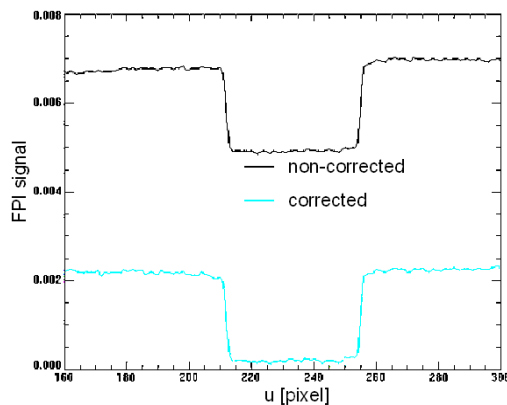


Lateral profile through phantom shadow and BB shadow of the uncorrected (black) and the corrected FPI signal (blue) obtained from the projection at $\Theta = 0°$ of the RW3 cube.

Figure 6.36: Scatter correction check at RW3 phantom

be slightly underestimated in the BB shadow, it is still of the correct order of magnitude despite the high SPR, which can be estimated from the profiles to be approximately 300 %.

An inner region of a transversal slice with the reconstruction of the uncorrected data, the scatter-corrected data, and the projections acquired with the anti-scatter grid is shown in figure 6.37.
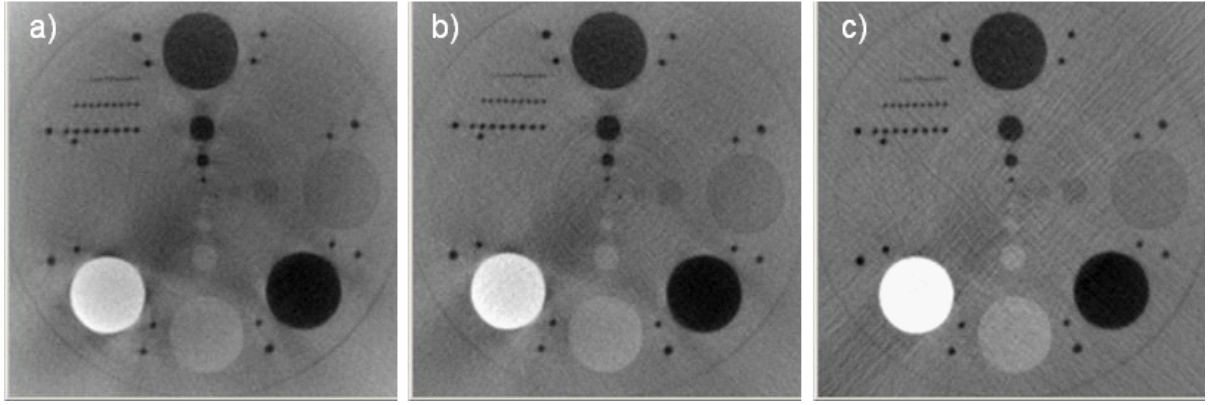
Figure 6.37: Central slice of the RW3 cube

*Reconstructions of the RW3 cube obtained from the uncorrected projections (a), from the projections acquired with anti-scatter grid (b) and from the scatter-corrected projections (c). The ring in the outer part of all three images represents a small air gap of radius of approximately 8 cm.*

As indicators for image quality of the reconstruction, the following parameters were taken into account:

- The lateral cupping within 10 cm radius in a homogeneous transversal slice (without any inserts),

- the noise ratio $\frac{\sigma}{\mu}$ of each 3 cm insert, and

- the CNR $\left( = \frac{|\mu - \mu_{bg}|}{\sigma + \sigma_{bg}} \right)$ of each 3 cm insert.

Furthermore, an attempt of a HU calculation on the different reconstruction was made.

**Cupping.** Figure 6.38 shows a comparison of the cupping in the reconstructions. Since the phan-
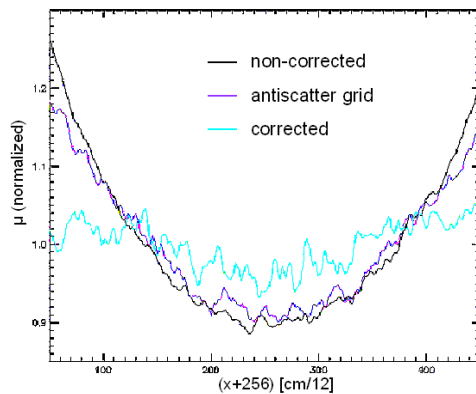


*Reconstructed attenuation coefficients along the x-axis of the patient coordinate system CBCT reconstructions of the RW3 cube with- and without scatter correction and with antiscatter grid. The profiles are normalized to their mean values.*

Figure 6.38: Cupping at the RW3 cube

tom size exceeds the FOV, cupping is not only caused by scatter but also by projection truncation. Therefore, only the inner part of the observed slice was taken into account. The attenuation coefficient profile along the x-axis of the reconstruction of the anti-scatter grid acquired projections (violet) shows a similar amount of cupping as the profile through the uncorrected reconstruction (black) with increased noise. The scatter-corrected projections yield cupping reduced reconstructions (blue curve) with a further noise increment, which can be seen in figure 6.37.

**Noise.** A comparison of noise ratios at the different inserts is given in table 6.7. Insert 1 (lung tissue equivalent) is not considered due to its material inhomogeneities. The noise of the single inserts

Table 6.7: Noise ratios $\frac{\sigma}{\mu}$ at the RW3 cube

|  | uncorrected | antiscatter grid | scatter corrected |
|---|---|---|---|
| insert 2 | 2.3 % | 2.9 % | 3.3 % |
| insert 3 | 3.8 % | 3.8 % | 3.1 % |
| insert 4 | 3.0 % | 3.3 % | 3.0 % |
| insert 5 | 3.7 % | 6.2 % | 18.0 % |
| insert 6 | 3.6 % | 3.5 % | 3.2 % |
| background | 2.7 % | 2.8 % | 3.8 % |

*The ratio $\frac{\sigma}{\mu}$ of the standard deviation and the mean value of the reconstructed attenuation coefficients of the 3 cm inserts is given.*

is, in most cases, very low and does not differ much between the different reconstructions. The comparability of the given noise ratios despite the different noise observed at the profiles (shown in figure 6.38) is due to the cupping that also affects the $\sigma$ of the inserts. Therefore, the $\sigma$ value of reconstructions including cupping artifacts is more like an attenuation coefficient uncertainty than real noise.

Insert 5 shows a strong increase of noise ratio from the uncorrected to the corrected reconstruction. This is due to the higher sensitivity of the relative noise for the low attenuation coefficient of air. Streaks in the reconstruction, as clearly visible in figure 6.38, cause a higher noise ratio for the scatter-corrected reconstruction, and for that acquired with an anti-scatter grid, because they deliver better attenuation coefficients (closer to zero) for air (see paragraph *Hounsfield units* within this section).

**CNR.** A comparison of CNRs of the different inserts is given in table 6.8. Insert 1 is not considered due to its material inhomogeneities, and the background itself is also not considered because its CNR is zero by definition. Obviously, the CNRs increase from uncorrected, to anti-scatter grid,

Table 6.8: CNRs at the RW3 cube

|  | uncorrected | anti-scatter grid | scatter corrected |
|---|---|---|---|
| insert 2 | 0.1 | 0.1 | 0.3 |
| insert 3 | 10.0 | 14.7 | 21.4 |
| insert 4 | 3.4 | 4.9 | 6.0 |
| insert 5 | 14.6 | 21.0 | 24.3 |
| insert 6 | 0.6 | 1.0 | 2.0 |

*The ratio $\frac{|\mu - \mu_{bg}|}{\sigma + \sigma_{bg}}$ of the mean attenuation coefficients difference of the 3 cm inserts and the background and their mean standard deviations is given.*

to scatter-corrected reconstruction. Due to the high noise ratio of insert 5 at the scatter corrected reconstruction, the CNR increases there only slightly. Therefore, the contrast itself is much higher.

**Hounsfield units.** Under the partially correct assumption that RW3 is water equivalent for the used spectra, pseudo-HUs were calculated by $H = 1000 \cdot \left( \frac{\mu}{\mu_{bg}} - 1 \right)$. The reference attenuation coefficient $\mu_{bg}$ is taken from the corresponding background of each reconstruction. Table 6.9 lists the calculated pseudo-HUs. Compared to the HUs obtained from the diagnostic FBCT (see table

Table 6.9: (Pseudo-)HUs at the RW3 cube

|          | uncorrected | antiscatter grid | scatter corrected |
|----------|-------------|------------------|-------------------|
| insert 1 | $-236 \pm 52$ | $-378 \pm 42$ | $-539 \pm 68$ |
| insert 2 | $47 \pm 64$ | $53 \pm 62$ | $95 \pm 64$ |
| insert 3 | $398 \pm 96$ | $630 \pm 106$ | $1192 \pm 125$ |
| insert 4 | $96 \pm 71$ | $154 \pm 71$ | $272 \pm 72$ |
| insert 5 | $-376 \pm 43$ | $-579 \pm 34$ | $-825 \pm 33$ |
| insert 6 | $-26 \pm 66$ | $-37 \pm 60$ | $-32 \pm 56$ |

*The table lists the pseudo-HUs of the 3 cm inserts calculated using the mean attenuation coefficient of the background $\mu_{bg}$ (see figure 6.1) as reference for $H = 0$. Therefore, the pseudo-HU of the background is zero by definition for all reconstructions.*

6.1), the CBCT reconstruction delivers the best pseudo-HUs with the scatter-corrected projections for materials with attenuation coefficients that strongly differ from water, i.e. inserts 1, 3, 4 and 5 in this case. Nevertheless, the reconstructed pseudo-HUs still do not show satisfactory agreement with the expected values (HUs from the diagnostic FBCT scanner). Considering these data, the scatter correction method does not seem to have the potential to deliver accurate HUs over the complete FOV.

### 6.4.3   Conclusion

Considering the studied cases, the tested scatter correction method seems to be feasible on prism-like shaped phantoms (including cylinder) aligned in the y-direction with y-dimensions sufficiently exceeding the FOV edges. For small phantoms particularly, it seems to deliver a quantitatively good estimation of the 2D scatter fluence. An additional estimation of signal in the collimator shadow caused by off-focal radiation and scintillator scatter might allow scatter correction of phantom shadows having somewhat too small y-dimensions; but this has not yet been investigated in detail.

CBCT reconstructions of scatter corrected projections show fewer cupping artifacts but increased (cupping independent) noise. Noise could partly be reduced by u-filtering of the estimated scatter distribution. V-leafs shadows should cover a sufficiently large part of the FPI to allow an accurate scatter estimation. Good results were obtained using 40 mm on both sides of the FOV in the v-direction behind the collimator penumbra. Using smaller collimator shadows, for scatter estimation, one should be sure to use pixels far beyond the collimator penumbra in order to avoid overestimations due to the steep signal gradient at the penumbra. However, all of this results in a decreased longitudinal FOV.

HUs could not be reconstructed to a satisfactory level. Further investigations may possibly solve this problem. Projections with a shifted FPI have not yet been investigated, but the accuracy of scatter estimation did not seem to degrade at the periphery of the centered FPI.

# Chapter 7

# Summary & Outlook

The presented work mainly focuses on the technical development and the linac integration of a kV-cone beam imaging setup. The components and the development process are described in detail, starting from an initial bench top setup to the implementation of a prototype design appropriate for clinical applications. Several hardware and software components have been developed and implemented, which either enable the control and the interaction of the individual parts of the system for the Inline concept characterizing applications, or integrate peripheral features such as the respiratory gating system.

In summary, an IGRT system was designed and realized with the idea to integrate kV-imaging at a MV-treatment machine, sharing one axis for both the treatment beam, and the imaging beam and additionally supporting MV-imaging applications without the need of a second x-ray detector. Multiple applications were proposed in section 3.2, and partly also provided by the development and integration of additional hardware and software (see, for instance, section 5.4 or 5.5).

The main features of the developed system are:

- Acquisition of kV-CBCTs of the patient in treatment position.

- Acquisition of kV-projections in treatment beam direction during dose delivery.

- MV beam tracking.

- Acquisition of 4D-CBCTs.

The provided features may allow, for example, the following applications (partly in combination with further additionally developed peripheral components):

- Detection and correction of set-up errors.

- Detection and correction of inter-fractional and intra-fractional patient motion.

- Calculation of actual delivered dose on the basis of CBCTs in treatment position.

- Entrance dosimetry on the basis of the real-time monitored treatment sequence.

- 4D-CBCT acquisition.

- MV-beam gating on the basis of real-time monitored breathing motion.

- etc.

Several investigations and measurements using the provided platform are described within this work and in several further publications, concerning, for instance, 4D-imaging [67], [68], patient studies [82], [81], dose guided RT [45], [84], and others [73], [92] – [96].

The system was found to be appropriate for clinical applications. Several CBCTs of patients were acquired and followed by an immediate repositioning. Furthermore, 4D-imaging of patients was performed, and first attempts towards dose guidance were carried out on the basis of treatment beam imaging.

It rests with the team of clinicians and medical physicists to deploy the potential of the presented system with all of its features, e. g. to perform patient positioning correction by utilizing also rotational degrees of freedom. Dose calculations from CBCT data were shown to be feasible with good accuracy and might be used, possibly in combination with entrance dosimetry, for the control of actual delivered dose distributions and, in a further step, to inter-fractionally adapted treatment plans, with the aim to ensure a close compliance with the dose prescriptions [97], [98].

The image quality of CBCTs is still low compared to that of diagnostic FBCTs. A crucial limitation of image quality is the large amount of scattered radiation on the wide field projections of CBCTs. One major goal and subject of further investigations is the reduction of scatter artifacts and, closely related to it, an accurate reconstruction of Hounsfield units. A simple, direct approach for scatter correction has been tested to yield improvements in image quality and HU reconstruction for certain geometries.

One promising feature of the Inline concept, i. e. the fluoroscopic tracking of lateral organ motion during the beam delivery and the possibility to overlay the kV-projection with the current (scaled) beam shape, has not been considered during this work. The real-time evaluation of the image data combined with an immediate reaction like gating or the adaptation of the beam shape to the target volume, requiring appropriate algorithms and sufficient computing power, is a work in progress.

The successful clinical studies with the IGRT prototype developed in this work lead to a first commercial realization of the Inline IGRT concept, the developement of the $Art\acute{\iota}ste^{\text{TM}}$ by Siemens/OCS.

## 7.1 The Artíste

The Artíste of Siemens/OCS is the first commercial implementation of the Inline concept for IGRT. It was constructed partly on the basis of the developments and investigations described in this work. Figure 7.1 shows an experimental prototype version of this treatment machine.
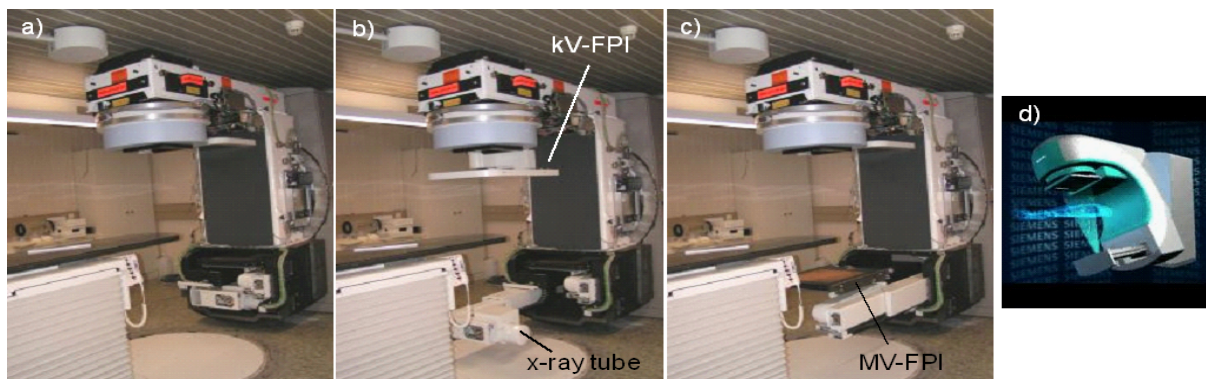


Figure 7.1: The Artíste

*A) Artíste Prototype with all imaging components in park position. B) x-ray tube and kV-FPI in operational position. C) MV-FPI in operational position. No covers are currently mounted at the machine. Picture (d) gives a design example of the Artíste with covers.*

The current version of the prototype employs the same kV-source and FPI that were used in this work and were found to be appropriate for clinical applications. As an additional feature, a second FPI (the *MV-FPI*, in contrast to the *kV-FPI*), as already suggested in section 3.2, is installed above the x-ray tube for further MV-imaging purposes. The integration of the three hardware components (two FPIs and the x-ray tube) results in several additional mechanical degrees of freedom. The x-ray tube has its park position inside the gantry and can be moved along the y-direction to the point where the focus is at the room coordinate $[0, 0, -100\,\text{cm}]$. In this position, it can be tilted a few degrees around its motion axis. A tilt is performed automatically to adjust the central ray at the center of the kV-FPI's active area shifted laterally for FOV extension. The kV-source incorporates a rectangular collimator with four independently adjustable leaves to collimate the kV-beam in the u- and the v-direction. The kV-FPI is parked between the MLC and gantry, and can be moved below the MLC where its z-coordinate is adjustable within a certain range. Furthermore, a lateral shift in the x-direction is possible for a FOV extension during CBCT acquisition. The MV-FPI parks inside the gantry above the x-ray tube, and can also be driven in the y-direction to the point where its center is at $y = 0$. Furthermore, it can be moved upwards to $z = 0$ and also be shifted laterally along the x-direction, as well as along the y-direction.

## 7.2   Conclusion

With the technical development, realization and clinical application, the potential of an IGRT system, following the Inline concept, could be demonstrated. Image guided RT was successfully performed with this setup for head and neck cases, as well as for prostate patients. The further integration of 4D-imaging methods additionally allowed lung specific applications. Together with the demonstrated feasibility of further Adaptive Radiotherapy related features concerning, for instance, dose guidance, real-time motion tracking during beam delivery, etc., a powerful tool was provided for the new area of image guided radiation oncology that allows our clinical colleagues to develop 'the art of ART' with the newly designed ARTÍSTE system.

# List of Figures

# List of Tables

# Bibliography

[1] T. Bortfeld. IMRT: a review and preview. Phys Med Biol. 2006 Jul 7;51(13):R363-79.

[2] U. Oelfke, T. Bortfeld. Inverse planning for photon and proton beams. Med Dosim. 26, 113 (2001).

[3] K. Herfarth, A. Pirzkall, F. Lohr, D. Schulz-Ertner, J. Spoo, C. Frank, M. Bahner, O. Pastyr, J. Debus J. [First experiences with a noninvasive patient set-up system for radiotherapy of the prostate] Strahlenther Onkol. 2000 May;176(5):217-22. German.

[4] A. McKenzie, M. van Herk, B. Mijnheer. The width of margins in radiotherapy treatment plans. Phys Med Biol. 2000 Nov;45(11):3331-42.

[5] A. McKenzie, M. van Herk, B. Mijnheer. Margins for geometric uncertainty around organs at risk in radiotherapy. Radiother Oncol. 2002 Mar;62(3):299-307.

[6] G. Mageras, G. Kutcher, S. Leibel, M. Zelefsky, E. Melian, R. Mohan, Z. Fuks. A method of incorporating organ motion uncertainties into three-dimensional conformal treatment plans. Int J Radiat Oncol Biol Phys. 1996 May 1;35(2):333-42.

[7] J. Killoran, H. Kooy, D. Gladstone, F. Welte, C. Beard. A numerical simulation of organ motion and daily setup uncertainties: implications for radiation therapy. Int J Radiat Oncol Biol Phys. 1997 Jan 1;37(1):213-21.

[8] J. Balter, G. Chen, C. Pelizzari, S. Krishnasamy, S. Rubin, S. Vijayakumar. Online repositioning during treatment of the prostate: a study of potential limits and gains. Int J Radiat Oncol Biol Phys. 1993 Sep 1;27(1):137-43.

[9] A. Martinez, D. Yan, D. Lockman, D. Brabbins, K. Kota, M. Sharpe, D. Jaffray, F. Vicini, J. Wong J. Improvement in dose escalation using the process of adaptive radiotherapy combined with three-dimensional conformal or intensity-modulated beams for prostate cancer. Int J Radiat Oncol Biol Phys. 2001 Aug 1;50(5):1226-34.

[10] D. Yan, F. Vicini, J. Wong, A. Martinez. Adaptive radiation therapy. Phys Med Biol. 1997 Jan;42(1):123-32.

[11] L Dawson, M. Sharpe. Image-guided radiotherapy: rationale, benefits, and limitations. Lancet Oncol. 2006 Oct;7(10):848-58.

[12] L. Xing, B. Thorndyke, E. Schreibmann, Y. Yang, T. Li, G. Kim, G. Luxton, A. Koong. Overview of image-guided radiation therapy. Med Dosim. 2006 Summer;31(2):91-112.

[13] U. Oelfke. Image guided radiotherapy at DKFZ. Radiother Oncol 73 (Suppl.1), (2004) 10.

[14] T. Tücking, S. Nill, B. Hesse, U. Oelfke. Bildgestützte Strahlentherapie am DKFZ. In: E-Verhandlungen 2006. Abstracts der Frühjahrstagung in Heidelberg. Heidelberg: Deutsche Physikalische Gesellschaft (DPG) (2006) 11.2.

[15] D. Jaffray, D. Drake, M. Moreau, A. Martinez and J. Wong. A radiographic and tomographic imaging system integrated into a medical linear accelerator for localization of bone and soft-tissue targets. Int. J. Radiat. Oncol. Biol. Phys. 45 773-89 (1999).

[16] D. Letourneau, J. Wong, M. Oldham M, M. Gulam, L. Watt, D. Jaffray, J. Siewerdsen, A. Martinez Cone-beam-CT guided radiation therapy: technical implementation. Radiother Oncol. 2005 Jun;75(3):279-86.

[17] D. Yan, E. Ziaja, D. Jaffray, J. Wong, D. Brabbins, F. Vicini, A. Martinez. The use of adaptive radiation therapy to reduce setup error: a prospective clinical study. Int J Radiat Oncol Biol Phys. 1998 Jun 1;41(3):715-20.

[18] U. Oelfke, T. Tücking, S. Nill, A. Seeber, B. Hesse, P. Huber, C. Thilmann C. Linac-integrated kV-cone beam CT: technical features and first applications. Med Dosim. 2006 Spring;31(1):62-70.

[19] B. Groh. A study of the use of flat-panel imagers for radiotherapy verification. Dissertation Naturwissenschaftl.-Mathematische Gesamtfakultät, Universität Heidelberg, (2000).

[20] B. Groh, J. Siewerdsen, D. Drake, J. Wong, D. Jaffray. A performance comparison of flat-panel imager-based MV and kV cone-beam CT. Med Phys. 2002 Jun;29(6):967-75.

[21] H. Rehbinder, C. Forsgren, J. Lof. Adaptive radiation therapy for compensation of errors in patient setup and treatment delivery. Med Phys. 2004 Dec;31(12):3363-71.

[22] M. Oldham, D. Letourneau, L. Watt, G. Hugo, D. Yan, D. Lockman, L. Kim, P. Chen, A. Martinez, J. Wong. Cone-beam-CT guided radiation therapy: A model for on-line application. Radiother Oncol. 2005 Jun;75(3):271-8.

[23] Setup error in radiotherapy: on-line correction using electronic kilovoltage and megavoltage radiographs. Pisani L, Lockman D, Jaffray D, Yan D, Martinez A, Wong J. Int J Radiat Oncol Biol Phys. 2000 Jun 1;47(3):825-39.

[24] T. Thorson, T. Prosser. X-ray volume imaging in image-guided radiotherapy. Med Dosim. 2006 Summer;31(2):126-33.

[25] C. Huntzinger, P. Munro, S. Johnson, M. Miettinen, C. Zankowski, G. Ahlstrom, R. Glettig, R. Filliberti, W. Kaissl, M. Kamber, M. Amstutz, L. Bouchet, D. Klebanov, H. Mostafavi, R. Stark. Dynamic targeting image-guided radiotherapy. Med Dosim. 2006 Summer;31(2):113-25.

[26] Jaffray DA, Siewerdsen JH, Wong JW, Martinez AA. Flat-panel cone-beam computed tomography for image-guided radiation therapy. Int J Radiat Oncol Biol Phys. 2002 Aug 1;53(5):1337-49.

[27] Radiotherapy Equipment - Coordinates, Movements & Scales. IEC 61217. May 1995

[28] B. Hesse. Device for performing and verifying a therapeutic treatment and corresponding program and control method. European Patent WO 03/076016 A1; (2003).

[29] B. Hesse, S. Nill, T. Tücking and U. Oelfke. A novel hardware design for image and dose guided radiotherapy Int. J. Radiat. Oncol. Biol. Phys. 60 (Suppl. 1) 200 (2004).

[30] C. Amies, A. Bani-Hashemi, J. Celi, G. Grousset, F. Ghelmansarai, D. Hristov, D. Lane, M. Mitschke, A. Singh, H. Shukla, J. Stein, M. Wofford. A multi-platform approach to image guided radiation therapy (IGRT). Med Dosim. 2006 Spring;31(1):12-9.

[31] B. Hesse, S. Nill, T. Tücking, U. Oelfke. Ein neues Konzept für die bild- und dosis-geführte Strahlentherapie. In: E-Verhandlungen 2006. Abstracts der Frühjahrstagung in Heidelberg. Heidelberg: Deutsche Physikalische Gesellschaft (DPG) (2006) 11.1.

[32] W. Hamacher. Radiation therapy in cancer treatment.
     `http://optimierung.mathematik.uni-kl.de/research/cancer.html` (2005).

[33] Digital Mevatron Interface Protocol. Rev F. Siemens Medical Solutions. 28 July 2004.

[34] P. Marnier, E. Sheldon. Physics of Nuclei and Particles Vol. I,. Academic Press (1969).

[35] G. Spear. GTN The GLAST Telescope Network.
     `http://gtn.sonoma.edu/public/resources/presentations/gtn_balloons/` (2003).

[36] P. Reiter. Detektoren und Messmethoden. Aufzeichnungen zur Vorlesung WS05/06.
     `http://www.ikp.uni-koeln.de/reiter/vorlesungen.shtml` (2006).

[37] W. Schlegel, J. Bille (eds.). Medizinische Physik (2): Medizinische Strahlenphysik. Springer
     Verlag, Berlin, Heidelberg (2002).

[38] J. Boone, A. Seibert. An accurate method for computer-generating tungsten anode X-ray
     spectra from 30 to 140 kV. Med. Phys. 24(11), 1661-1670 (1997).

[39] J. Boone, T. Fewell, J. Jennings. Molybdenum, rhodium, and tungsten anode spectral models
     using interpolating polynomials with application to mammography. Med. Phys. 24(12), 1863-
     1874, (1997).

[40] J. Boone. Spectral modeling and compilation of quantum fluence in radiography and mam-
     mography. Proceedings of the SPIE 3336, 592-601, (1998).

[41] G. Küster. Monte Carlo Untersuchungen zur Optimierung von Techniken für die konforme
     Strahlentherapie. Dissertation Naturwissenschaftl.-Mathematische Gesamtfakultät, Univer-
     sität Heidelberg, (1999).

[42] L. Feldkamp, L. Davis, J. Kress. Practical cone-beam algorithm. J. Opt. Soc. Am [A] 1:612-9;
     (1984).

[43] A. Seeber. Development and validation of a cone-beam computed tomography reconstruction
     for adaptive therapy of extracranial regions [Diploma thesis]. Universität Karlsruhe (2005).

[44] P. Cho, A. Rudd, R. Johnson. Cone-beam CT from width-truncated projections. Comput.
     Med. Imag. Graph. 20:49-57; (1996).

[45] B. Hesse, S. Nill, T. Tücking, U. Oelfke. Dose Guidance in Radio Therapy by means of Entrance
     Dosimetry. Med Phys., 33(6) 2031 (2006).

[46] B. Hesse, S. Nill, T. Tücking U. Oelfke. 3D in vivo dosimetry by means of entrance dosimetry
     for dose guided radiotherapy. Radiotherapy and Oncology, 81 (Suppl.1) 46 (2006).

[47] B. Hesse, S. Nill, T. Tücking, U. Oelfke. „Entrance Dosimetrie": Eine neue Methode zur
     dosisgeführten Strahlentherapie. In: Medizinische Physik 2006. Hrsg.: L. Bogner, B. Dobler.
     Regensburg: Deutsche Gesellschaft für Medizinische Physik (DGMP) (2006) 276-277.

[48] J. Chang, C. Obcemea, J. Sillanpaa, J. Mechalakos, C. Burman. Use of EPID for leaf po-
     sition accuracy QA of dynamic multi-leaf collimator (DMLC) treatment. Med Phys. 2004
     Jul;31(7):2091-6.

[49] S. Baker, G. Budgell, R. MacKay. Use of an amorphous silicon electronic portal imaging device
     for multileaf collimator quality control and calibration. Phys Med Biol. 2005 Apr 7;50(7):1377-
     92.

[50] Nill S, Unkelbach J, Dietrich L, Oelfke U. Online correction for respiratory motion: evaluation
     of two different imaging geometries. Phys Med Biol. 2005 Sep 7;50(17):4087-96.

[51] D. Grant. Tomosynthesis: a three-dimensional radiographic imaging technique. IEEE Trans Biomed Eng. 1972 Jan;19(1):20-8.

[52] Medical electrical equipment - ALL PARTS IEC 60601. Mar 2006.

[53] Medical electrical equipment - X-ray tube assemblies for medical diagnosis - Characteristics of focal spots IEC 60336. Apr 2005.

[54] S. Mori, M. Endo, K. Nishizawa, M. Ohno, H. Miyazaki, K. Tsujita, Y. Saito. Prototype heel effect compensation filter for cone-beam CT. 2005 Phys. Med. Biol. 50 N359-N370.

[55] J. Siewerdsen, D. Jaffray. Optimization of x-ray imaging geometry (with specific application to flat-panel cone-beam computed tomography). Med Phys. 2000 Aug;27(8):1903-14.

[56] K. Etschberger. Controller Area Network. IXXAT Automation GmbH (2001).

[57] M. Ebert. Non-ideal projection-data in x-ray computed tomography. Dissertation Fakultät für Mathematik und Informatik, Universität Mannheim, (2001).

[58] Y. Cho, D. Moseley, J. Siewerdsen, D. Jaffray. Accurate technique for complete geometric calibration of cone-beam computed tomography systems. Med Phys. 2005 Apr;32(4):968-83.

[59] R. Hinderer, B. Hesse, M. Ebert, S. Nill, U. Oelfke. Correction of non-ideal projection geometries in conebeam computed tomography using a phantom with helically arranged markers. Radiotherapy and Oncology, 73 (Suppl.1) (2004) 228.

[60] H. Barrett, W. Swindell. Radiological imaging. Academic Press, London (1981).

[61] R. Nishikawa. The Fundamentals of MTF, Wiener Spectra, and DQE. http://www.aapm.org/meetings/99AM/pdf/2798-87374.pdf (2001)

[62] E. Samei, M. Flynn, D. Reimann. A method for measuring the presampled MTF of digital radiographic systems using an edge test device. Med Phys. 1998 Jan;25(1):102-13.

[63] H. Busch. Digitale Projektionsradiographie Technische Grundlagen, Abbildungseigenschaften und Anwendungsmöglichkeiten. Der Radiologe. 39:710-724 (1999).

[64] O. Morin, A. Gillis, J. Chen, M. Aubin, M. Bucci, M. Roach, J. Pouliot. Megavoltage conebeam CT: system description and clinical applications. Med Dosim. 2006 Spring;31(1):51-61. Review.

[65] R. Crawford, K. F. King, C. J. Ritchie, and J. D. Godwin. Respiratory compensation in projection imaging using a magnification and displacement model. IEEE Trans. on Med. Imag., 15:327-332, 1996.

[66] L. Dietrich. Berücksichtigung von inter- und intrafraktionellen Organbewegungen in der adaptiven Strahlentherapie. Dissertation Naturwissenschaftl.-Mathematische Gesamtfakultät, Universität Heidelberg, (2005).

[67] L. Dietrich, S. Jetter, T. Tücking, S. Nill, U. Oelfke. Linac-integrated 4D cone beam CT: first experimental results. Phys Med Biol., 51 (2006) 2939-2952.

[68] S. Jetter. Atemgetriggerte Strahlentherapie mit dem Anzai Respiratory Gating System. Diplomarbeit Fakultät für Physik und Astronomie, Universität Heidelberg, (2006).

[69] S. Jetter, L. Dietrich, T. Tücking, S: Nill, B. Hesse, U. Oelfke. Time resolved patient imaging in treatment position. In: E-Verhandlungen 2006. Abstracts der Frühjahrstagung in Heidelberg. Heidelberg: Deutsche Physikalische Gesellschaft (DPG) (2006) 11.4.

[70] L. Dietrich, T. Tücking, S. Nill, U. Oelfke. Compensation for respiratory motion by gated radiotherapy: an experimental study. Phys Med Biol., 50(10) (2005) 2405-2414.

[71] X. Li, C. Stepaniak, E. Gore. Technical and dosimetric aspects of respiratory gating using a pressure-sensor motion monitoring system. Med Phys. 2006 Jan;33(1):145-54.

[72] J. Siewerdsen, D. Moseley, B. Bakhtiar, S. Richard, D. Jaffray. The influence of antiscatter grids on soft-tissue detectability in cone-beam computed tomography with flat-panel detectors. Med Phys. 2004 Dec;31(12):3506-20.

[73] B. Mafopa Njunda B. Verification of the effect of a flat panel detector on the dosimetric properties of a treatment beam. Masterthesis Fakultät für Physik und Astronomie, Universität Heidelberg, (2005).

[74] T. Bortfeld, W. Schlegel, B. Rhein. Decomposition of pencil beam kernels for fast dose calculations in three-dimensional treatment planning. Med. Phys. 20, 311 (1993).

[75] D. Low, W. Harms, S. Mutic, J. Purdy. A technique for the quantitative evaluation of dose distributions. Med Phys. 1998 May;25(5):656-61.

[76] B. Rhein, P. Haring, J. Debus, W. Schlegel. [Dosimetric verification of IMRT treatment plans at the German Cancer Research Center (DKFZ)] Z Med Phys. 2002;12(2):122-32. German.

[77] M. Arnfield, Q. Wu, S. Tong, R. Mohan Dosimetric validation for multileaf collimator-based intensity-modulated radiotherapy: a review. Med Dosim. 2001 Summer;26(2):179-88. Review.

[78] M. Endo, T. Tsunoo, N. Nakamori, K. Yoshida. Effect of scattered radiation on image noise in cone beam CT. Med Phys. 2001 Apr;28(4):469-74.

[79] J. Balter, K. Lam, C. McGinn, T. Lawrence, R. Ten Haken. Improvement of CT-based treatment-planning models of abdominal targets using static exhale imaging, Int. J. Radiat. Oncol. Biol. Phys. 41, 939-943 (1998).

[80] A. Lujan, E. Larsen, J. Balter, R. Ten Haken. A method for incorporating organ motion due to breathing into 3D dose calculations, Med Phys. 26, 715-720 (1999).

[81] C. Thilmann, S. Nill, T. Tücking, B. Hesse, L. Dietrich, B. Rhein, P. Häring, U. Oelfke, J. Debus, P. Huber. Correction of Patient Positioning Errors based on In-Line Cone Beam CTs: Clinical Implementation and First Experiences. International Journal of Radiation Oncology Biology Physics, 63 (Suppl.1) (2005) 550-551.

[82] C. Thilmann, S. Nill, T. Tücking, A. Höss, B. Hesse, L. Dietrich, R. Bendl, B. Rhein, P. Haring, C. Thieke, U. Oelfke, J. Debus, P. Huber. Correction of patient positioning errors based on in-line cone beam CTs: clinical implementation and first experiences. Radiat Oncol. 2006 May 24;1:16.

[83] T. Tücking, S. Nill, U. Oelfke. Evaluation of dose calculation in KV-Cone Beam CT data sets. Medical Physics, 32(6) (2005) 2109.

[84] T. Tücking, S. Nill, U. Oelfke. Dose calculation on linac integrated kv-cone beam CT. Radiotherapy and Oncology, 81 (Suppl.1) (2006) 26.

[85] U. Schneider, E. Pedroni, A. Lomax. The calibration of CT Hounsfield units for radiotherapy treatment planning. Phys Med Biol. 1996 Jan;41(1):111-24.

[86] W. Schneider, T. Bortfeld, W. Schlegel. Correlation between CT numbers and tissue parameters needed for Monte Carlo simulations of clinical dose distributions. Phys Med Biol. 2000 Feb;45(2):459-78.

[87] J. Siewerdsen, D. Jaffray. Cone-beam computed tomography with a flat-panel imager: magnitude and effects of x-ray scatter. Med Phys. 2001 Feb;28(2):220-31.

[88] K. Preiser, T. Bortfeld, K. Hartwig, W. Schlegel, J. Stein. A new program for inverse radiotherapy planning. In: XIIth International Conference on the Use of Computers in Radiation Therapie. D. Leavitt, G. Starkschall (Hrsg.). Medical Physics Publishing 425 (1997).

[89] R. Bendl R, A. Hoess, M. Keller, K. Preiser, J. Pross, W. Schlegel. VIRTUOS - A program for VIRTUal radiOtherapy Simulation and verification. Proceedings of the Eleventh International Conference on the Use of Computers in Radiation Therapy, Manchester 226 (1994).

[90] L. Spies L, P. Evans, M. Partridge, V. Hansen, T. Bortfeld. Direct measurement and analytical modeling of scatter in portal imaging. Medical Physics, 27 (2000) 462-471.

[91] J. Siewerdsen, M. Daly, B. Bakhtiar, D. Moseley, S. Richard, H. Keller, D. Jaffray. A simple, direct method for x-ray scatter estimation and correction in digital radiography and cone-beam CT. Med Phys. 2006 Jan;33(1):187-97.

[92] T. Tücking, L. Dietrich, S. Nill, B. Hesse, C. Thilmann, U. Oelfke. Respiration gated cone beam imaging and fluoroscopy at a linear accelerator. Radiotherapy and Oncology, 76 (Suppl.2) (2005) 127.

[93] S. Nill, S. Jetter, T. Tücking, T. Moser, G. Remmert, J. Biederer, M. Fabel-Schulte, J. Dinkel, U. Oelfke. Comparison of 4D cone beam CT and 4D spiral scan CT using a dedicated chest phantom. Radiotherapy and Oncology, 81 (Suppl.1) (2006) 213.

[94] I. Reitz, B. Hesse, T. Tücking, S. Nill, U. Oelfke. Enhancement of image quality with a fast iterative scatter correction solution for kv CBCT. Radiotherapy and Oncology, 81 (Suppl.1) (2006) 217.

[95] A. Seeber, S. Nill, T. Tücking, U. Oelfke. Linac based kV cone-beam CT for extended field-of-views. In: E-Verhandlungen 2006. Abstracts der Frühjahrstagung in Heidelberg. Heidelberg: Deutsche Physikalische Gesellschaft (DPG) (2006) 11.7.

[96] A. Seeber, S. Nill, T. Tücking, U. Oelfke. Reconstruction of linac based cone-beam CT data for extended field-of-views: analysis quality for a novel imaging setup. In: Biomedizinische Technik, 50 (Suppl.1, Part 1). Hrsg.: U. Boenick u.a. Berlin: Fachverlag Schiele & Schön GmbH, (2005) 619-620.

[97] C. Wu C, R. Jeraj, G. Olivera, T. Mackie. Re-optimization in adaptive radiotherapy. Phys Med Biol. 2002 Sep 7;47(17):3181-95.

[98] M. Birkner, D. Yan, M. Alber, J. Liang, F. Nusslin F. Adapting inverse planning to patient and organ geometrical variation: algorithm and implementation. Med Phys. 2003 Oct;30(10):2822-31.

Zum Schluss möchte ich mich noch bei all denen bedanken, die mich im Laufe meiner Promotion unterstützt haben.

Hierbei ist insbesondere Uwe Oelfke zu nennen, der als AG-Leiter das nötige Vertrauen in mich hatte, mir diese Arbeit zu ermöglichen.

Danke auch an Simeon Nill, der alles kann außer Hochdeutsch und zu jeder Tages- und Nachtzeit bereit war, das Projekt voranzutreiben, sei es durch Softwareentwicklungen, Organisatorisches, Papierkram, oder durch gute Ideen und hilfreiche Unterstüzungen.

Ein besonderer Dank gilt natürlich auch Professor Schlegel, der mit seiner bedachten Art, die Abteilung Medizinische Physik zu leiten, uns allen stets ein angenehmes und freundschafliches Klima vorfinden lässt.

Weiter bedanke ich mich bei Professor Bille, für seine Bereitschaft als Gutachter für diese Arbeit zur Verfügung zu stehen.

Für das Verwandeln des vorliegenden Textes von „Was-ich-für-Englisch-hielt" in Englisch war Joanne zuständig, wofür ich mich hiermit nochmal bei ihr bedanke.

Ein Dank geht auch an die Werkstatt und Gernot Echner und Clemens Lang, die auch kurzfristig immer in der Lage waren, jeden Konstruktionswunsch zu erfüllen und „mechanische Notfälle" zu meistern.

Dass der Spaß nie zu kurz kam, dafür haben jede Menge Kollegen gesorgt, mit denen ich hier tagein, tagaus zu tun hatte. Insbesondere sind das natürlich die N113er: Annette, Thomas und Simeon. Spaß gemacht hats natürlich auch mit allen anderen Kollegen und Exkollegen aus der besten Arbeitsgruppe der Welt.

Bedanken möchte ich mich noch bei allen hier nicht gennanten, die zum Gelingen dieser Arbeit beigetragen haben. Dazu gehören auch viele Siemens Mitarbeiter, die immer wieder in unkomplizierter Weise mit Rat und Tat zur Verfügung standen.

*"Like everyone I have a peripheral role to play in the lives of most people I know, however, and these people are often uninterested in the forthcoming First Division programme. [...] Family and friends know, after long years of wearying experience, that the fixture list always has the last word in any arrangement."*

*Nick Hornby*